May 2017

Late Cretaceous Extensional Collapse of the Southern Cordillera: Evidence from the Bristol and Granite Mountains, SE California

Lee Hess
University of Nevada, Las Vegas, hesslee1@gmail.com

LATE CRETACEOUS EXTENSIONAL COLLAPSE OF THE SOUTHERN CORDILLERA: EVIDENCE FROM THE BRISTOL AND GRANITE MOUNTAINS, SE CALIFORNIA

By

Lee T. Hess

B.S. - Geology
Idaho State University
2011

A thesis submitted in partial fulfillment
of the requirements for the

Master of Science - Geology

Department of Geosciences
College of Sciences
The Graduate College

University of Nevada, Las Vegas
May 2017

UNLV | GRADUATE COLLEGE

Thesis Approval

The Graduate College
The University of Nevada, Las Vegas

May 24, 2017

This thesis prepared by

Lee T. Hess

entitled

Late Cretaceous Extensional Collapse of the Southern Cordillera: Evidence from the Bristol and Granite Mountains, SE California

is approved in partial fulfillment of the requirements for the degree of

Master of Science – Geology
Department of Geosciences

Michael L. Wells, Ph.D.
Examination Committee Chair

Terry Spell, Ph.D.
Examination Committee Member

Wanda Taylor, Ph.D.
Examination Committee Member

Dave Miller, Ph.D.
Examination Committee Member

Dennis Bazylinski, Ph.D.
Graduate College Faculty Representative

Kathryn Hausbeck Korgan, Ph.D.
Graduate College Interim Dean

ABSTRACT

Demonstrating the regional extent of Late Cretaceous extensional collapse of western North America's southern Cordillera is important to understanding the tectonic evolution of the Sevier-Laramide orogens, and the geodynamics of ancient and modern orogens and synconvergent extension. Documenting Late Cretaceous extension in the southern Cordillera requires looking through the extensive overprint by Cenozoic structures. Late Cretaceous extension in the eastern Mojave region has been inferred from geochronology and thermochronology studies, which document Late Cretaceous cooling of Mesozoic granitoid rocks, some of which were emplaced in the middle crust. Cooling histories from these rocks have also been interpreted to be a result of lithospheric refrigeration, as well as erosional exhumation during the Laramide. New data from this study, combined with results from other studies, demonstrate that Late Cretaceous extension and exhumation of mid-crustal rocks was a major event in the southern Cordillera. A newly described (herein) mylonitic shear zone in the Bristol Mountains records a top-to-the-SW, down-dip, non-coaxial sense of shear. Furthermore, microstructural analysis indicates the shear zone recorded deformation temperatures at upper greenschist to lower amphibolite conditions (~350 to ~550 ˚C). Low-temperature overprint suggests progressive denudation of the shear zone into shallow crustal levels. U/Pb geochronology and $^{40}Ar/^{39}Ar$ thermochronology demonstrate that Cretaceous plutons were emplaced at ~75 Ma and cooled below K-feldspar MDD small domain closure temperatures by ~65 Ma. MDD modeling of K-feldspar from plutonic rocks show that following ductile shearing and rapid cooling, rocks continued to cool at rates of ~22 ˚C/m.y (footwall) and ~16 ˚C/m.y. (shear zone) Mylonitic deformation in the Bristol Mountains is bracketed from ~75 Ma to 65 Ma. Kinematic indicators from the Granite Mountains shear zones show a top-to-the-NW, down-dip, non-coaxial sense of shear. Distinct banding of dynamically recrystallized quartz and feldspar suggests the shear zone recorded deformation temperatures in the lower amphibolite facies (~400 to ~600˚C). Furthermore, U/Pb geochronology and $^{40}Ar/^{39}Ar$ thermochronology indicate that Cretaceous plutons were emplaced from ~80 Ma to ~75 Ma and were rapidly cooled through K-feldspar MDD closure temperatures by ~66 Ma. MDD modeling of K-feldpsar, within the footwall, suggest that Cretaceous plutons cooled at rates ranging from ~16 to 67 ˚C/m.y. Mylonitic deformation in the Granite Mountains is bracketed from ~80 Ma to 66 Ma. Data from the Bristol and Granite mountains indicate ductile shear zones unequivocally document extensional collapse of the Sevier retroarc in the Late Cretaceous. We advocate the removal of the North American lithospheric mantle as the root cause for synconvergent extension in the southern Cordillera as it best fits the geologic constraints. The process of delamination is considered the most viable mechanism for removal of the mantle lithosphere, leading to crustal anatexis, peraluminuous magmatism, and extensional collapse of the southern Cordillera, which was synchronous with continued contraction in the Sevier fold-thrust belt as well as the newly developed Laramide deformational belts.

ACKNOWLEDGMENTS

Most of all I would like to thank Dr. Michael L. Wells for setting me up with this amazing project. His resources have made everything here possible and his patience for my many myopic questions and the sharing of his vast knowledge is hugely appreciated. Dr. Wells has taught me more about western North America Cordilleran geology than I ever thought possible. His enthusiasm and excitement in the field has shaped me as the field geologist I am today. Also, I owe a huge thanks to David M. Miller for taking time out of his busy schedule and serving on my committee. His valuable insight on geology of the southern Cordillera has strengthened this research project substantially. That said, all my committee members deserve a huge amount of gratitude for their patience and attention to detail through the editing process.

Kathy Zanetti at the NIGL has helped me hugely in so many ways, without her and Dr. Terry Spell this project would not have been possible. Also, Dr. Minghua Ren at the EMIL deserves a gigantic thank you for helping me set-up and run the CL detector on the SEM, so we could obtain publication-quality zircon images. I am also very grateful to Dr. Martin Wong from Colgate University for helping figure out Multiple Domain Diffusion modeling, and showing me Arvert, a Mac friendly modeling software. The lab technicians at the Arizona LaserChron lab at the University of Arizona deserve acknowledgment for putting up with my many unintelligent questions and late night foul-ups on the LA-ICP-MS.

Several field assistants I have employed over my project merit a huge thank you; Chris Wing, Dr. Arya Udry, Chad Crotty, and Will Joseph you were great to have in the field, and were great sports on the heinous hikes we endured. Dr. Arya Udry – you deserve the biggest thank you of all! Lastly, I must give recognition to Red Rock Canyon and all the classic rocks climbs therein. This place and all its greatness has let me grow as a person more than I would have ever imagined, and has given me much mental support over the years of living in Las Vegas.

TABLE OF CONTENTS

LIST OF FIGURES

1. INTRODUCTION

Late Cretaceous orogenic collapse and exhumation of mid-to-lower crustal rocks have been recognized along the retroarc of the Sevier orogenic belt, but its geographic distribution and causes are still poorly understood due to overprinting by mid-Cenozoic structures, alternative mechanisms proposed to explain Late Cretaceous cooling ages, and a variety of potential geodynamic drivers (Carl et al., 1991; Dumitru et al., 1991; Hodges and Walker, 1992; George and Dokka, 1994; Applegate and Hodges, 1995; Saleeby, 2003; Wells et al., 2005; Wells and Hoisch, 2008; Wells et al., 2012) (Figure 1). Understanding the cause, extent, and timing of synorogenic extension, exhumation, and cooling of mid-crustal rocks in the southern Cordillera is the focus of this study. Several mechanisms have been invoked to explain Late Cretaceous cooling ages across the eastern (Foster et al., 1992; Wells and Hoisch, 2008), western Mojave Desert (Miller and Morton, 1980; Jacobson, 1990) and adjacent arc (George and Dokka, 1994; Grove et al., 2003a; Saleeby et al., 2007). These include: erosional exhumation (George and Dokka, 1994; Grove et al., 2003a), refrigeration of the North American lithosphere (Dumitru et al., 1991), and gravity-driven extensional collapse (Hodges and Walker, 1992; Saleeby, 2003; Wells et al., 2005; Wells and Hoisch, 2008). Rapid cooling of mid-crustal peraluminous granitoid rocks has been documented across the eastern Mojave region, from the Old Woman Mountains in the south to the New York Mountains to the north, and is interpreted as being a result of extensional exhumation (Foster et al., 1989; Foster et al., 1992; McCaffrey et al., 1999; Beyene, 2000; Kula, 2002; Wells et al., 2002; Wells et al., 2005), although structures of Late Cretaceous age are cryptic. Additionally, George and Dokka (1994) and Grove and others (2003a) document rapid cooling of the southern magmatic arc region in the Peninsular Ranges, which they attribute to uplift during Laramide tectonics and subsequent erosional exhumation. Saleeby (2003) has proposed that cooling and upper-plate extension in the southern Sierra Nevada batholith and adjacent western Mojave region resulted from underthrusting of schists due to Laramide flat-slab subduction and slab segmentation. Furthermore, Dumitru et al. (1991) suggested there is no need for extension or exhumation to explain the cooling ages in the southern Cordillera, and concluded that lithospheric refrigeration of the North American plate is a plausible explanation for the observed cooling ages. Lithospheric refrigeration is interpreted to be a result of replacing hot asthenosphere beneath the North American plate with a cold oceanic plate. Detailed studies linking footwall thermochronology to geologic structures are needed to further resolve the extent and driving mechanisms for Late Cretaceous synconvergent extension.

The cause and extent of synconvergent extension in the Late Cretaceous, which led to the initial piecemeal collapse of the Sevier retroarc, is debated among researchers. Extension in the Late Cretaceous was synchronous with active shortening along the Sevier fold-thrust belt (SFTB) of Utah, Idaho, and Wyoming, as well as the nascent Laramide province. The southern SFTB was effectively inactive by ~90 Ma, and is broadly coincident with the cessation of arc magmatism (DeCelles et al., 2009, DeCelles and Graham, 2015). Although it is recognized that synconvergent extension is partly caused by lateral gradients in gravitational buoyancy forces stored within the lithosphere, resulting from horizontal gradients in crustal thickness, density and topography (e.g., Jones et al., 1998; Sonder and Jones, 1999), the mechanisms giving rise to an increase in gravitational potential energy and the role of rheological weakening are debated. Increases in buoyancy forces can be driven by several mechanisms, e.g., crustal thickening and uplift during orogenesis including underplating in the interior of orogenic wedges (Platt, 1986; Molnar and Chen, 1988), delamination of a dense lithospheric root from the overriding plate causing isostatic rebound (Houseman et al., 1981; England and Houseman, 1989) or similarly, subduction erosion of dense lithosphere during low-angle subduction (Saleeby, 2003; Liu et al., 2010). Although gravitational forces are important as driving forces for extension, the mechanisms that produce environments where gravitational forces exceed horizontal compressional forces and crustal strength are not fully understood.

The Granite and Bristol mountains are plutonic complexes comprised of mid-crustal Jurassic and Cretaceous granitoid rocks, located near the southern end of the Sevier orogenic belt in southeast California (Figures 1 & 2). The Granite and Bristol mountains lie within the Mojave Block and Laramide deformational corridor in southern California, an area greatly affected by subduction erosion, schist underplating, Cenozoic extension, and dextral shearing associated with the Eastern California shear zone. Previous geobarometry and thermochronology studies in the Granite Mountains indicate mid-crustal (4.5 kbar) crystallization of Late Cretaceous granites followed by rapid cooling to temperatures below ~150 ˚C during the Late Cretaceous which was attributed to extensional exhumation (Kula, 2002). However, extensional structures responsible for the Late Cretaceous exhumation were not previously identified (Kula, 2002). The only documented structure responsible for exhumation is the Neogene Bull Canyon Fault (BCF), which wraps around the northwestern margin of the range and dips ~40˚ to the NW with brittle striae trending to the NW (Howard et al., 1987, this study). The age of the BCF is poorly constrained by geological relationships, with the fault apparently cutting Quaternary-Tertiary gravels and Tertiary mega breccia in the hanging wall (Howard et al., 1987; Miller et al., 1992). The BCF is demarked by well-developed cataclastic to ultracataclastic rocks and associated highly fractured and cleaved Jurassic diorite and granite (Howard et al., 1987).

This research will present new geologic mapping, structural orientation data, microstructural analysis, geochronology, and thermochronology from the Bristol and Granite mountains of the

Mojave Desert in southeast California. These data show that the rapid cooling of mid- crustal plutons in the Bristol and Granite mountains was a result of unroofing by extensional shearing in mylonitic rocks and record a Late Cretaceous unroofing event responsible for partial exhumation of plutonic rocks. Furthermore, results from the Bristol Mountains constrain the geometry, kinematics, and age of a previously undocumented shear zone. Mapping of the BCF in the Granite Mountains shows that Cenozoic detachment faulting reactivated a Late Cretaceous extensional shear zone, and excised, overprinted, and/or displaced most evidence for Late Cretaceous extension. The discontinuous mylonitic belt in the footwall of the BCF is interpreted to be the base of the structure(s) responsible for Late Cretaceous cooling and unroofing in the Granite Mountains, first recognized by Kula (2002). Data from the Bristol and Granite mountains are consistent with other Late Cretaceous cooling signatures in the Mojave Desert, as well as the Great Basin. Therefore, these observations are most consistent with a single orogen-wide mechanism that explains Late Cretaceous rapid cooling and exhumation. Although erosional exhumation and lithospheric refrigeration may be locally important, following Wells and Hoisch (2008), we hypothesis that the cause of extension along the axis of the earlier contractionally thickened lithosphere is widespread delamination of a dense lithospheric root from the North American plate at ~75 Ma, which subsequently caused isostatic uplift of the orogen and gravity-driven collapse. Demonstrating extensional structures of Late Cretaceous age is fundamental to understanding the geodynamics of synconvergent extension and, furthermore, the incipient collapse of the North American Cordillera.

2. GEOLOGIC BACKGROUND

2.1 Sevier-Laramide Orogenies

The Sevier Orogeny initiated in the Late Jurassic, following a reorganization at the plate margin and inception of subduction of the Farallon plate eastward beneath the North American plate (Burchfiel et al., 1992; DeCelles, 2004; Yonkee and Weil, 2015). By the earliest Cretaceous, a mature fold and thrust belt had developed across the Cordilleran retroarc of the western United

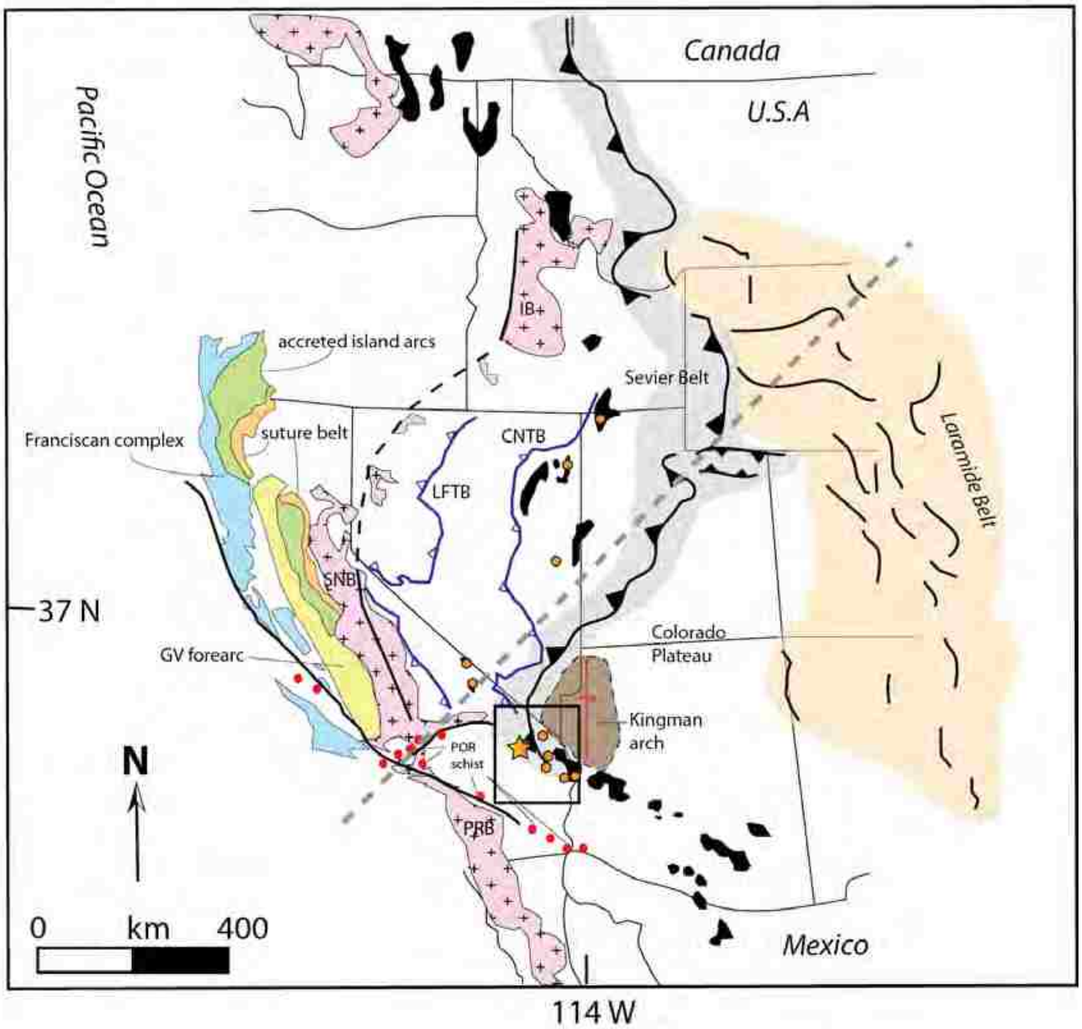

[redacted]

States and Canada (Figure 1) (Burchfiel et al., 1992; DeCelles, 2004; Yonkee and Weil, 2015). Continued contraction and thickening of continental crust eventually led to an unstable orogen and by the Late Cretaceous, incipient extensional collapse was taking place, resulting in the rapid exhumation of mid-crustal rocks in the Sevier retroarc (Hodges and Walker, 1992; Miller et al., 1995; Wells et al., 2005; Wells and Hoisch, 2008; Wells et al., 2012). It is hypothesized that collapse of the Sevier orogen is partially due to the development of a dense root beneath the North American continent, which delaminated from the lithospheric mantle causing an isostatic response and uplift of a high orogenic plateau (Coney and Harms, 1984; DeCelles, 2004; Wells et al., 2005; Wells and Hoisch, 2008; Druschke et al., 2011; Ernst, 2010; Snell et al., 2013). The high plateau became gravitationally unstable, leading to internal extensional deformation (Jones et al., 1998; Sonders and Jones, 1999; Wells and Hoisch, 2008; DeCelles et al., 2009; Wells et al., 2012). The Sevier fold-thrust belt and associated Mesozoic intrusive rocks intersect within the Mojave Desert, where the Proterozoic-Paleozoic passive margin sedimentary wedge was crosscut by the Mesozoic magmatic arc.

At approximately 80 Ma, the Farallon plate began to change geometry to flat-slab subduction, marking the transition to the Laramide orogeny, which is characterized by thick-skinned deformation. An increase in convergence rate and subduction of a more buoyant oceanic plateau – a counterpart or conjugate to the Hess-Shatsky rise (Livaccari et al., 1981; Henderson et al., 1984; Barth and Scheiderman; 1996; Saleeby, 2003; Liu et al., 2008; Liu et al., 2010) – led to a shallowing in the subduction angle of the Farallon plate. Laramide deformation is demarked by basement cored uplifted arches which are separated by broad basins (Yonkee and Weil, 2015), which extends from southern Montana to northern Arizona and New Mexico, defining a deformational belt much further inland than the SFTB. The change to Laramide style deformation effectively shut-off asthenospheric flow beneath the western margin of the North American plate, leading to a cessation in arc magmatism in the Sierra Nevada and Mojave region (Saleeby, 2003). Laramide tectonics in the Mojave region also led to underthrusting of schists with Franciscan affinities, westward impingement of the arc by top-W thrusting and large scale detachment faulting, which produced a highly oblique tilted crustal section with ~9 kbar rocks exhumed in the southernmost Sierra Batholith (Saleeby, 2003). Cooling ages of underplated schists vary from older (~88 Ma) in the west to younger (~67 Ma) in the east (Saleeby et al., 2007). Additionally, detrital zircon ages of the Franciscan-type sediments follow a similar spatial pattern (Jacobson and Dawson, 1995; Jacobson et al., 1996; Grove et al., 2003; Jacobson et al., 2011). Detrital as well as cooling ages farther east, specifically in western Arizona, are much younger (~60 Ma) than ages observed in plutonic rocks across eastern Mojave Desert (Jacobson et al., 1988; Jacobson, 1990; Jacobson and Dawson, 1995; Jacobson et al., 1996; Grove et al., 2003; Jacobson et al., 2011). This observation further contradicts the idea of a refrigeration effect being responsible for cooling of crustal rocks across the Mojave Desert - schists were underplated after the cooling event recorded in the Mojave, which requires cooling caused by extensional and erosional exhumation. Basal traction and end-loading of the North American plate propagated deformation inboard from the plate margin for ~1,500 km, disrupting the Sevier foreland (Saleeby, 2003; Yonkee and Weil, 2015) (Figure 1). Furthermore, as the more buoyant subducted large igneous province (LIP) propagated eastward, dynamic topographic responses are predicted from geodynamic modeling to have occurred at both the leading and trailing end of the LIP, causing initial subsidence followed by uplift (Liu et al., 2010). The Kingman arch of southern Nevada and northwestern Arizona is an uplift of Laramide age (Beard and Faulds, 2010) that led to a highland in the southern Cordillera, east of the Sevier FTB (Figure 1). Paleozoic and Mesozoic rocks were subsequently eroded and deposited along the

Colorado Plateau in Late Cretaceous-Eocene time, with remnant deposits represented in the "rim gravels" (e.g., Young and Hartman, 2014). The signature unconformity throughout the Kingman arch is Proterozoic basement rocks overlain by Miocene sedimentary and volcanic rocks (Faulds et al., 2001). Beard and Faulds (2010) postulate that uplift of the Kingman arch postdates intrusion of 70 Ma peraluminous granites in the region. Evidence of the high Kingman arch in the Late Cretaceous – early Palaeocene and subsequent stripping suggests erosion of the southern Cordillera was likely a significant contributor to exhumation post-70 Ma.

2.2 Basin and Range Extension

The Laramide orogeny persisted until ~50 Ma when post-orogenic collapse of structural highlands and areas of gravitationally instability initiated. Eocene post-orogenic collapse of the North American Cordillera is partly due to the Farallon plate "peeling away" from the North American plate, allowing compressional forces to relax and gravitational potential energy stored in the crustal welt to drive extension (Humphreys, 1995; Sonder and Jones, 1999). The Cordilleran contractional belt began orogenic collapse immediately following Laramide deformation, with a time-gap of ~ 1-5 m.y., and is partly coeval with the development of the Cordilleran metamorphic core complexes (Coney and Harms, 1984; Constensius, 1992). Removal of the Farallon plate, whether by slab rollback or density-driven foundering, eventually led to the development of the Basin and Range province, and allowed for renewed asthenospheric flow beneath the hydrated North American plate. Renewed asthenosphere flow led to thermal weakening of the North American lithosphere and widespread bimodal volcanism to disperse across western North America (Constensius, 1992; Humphreys, 1995; Dickinson, 2002; Copeland et al., 2017). Volcanism and extension swept from the north and south, respectively, and converged in the central Basin and Range in southern Nevada by ~15 Ma.

The Basin and Range is a physiographic province which is spatially and temporally divided into three subprovinces, based on differences in extensional histories and structural styles (Wernicke, 1990). The subprovines correlate with differences in evolving plate dynamics (Sonder and Jones, 1999). Extension in the northern Basin and Range (NBR) initiated at ~48 Ma in Idaho and Wyoming and subsequently stepped southwestward. The NBR is characterized by high elevation, high heat flow, and extensively thinned crust (Sonder and Jones, 1999). Magmatism and extension in the NBR is postulated to be related to buckling and roll-back of the Farallon plate and tracks the position of the foundering slab beneath North America (Humphreys, 1995). In contrast, within the southern Basin and Range (SBR), extension and magmatism initiated at ~28 Ma. SBR is the least active subprovince in the Basin and Range physiographic province with the lowest surface elevations and heat flow (Sonder and Jones, 1999). Extension in the SBR swept from the ESE to the WNW, temporally. Deformation and magmatism is associated with an evolving plate margin at ~28 Ma. The interaction of the mid-oceanic spreading ridge between the Pacific and Farallon plates with the North American plate margin created the Mendocino and Rivera triple junctions. Subduction of the Farallon side of the mid-oceanic ridge led to a slab window beneath the North American plate and the newly formed triple junctions migrated northward and southward, allowing compression to relax and widespread extension to occur in the SBR until ~16 Ma (Dickson and Snyder, 1979; Sonder and Jones, 1999). Extension began to slow in the SBR as the Mendocino triple junction migrated northward. Extension and magmatism initiated in the central Basin and Range (CBR) at ~16 Ma and swept from east to west, temporally. The CBR has the highest local relief, high local heat flow and marks a transition between the NBR and SBR. Furthermore, the CBR marks the area of greatest extension in the Basin and Range and is extending the area between the rigid Sierra Nevada and Colorado Plateau blocks (Sonder and Jones, 1999). The Mojave block, Bristol and Granite mountains are greatly affected by CBR deformation. The Bull Canyon detachment fault of the Granite Mountains is a low-angle normal fault associated with CBR extension.

2.3 Eastern California Shear Zone

The Eastern California shear zone (ECSZ) is a deformational belt chiefly comprising NW striking right-lateral strike-slip faults that propagate North America-Pacific transform motion across the Mojave block to the southern Walker Lane belt (WLB) in the western Great Basin (Dokka and Travis, 1990; Faulds and Henry, 2008; Miller, 2017). At ~30 Ma, deformation at the plate margin evolved from an Andean-type subduction margin to a transform dominated margin, due to the interaction of the Pacific - Farallon ridge with the North American plate margin and the northward and southward migration of the Mendocino and Rivera triple junctions, respectively (Atwater, 1970; Atwater and Stock, 1998). As the Mendocino triple junction migrated northward, some of the strain was partitioned to the east side of the Sierra Nevada block, transecting the Mojave Desert to join the San Andreas fault system to the south and forming the incipient ECSZ and WLB (Faulds and Henry, 2008). The ECSZ is kinematically linked with the San Andreas fault system and is defined by a ~150 km wide belt south of the Garlock Fault (Figure 1). The ECSZ is responsible for ~65 km of right lateral displacement from the Miocene to Quaternary (Faulds and Henry, 2008). To the north, the WLB is accommodating dextral motion of the rigid magmatic arc (Sierra Nevada microplate) with respect to the Basin and Range Province. Deformation of the WLB terminates coincidently in the southern Cascade region near the Mendocino triple junction, suggesting a causative link with the San Andreas system and plate boundary motion (Faulds et al., 2005). Geodetic data suggest these deformational belts are presently accommodating ~20% of right-lateral motion between the North American and Pacific plates (Hammond and Thatcher, 2007).

The ECSZ greatly disrupts the Mojave Desert with significant right-lateral motion (Miller, 2017). The Bristol-Granite Mountain Fault Zone (BGMFZ) is thought to be the northeastern-most segment of the ECSZ, and structurally dissects the Bristol and Granite mountains. Lease et al. (2009) indicate a minimum dextral offset of ~19 km, post-18 Ma, along the BGMFZ by using paleovalley reconstructions and age constraints from the Peach Springs Tuff. Furthermore, Dokka and Travis (1990a) proposed a 21.5 km offset across the BGMFZ based on strain compatibility kinematic models. Miller (1993) and Howard and Miller (1992) proposed a 0-10 km offset based on offset of east-trending rhyolite flows. New constraints from gravity and aeromagnetic data suggest the BGMFZ and Soda-Avawatz fault, a northern strand of the BGMFZ, accommodate 9-15 km of right-lateral offset post-18 Ma (Langenheim and Miller, 2017). Reconstruction of this fault is crucial to understanding the geologic evolution of the Bristol and Granite mountains.

2.4 Eastern Mojave Desert

The Eastern Mojave Desert is a region with numerous Mesozoic contractional structures, Mesozoic and Cenozoic extensional features, and extensive Mesozoic magmatic arc rocks and Cenozoic bimodal volcanic rocks (Burchfiel and Davis, 1981; Foster et al., 1990; Glazner et al., 1994). The Mojave region sits at the crossroads of the SFTB and the Mesozoic magmatic arc. Many of the Late Cretaceous plutons within the eastern Mojave display textures and cooling signatures consistent with syn-extensional emplacement and subsequent exhumation. Furthermore, many ductile extensional shear zones within this region record the partial denudation and unroofing of mid-crustal rocks to shallow crustal levels during the Late Cretaceous. The timing and kinematics of Late Cretaceous extension in the Mojave are consistent with data and observations from the Bristol and Granite mountains.

2.4.1 Granite and Bristol Mountains

The Granite Mountains are a domal plutonic complex compromised mostly of mid-crustal Jurassic and Cretaceous igneous rocks with small roof pendants present at higher elevations (Figure 2b) (Howard et al., 1987). Roof pendant rocks are marbles and calcsilicate rocks with small zones of skarn alteration, possibly correlating to the Monte Cristo Formation (Mississippian) and the Bird Spring Formation (Pennsylvanian to Permian) in the nearby Providence Mountains (Howard et al., 1987). The Mesozoic plutonic rocks range in composition from diorite to granodiorite and porphyritic monzogranite (Howard et al., 1987; Young et al., 1991). Kula (2002) used Al-in-hornblende geobarometry on Late Cretaceous plutonic rocks in the Granite Mountains to show 4-4.5 kbar emplacement pressures corresponding to mid-crustal depths. The presence of Paleozoic roof pendants within mid-crustal plutons, adjacent to an unmetamorphosed upper crustal Paleozoic section in the Providence Mountains, suggests pre-intrusive structural burial of the Granite Mountain strata. Kula (2002), using $^{40}Ar/^{39}Ar$ hornblende and K-feldspar thermochronology, also documented a geologically rapid cooling event in the Late Cretaceous, which was attributed to extensional exhumation, though structures responsible for exhumation were not recognized. The Bull Canyon Fault (BCF), the only exhumational structure previously recognized in the Granite Mountains, is exposed along the northern and northwestern base of the Granite Mountains (Figure 2b). The BCF is a Neogene (?) normal fault, dipping away from the range at ~40˚NW, demarked by zones of intense brecciation, highly fractured diorite and leucogranite, and well developed orange to red cataclastic and ultracataclastic fault rocks. Rocks in the immediate footwall of the BCF are highly chloritized Jurassic plutonic rocks, Geologic mapping of the Bristol Mountains, to the NW, indicates plutonic lithologies are similar to those in the Granite Mountains, ranging in composition from diorite to granodiorite and granite. A large mylonitic shear zone is present along the west and southwest portions of the mountain range. U/Pb dating of zircon (this study) indicates Cretaceous and Jurassic plutons were emplaced synchronously with plutons in the Granite

Mountains. $^{40}Ar/^{39}Ar$ thermochronology on mica and K-feldspar (this study) in the Bristol Mountains demonstrates Late-Cretaceous plutons underwent a rapid cooling event, coeval with cooling in the Granite Mountains.

The BGMFZ, a dextral strike-slip fault that strikes NW and dips ~70-80˚ NE, separates the Bristol Mountains to the west and the Granite Mountains to the east (Figure 2b) (Howard et al., 1987). The BGMFZ plays an important role in displacing the Granite Mountains from the Bristol Mountains, though the significance is poorly understood. It is considered herein that the paleovalley reconstruction estimate of Lease et al. (2009) is unreliable. New data from geophysical data indicate a 9-15 km offset (Langenheim and Miller, 2017). The magnitude of offset across the BGMFZ is important in reconstructing where the Bristol Mountains lay relative to the Granite Mountains; we adopt the conservative 9-15 estimate of Langenheim and Miller (2017).

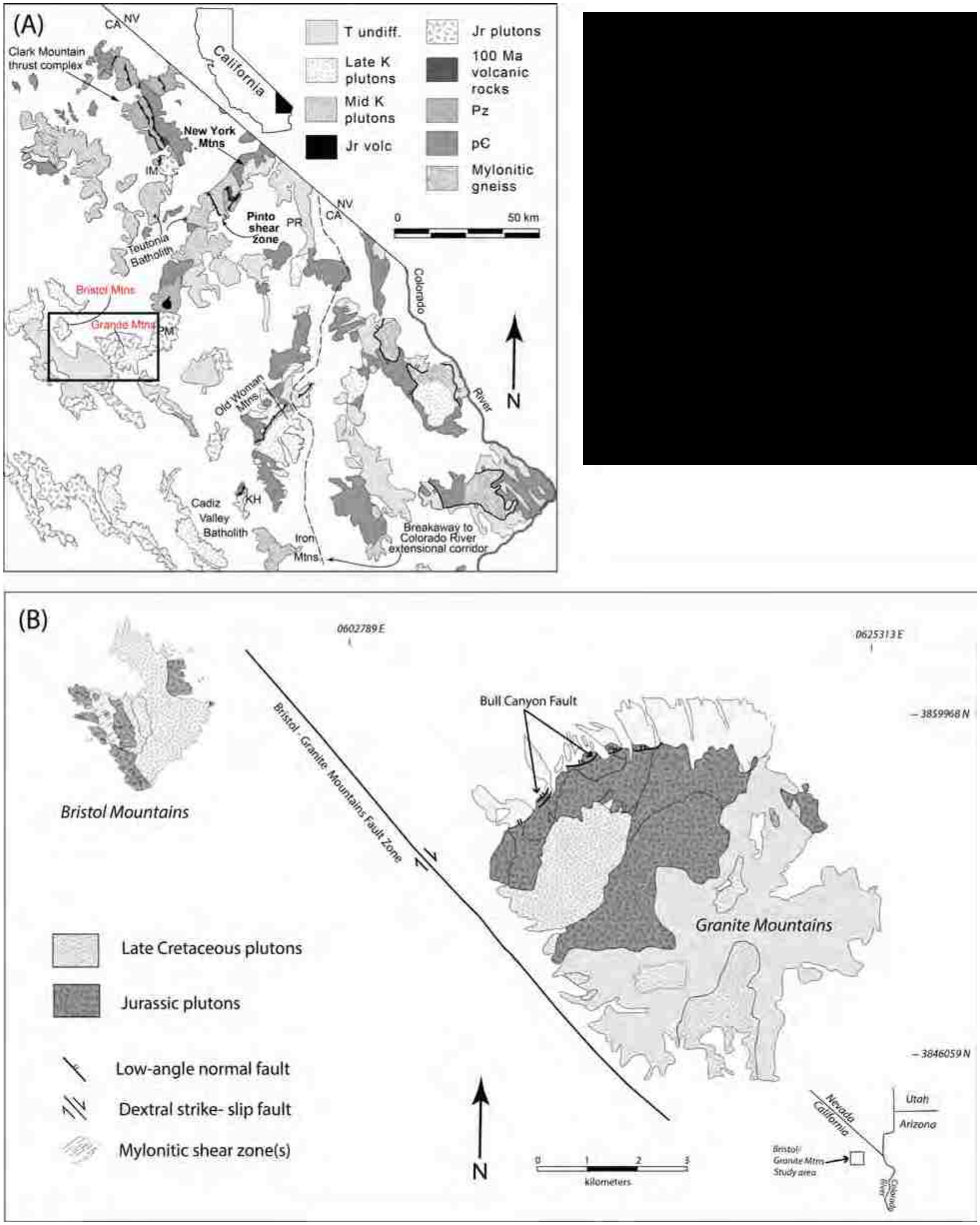
(A)
CA
NV
California
Clark Mountain thrust complex
New York Mtns
IM
Pinto shear zone
PR
Teutonia Batholith
Bristol Mtns
Granite Mtns
PM
Colorado
River
Old Woman Mtns
Cadiz Valley Batholith
KH
Iron Mtns
Breakaway to Colorado River extensional corridor
T undiff.
Late K plutons
Mid K plutons
Jr volc
Jr plutons
100 Ma volcanic rocks
Pz
pC
Mylonitic gneiss
0
50 km
N
(B)
0602789 E
0625313 E
3859968 N
3846059 N
Bristol Mountains
Bristol - Granite Mountains Fault Zone
Bull Canyon Fault
Granite Mountains
Late Cretaceous plutons
Jurassic plutons
Low-angle normal fault
Dextral strike- slip fault
Mylonitic shear zone(s)
N
kilometers
Nevada
California
Utah
Arizona
Bristol/ Granite Mtns Study area
Colorado River

3. METHODS

This study addresses the fundamental hypothesis that the ductile mylonitic shear fabrics present in the Granite and Bristol mountains record Late Cretaceous extensional deformation, which resulted from widespread collapse of the Sevier retroarc. Furthermore, it is hypothesized that the BCF was reactivated in the Cenozoic and obscured the Late Cretaceous extensional shear zone. To test these hypotheses, the following research questions were addressed: (1) What are the emplacement ages and thermal histories for the Cretaceous and Jurassic plutons spanning the footwall of the shear zones present in the Granite Mountains and Bristol Mountains? (2) What are kinematics for the mylonitic rocks, and are they similar? (3) What is the age of mylonitic shearing as constrained by deformation temperatures and thermal histories of footwall rocks? (4) What is the relationship between the BCF and the mylonitic fabrics in the immediate footwall?

3.1 Sampling Approach

To address the emplacement and thermal histories of the Cretaceous and Jurassic plutons, one sampling transect was performed across each mountain range. For the Granite Mountains, we build off the study of Kula (2002), who presented U/Pb zircon, $^{40}Ar/^{39}Ar$ hornblende and K- feldspar, and Al-in-hornblende barometric data along a NE-SW transect. The transect for the current study trends SE-NW, parallel to the transport direction of the mylonitic shear zone and BCF, and utilizes the central sample from the transect of Kula (2002). This study added two additional sampling locations (GM6 and GM7), for which we analyzed zircon for U/Pb crystallization ages, as well as hornblende (one sample), biotite, and K-feldspar for $^{40}Ar/^{39}Ar$ thermochronology. Furthermore, we determined improved U/Pb zircon ages for Cretaceous plutons sampled by Kula (2002), utilizing advances in U/Pb LA-ICP-MS analysis, to refine emplacement and crystallization ages used to construct T-t profiles. Moreover, two additional samples, a diorite (GM5) and leucogranite pluton (GM138) (Figure 3), were collected for U/Pb zircon ages to address the timing of emplacement for Jurassic plutons. The new data, along with those presented in Kula (2002), provide substantial constraints on the overall emplacement and thermal histories across the footwall of the mylonitic shear zone and BCF of the Granite Mountains. In the Bristol Mountains, three samples (BM16, BM17, BM18/13) were collected along a SW-NE transect, spanning the footwall and shear zone parallel to transport direction. On this transect, one sample was analyzed for a zircon U/Pb age, and four micas and two K-feldspars were analyzed for $^{40}Ar/^{39}Ar$ thermochronology. Additionally, two samples, not on the transect, were sampled from a Cretaceous (BM9) and Jurassic pluton (BM4) for zircon U/Pb ages, as well as a mica cooling age from the Cretaceous pluton to obtain preliminary data from the range (Figure 7). To constrain deformation temperatures and kinematics of ductilely deformed mylonitic rocks, multiple oriented samples were collected from the shear zone(s). Samples were collected along strike, spanning the length of the exposed shear zone(s).

3.2 Analytical Techniques

3.2.1 Mineral Separation and Characterization

Mineral separates were prepared at UNLV's rock preparation and mineral separation labs. Rocks samples collected from the field were crushed using a Badger crusher to reduce rocks to chip sized fragments. Chips were then pulverized using a disk mill. Pulverized material was seived to segregate mineral fraction sizes. A sieve stack of varying nominal sieve size opening, ranging from 354 microns to 44 microns, was used. Minerals were chosen from different size fractions based on degree of complete disaggregation (e.g. monomineralic grains) and mineral freshness.

For zircon separation, approximately 2.5 kg of sample from the 44-354-micron size fraction were washed on a wifley table to separate minerals by density. Minerals in the last (heavies) cup were then dried and a hand magnet was used to remove magnetite and any metal shavings from the crushing process. Methylene iodide - a heavy liquid with specific gravity (S.G.) of 3.32 – was used to sink zircons and float minerals with S.G. less than 3.32. After heavy liquids separation and washing, the sample was further separated using a Frantz isodynamic magnetic separator. Samples are run through the Frantz at varying amperages and varying tilts of the sample tray to completely remove all magnetic materials from the non-magnetic zircons. Final sample purification (>99%) is done under a binocular microscope by hand picking non-zircons out of the sample with tweezers and small needles. Approximately 100 grains were selected for analysis for each sample.

To separate hornblende, a sieved size fraction ranging from 177 to 250 microns was extracted from the pulverized material. Sample was then magnetically separated using hand magnetics and Frantz magnetic separator to remove most magnetic material and reduce sample size. Following this step, a heavy liquids separation step was used; methylene iodide (S.G. 3.32) was diluted to an S.G. of 3.1 to sink hornblende and float other minerals with S.G. values less than 3.1 (e.g. quartz, feldspar, and mica). Additional Frantz magnetic separation was used to further purify hornblende. Final purification was done using a binocular microscope to produce 150-300 mg of mineral separate.

To separate biotite and muscovite, sample size fractions ranging from 177 to 250 microns were used. A simple "paper shake" technique was used to separate mica. A small amount of sample was placed on a sheet of white computer paper; the sample was then agitated back and forth until quartz and feldspar rolled off the paper leaving behind mica. Mica commonly forms sheets with high surface area and surface tension allowing for the mineral to stick to the paper while other grains roll off. Following the paper shake technique, a Frantz magnetic separation step was used to remove any mica from feldspar and quartz that made it through the paper shake. Final sample was purified by hand picking out grains with impurities or inclusions to produce approximately 150-200 mg of mineral concentrate.

Potassium feldspar (K-feldspar) was separated from size fraction ranging from 177 to 250 microns. An initial Frantz magnetic separation step was used to reduce sample size and remove magnetics. Bromoform – a heavy liquid with a specific gravity of 2.85 – was used to separate K-feldspar. K-feldspar has a specific gravity of 2.5-2.6. Bromoform was diluted with acetone to an S.G. of ~2.61, to sink quartz and suspend plagioclase while leaving K-feldspar floating in the heavy liquid column. K-feldspar was run through the Frantz magnetic separator at high amperages (~ 2.2-2.5 A) to remove grains with magnetic inclusions. Final separation was done using a binocular microscope and tweezers. Only K-feldspar grains that appeared glassy (not milky) were hand-picked for final analysis. Approximately 150-300 mg was collected for final analysis.

3.2.2 U/Pb Zircon Geochronology

The U/Pb system is a robust dating system, which utilizes the decay of U-Th to Pb to isotopically date zircons. U and Th decay to stable Pb isotopes at a specific half-life which is used to determine ages. These are: ^{238}U to ^{206}Pb with a half-life of 4.468 Ga, ^{235}U to ^{207}Pb with a half-life of 704 Ma, and ^{232}Th to ^{208}Pb with a half-life of 14.01 Ga. Primarily three isotopic ratios are measured to determine ages: $^{238}U/^{206}Pb$, $^{235}U/^{207}Pb$, and $^{207}Pb/^{206}Pb$. When $^{238}U/^{206}Pb$ and $^{235}U/^{207}Pb$ yield the same age, the sample is concordant, thus it preserved a closed system and is ideal for determining the age of a zircon crystal. When $^{238}U/^{206}Pb$ and $^{235}U/^{207}Pb$ ages are varying, the sample is discordant and either has been subjected to an open system resulting in Pb loss or contains a component of older, inherited, material; these analyses are rejected from the final age calculation. Typically, with igneous zircons, rims of crystals are analyzed to determine the crystallization age whereas cores of crystals are analyzed to determine if the zircon is inherited from an older source.

Zircon U/Pb analyses were conducted at the Arizona LaserChron Center housed at the University of Arizona. A Thermo-Finnigan Element2 single collector-inductively coupled plasma-mass spectrometer (SC-ICP-MS) was used to analyze U/Pb isotopic ratios. The following parameters are summarized from Gehrels (2010) and Ibanez et al. (2015) Table 1. The Element2 uses an Analyte G2 laser ablation system which utilizes a 193nm ArF excimer producing a 20-micron beam size and 30-micron pit depths. The energy fluence and attenuation are 7 J/cm^2 and 8%, respectively. Laser ablation repetition rate is 7 Hz with 560 pulses. The Element2 mass spectrometer runs at 1200 W forwarding power with low mass resolutions.

Prior to analysis on the Element2 SC-ICP-MS single zircon grains were mounted with standards of known ages. Approximately 50-60 zircon (unknowns) were mounted in rows. Subsequent to drying and setting of epoxy in mount, detailed cathodo-luminescence (CL) images of the sample were taken. CL images capture the detail of oscillatory zoning in zircons, which enables identification of zircon cores and aids in spot selection. Approximately 50-75 spots of rims and cores, identified from the CL images, are set into the operating program and the sample is analyzed. A sample with 75 spot analyses takes approximately 2 hours to run. Data is then reduced using an in-house python code and EGcalc macro program. Concordia diagrams and best-fit age plots are generated using Isoplot.

3.2.3 $^{40}Ar/^{39}Ar$ Thermochronology

$^{40}Ar/^{39}Ar$ thermochronology is a proxy isotopic dating system developed from the K/Ar system; it is a robust system used to solve a variety geological problems from crystallization ages of young volcanic rocks to cooling histories of plutonic rocks (McDougall and Harrison, 1999). The K/Ar system is a radiogenic decay process of ^{40}K to ^{40}Ar with a half-life of 1.2480 Byr. For $^{40}Ar/^{39}Ar$ geochronology, samples must be irradiated by neutrons from a nuclear reactor to convert stable ^{39}K to radiogenic ^{39}Ar. After irradiation at a nuclear reactor the sample is loaded into a mass spectrometer and heated with a resistance furnace in a stepwise fashion to release gases from the crystal lattice. Step heating allows for several analyses per sample, usually 13-15, which in turn yields insight to the argon distribution throughout the sample. For example, heating steps typically start at 660 ˚C and heat until fusion at 1,400 ˚C. At lower temperatures (initial steps), atmospheric gases that entered the lattice, usually through weathering and alteration, are released, these data can usually be rejected from the final age calculation. At higher temperatures, the step heating technique begins to liberate radiogenic gases which developed through radioactive decay and geologic processes. These steps usually yield similar ages and are plotted on an age spectrum plot. Samples that meet the plateau age restrictions usually yield the most reliable ages, with the lowest errors. For a sample to meet the plateau age restrictions, four or more consecutive heating steps, which release at least 50% of the total ^{39}Ar, must correspondence in age at 2 sigma uncertainties.

All sample were irradiated at the OSU TRIGA Reactor in Corvallis, OR and analyzed at the University of Nevada, Las Vegas in the Nevada Isotope Geochronology Labratory (NIGL) on the MAP 215-50 mass spectrometer. This is a low background and high sensitivity machine and is equipped with a triple collector assembly, Faraday cup, and a standard electron multiplier. Additionally, the MAP 215-50 runs a 4K cryogenic pump which separates noble gases. A quadrapole mass spectrometer is used for measuring gases prior to sample admission.

Nominal closure temperatures used in this study are 500 ± 50 ˚C for hornblende, 425 ± 25

˚C for muscovite, and 325 ± 50 ˚C for biotite (McDougall and Harrison, 1999; Harrison et al., 2009). Modeling of K-feldspar gas release, following the MDD theory and techniques described in Lovera et al., 1989; Lovera, 1992; Lovera et al., 1993; and Lovera et al., 2002, yield a continuous cooling history for the temperature interval 300˚C to 150˚C. Computer programs provided by Zietler (1993) were used to model domain size and distribution and diffusion kinetics (SizeExtractor), as well as inversion modeling (Arvert) of age spectra to obtain continuous cooling curves.

3.2.4 Structural Analysis

To constrain lithologic distributions as well as the extent and geometry of the mylonitic shear zone in the Bristol Mountains, geologic mapping was performed at the 1:24,000 scale across the range. Structural measurements were collected from mylonitic rocks (foliation and lineations) to constrain geometry as well as general hanging-wall transport direction of the shear zone. Furthermore, multiple oriented samples were collected from the shear zone for detailed kinematic and microstructural analyses. Thin sections were cut from oriented samples and analyzed using traditional petrographic techniques. Kinematic indicators such as sigmoidal grains (mica fish), shear bands of dynamically recrystallized minerals, and grains with strain shadows were used to determine overall shear sense. Microstructures were studied to constrain deformation mechanisms. Specifically, the mechanisms of dynamic recrystallization of quartz and feldspar grains were assessed to constrain deformation temperatures, assuming average geologic strain rates. Three regimes of dynamic quartz recrystallization have been demonstrated to indicate deformation temperatures (Guillope and Poirier, 1979; Poirier and Guillope, 1979; Cahn, 1983; Urai et al., 1986; Drury and Urai, 1990; Hirth and Tullis, 1992; Stipp et al., 2002), and are as follows: bulging recrystallization (BLG), regime 1, which is indicative of low deformation temperatures (280-

400˚C); subgrain rotation recrystallization (SGR), regime 2, is characterized by intermediate deformation temperatures (400-500˚C); and grain boundary migration recrystallization (GBM), or regime 3, occurs at high deformation temperatures (~500˚C). Constraining the temperatures of deformation from the mylonitic shear zone also provides insight into the timing of deformation by coupling isotope geochronology and thermochronology with deformation mechanisms.

To address the structural significance of the BCF and its role in exhuming the Granite Mountains and displacing the Bristol Mountains to the NW, as well as its relationship to the ductile shear fabrics present in the immediate footwall, the BCF was mapped systematically at a 1:12,000 scale and a detailed structural analysis of the fault zone was performed. Brittle striations and fault surfaces were measured along the brittle cap of the BCF, and compared with measurements of foliations and lineations within the mylonitic fabrics in the immediate footwall of the BCF. All measurements were plotted on equal area stereographic projections using software *Stereonet 9*. Oriented samples were collected from the mylonitic shear zone to determine kinematics and deformation mechanisms, using the same techniques as discussed above.

4. RESULTS

4.1 Bull Canyon Fault – Mapping and Structural Analysis

The BCF is exposed along the northern and northwestern base of the Granite Mountains, and forms an arcuate shape dipping NW away from the range (Figure 3a-b). It is demarked by zones of intense brecciation, highly fractured granitoid rocks, and well developed orange to red cataclasite and ultracataclasite (Figure 4). Structural measurements of the BCF show an average fault plane strike of 252˚ and dip of 41˚NW (Figure 3c). Furthermore, mechanical transport direction indicators such as slickensides and grooves and mullions, were measured to determine overall direction of hanging-wall transport. Average trend of kinematic indicators demonstrates a hanging-wall transport direction of 324˚ and plunge of 39˚ (Figure 3c). The age of the BCF is poorly constrained by cross-cutting relations with undated Tertiary gravel and breccia units, as well as the regional framework of extension in the Southern Basin and Range; the fault is thought to be Neogene in age. Tertiary gravel deposits and Tertiary landslide breccia units are interpreted as deposits formed during the final exhumation of the Granite Mountains in the Miocene (Howard et al., 1987).

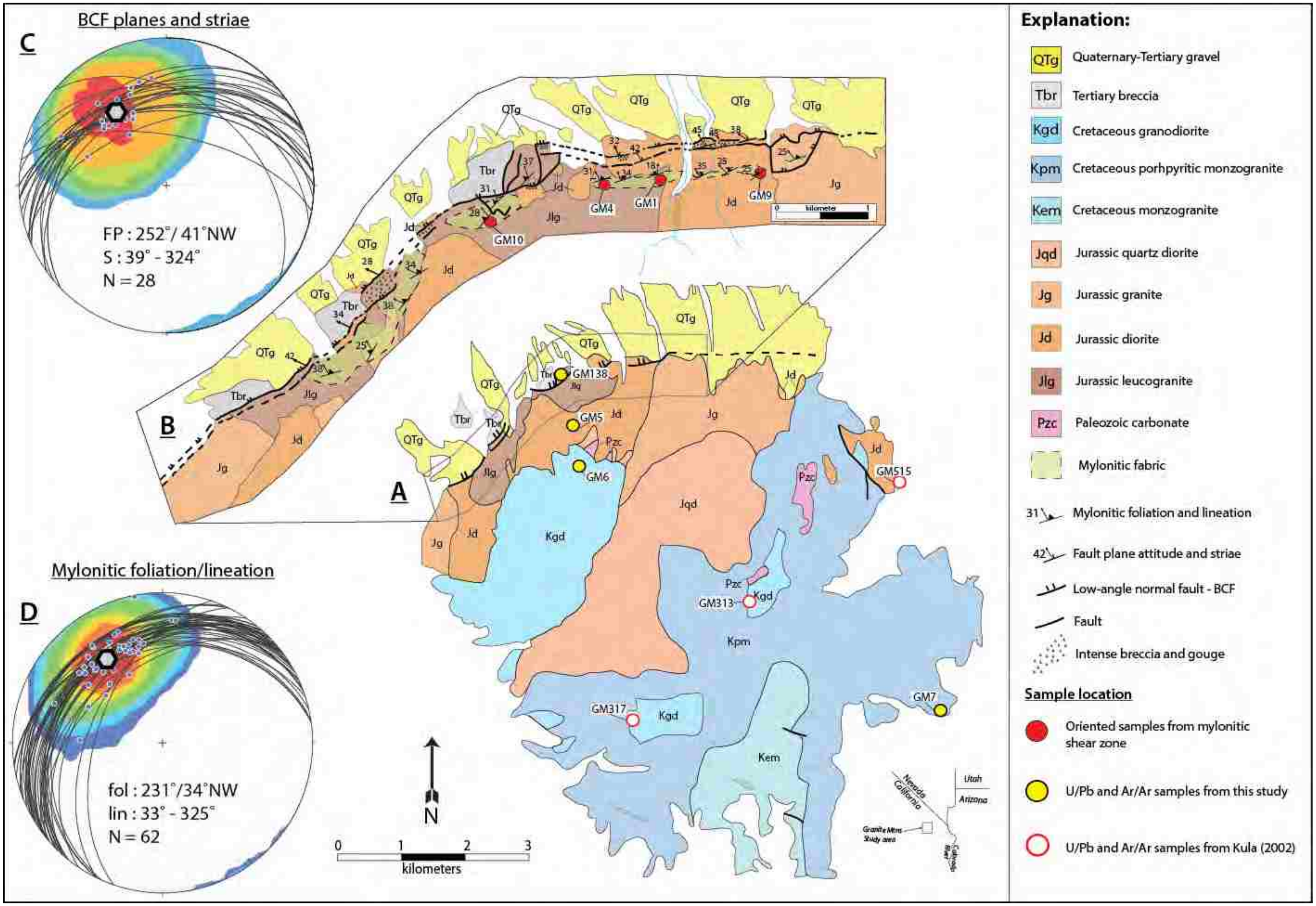
BCF planes and striae
C
FP : 252°/ 41°NW
S : 39° - 324°
N = 28
Mylonitic foliation/lineation
D
fol : 231°/34°NW
lin : 33° - 325°
N = 62
A
B
GM10
GM4
GM1
GM9
GM138
GM5
GM6
GM515
GM313
GM317
GM7
QTg
Tbr
Jd
Jlg
Jg
Jqd
Kgd
Kpm
Kem
Pzc
N
0
1
2
3
kilometers
Utah
Arizona
Nevada
California
Explanation:
QTg Quaternary-Tertiary gravel
Tbr Tertiary breccia
Kgd Cretaceous granodiorite
Kpm Cretaceous porhpyritic monzogranite
Kem Cretaceous monzogranite
Jqd Jurassic quartz diorite
Jg Jurassic granite
Jd Jurassic diorite
Jlg Jurassic leucogranite
Pzc Paleozoic carbonate
Mylonitic fabric
31 Mylonitic foliation and lineation
42 Fault plane attitude and striae
Low-angle normal fault - BCF
Fault
Intense breccia and gouge
Sample location
Oriented samples from mylonitic shear zone
U/Pb and Ar/Ar samples from this study
U/Pb and Ar/Ar samples from Kula (2002)

[redacted]

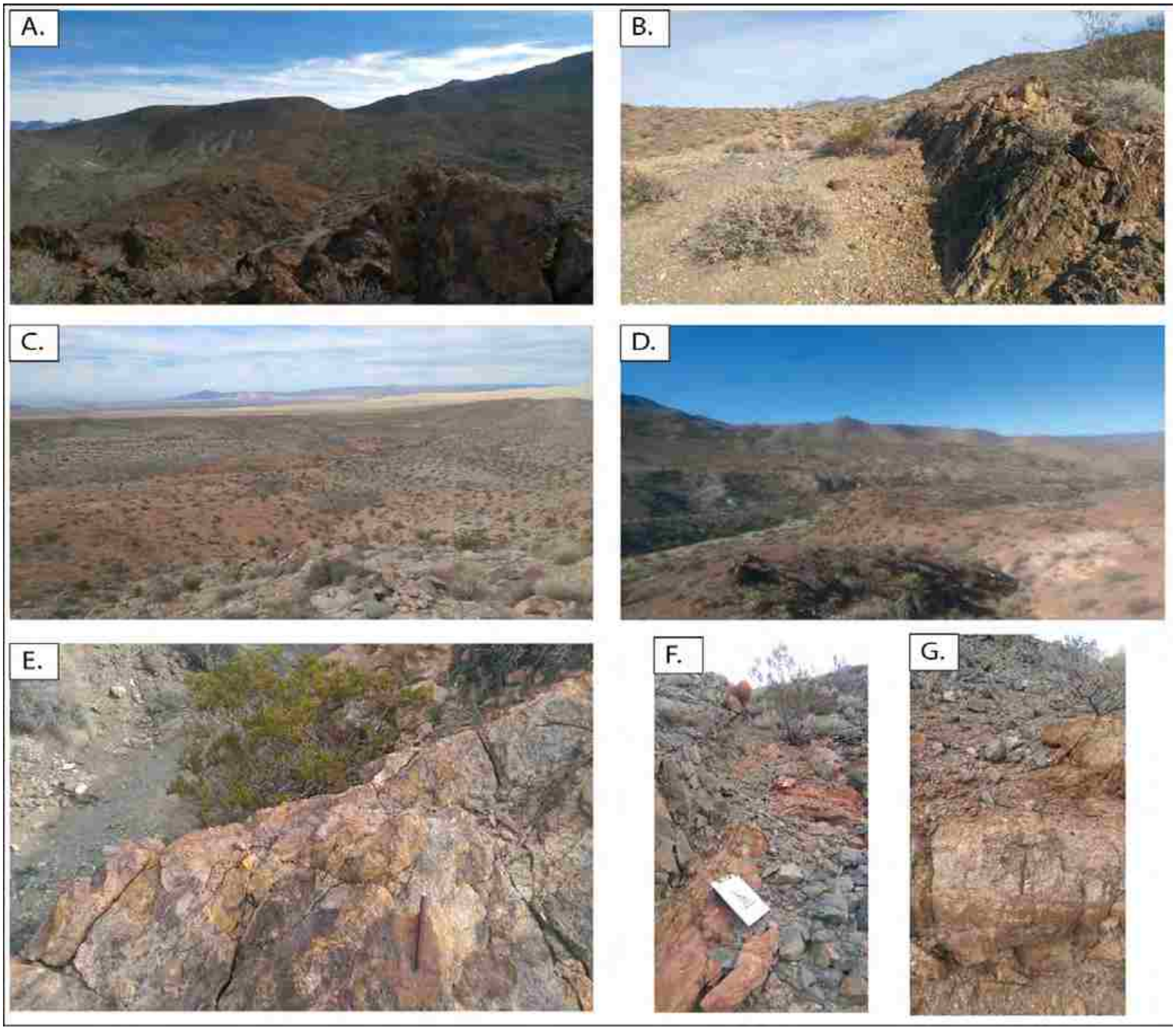

[redacted]

4.1.1 Footwall Geology

Rocks in the footwall of the BCF, in the northwestern Granite Mountains, are Jurassic leucogranites, granites, and diorites. These plutonic rocks are generally highly chloritized adjacent to the BCF, due to low-grade alteration. Solid-state mylonitic fabrics occur discontinuously throughout the immediate footwall of the BCF, dominantly developed in Jurassic leucogranite, including leucocratic sills within dioritic plutons. Structural measurements of localized mylonitic fabrics show a similar geometry and kinematics to the brittle-cap and principal slip-plane of the BCF. Mylonitically deformed rocks represent a structural thickness of ~500 m, below which Jurassic and Cretaceous granitoids are undeformed, preserving magmatic contacts, textures, and fabrics. Jurassic dioritic plutons show highly complex magma mixing textures and "spider-web dikes", indicating the Cretaceous plutonic suite intruded immediately below or adjacent to the Jurassic suite, causing complex interactions and magmatic processes to occur.

Mylonitic fabrics in the footwall of the BCF form a discontinuous belt of outcrops displaying solid-state shearing, and locally show chloritization and alteration due to BCF deformation. Structural measurements of mylonitic fabrics show an average foliation surface of 231˚ and dip of 34˚NW (Figure 3d). Trend and plunge of stretching lineations give an average transport direction of 325˚ and plunge of 33˚ (Figure 3d). Figure 3b shows sample locations for photomicrographs and samples discussed below.

The deformational style of mylonitic shear zones is best demonstrated by a detailed kinematic study of oriented thin sections, as well as observations at the outcrop and hand-sample scale. Kinematic indicators from thin sections unequivocally demonstrate top-to-the-NW, non-coaxial, down-dip sense of shear. Kinematic indicators include shear bands of dynamically recrystallized quartz with oblique grain shape fabric – with foliation defining S-C planes (Figure

5c) and sigmoidal and back-rotated feldspar grains (Figure 5a-b) with dynamically recrystallized tails. Tails of sigmoidal grains terminate at parallel C-planes, defined by wispy discontinuous planes of fine grained mica (Figure 5a-b) (Berthe et al., 1979; Lister and Snoke, 1984; Passchier and Simpson, 1986; Simpson and Wintsch, 1989; Passchier and Trouw, 1996; Passchier and Trouw, 2005).

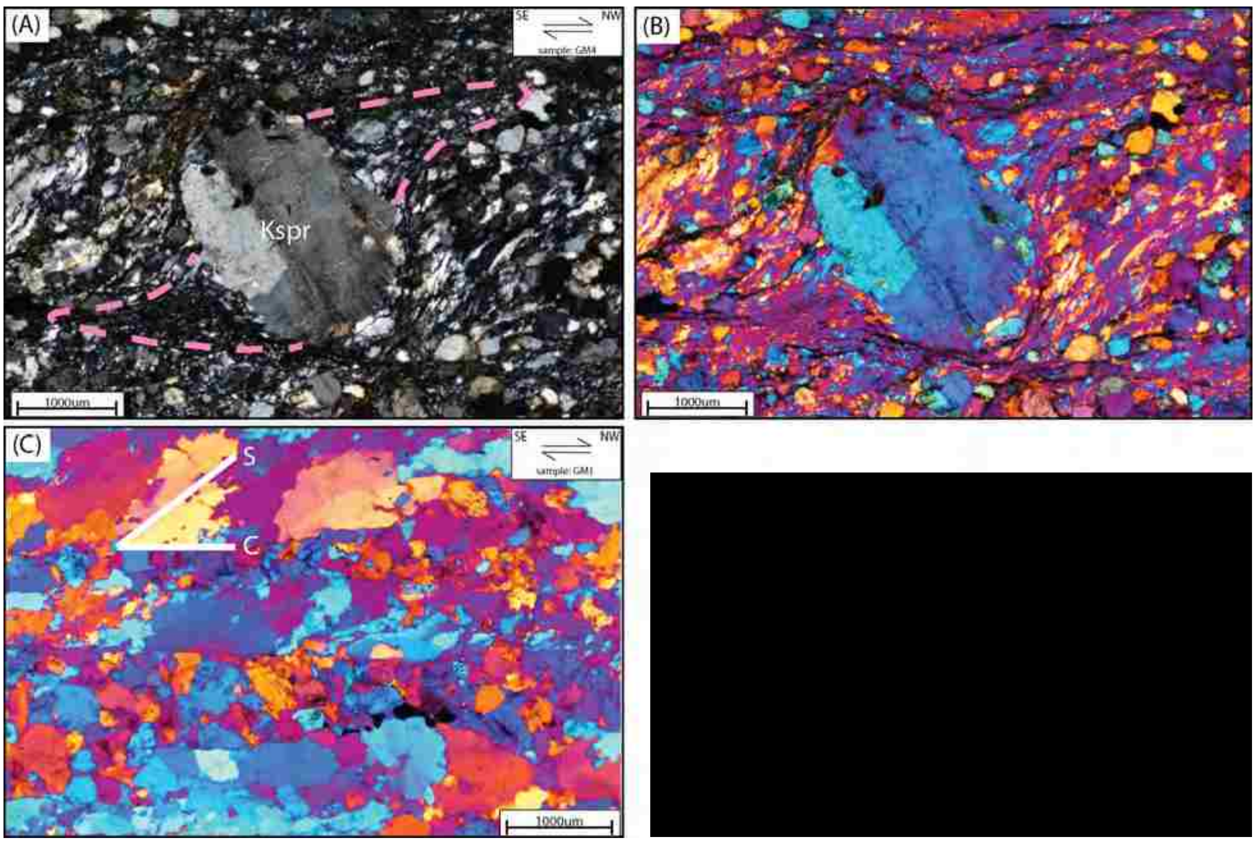

The degree of dynamically recrystallized quartz and feldspar provides insight into the temperature of deformation recorded in mylonitically deformed granitoid rocks. Specifically, three regimes of dynamic recrystallization are used to constrain deformation temperatures, discussed above. Microstructures from mylonites in the footwall of the BCF demonstrate shearing took place at upper greenschist to lower amphibolite facies conditions, and show that early higher temperature microstructures have been overprinted by a lower-grade, lower greenschist temperature conditions likely associated with either BCF deformation or progressive unroofing of the shear zone in the Late Cretaceous. Grain-size reduction is evident throughout the shear zone (Figure 6). Incipient gneissic fabric is evident in mylonite samples, segregating quartz and feldspar into distinct bands (Figure 6). Quartz bands display consistent grain boundary migration (GBM) recrystallization textures (Figure 6), correlating to regime 3 from Hirth and Tullis (1992) and Stipp et al. (2002). GBM recrystallization textures for quartz constrain deformation temperatures to 500˚C or greater. Plastic behavior and dynamic recrystallization of feldspar is indicative of high deformation temperatures. BLG recrystallization of feldspar is commonly observed at temperatures ranging from ~400 – 600 ˚C and SGR is common from ~500 – 550 ˚C (Figure 6) (Simpson, 1985; Gapais, 1989; Pryer, 1993; FitzGerald and Stunitz, 1993; Singleton and Moser, 2012). K-feldspar bands commonly show a sub-grain rotation (SRG) recrystallization texture (regime 2) further constraining deformation temperatures to ~550˚C (Figure 6) (Simpson, 1985; Gapais, 1989; Pryer, 1993; FitzGerald and Stunitz, 1993).

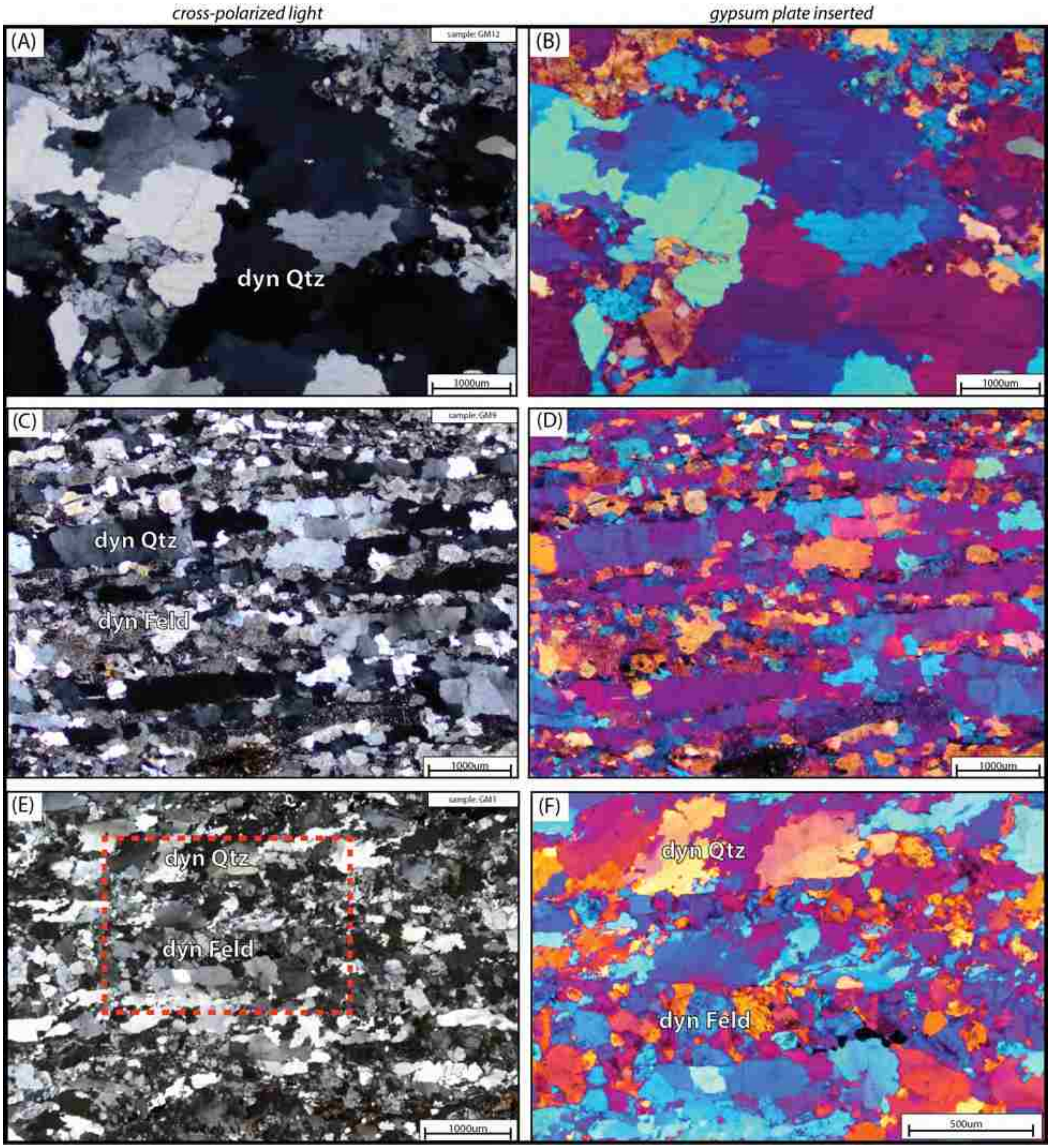
cross-polarized light
gypsum plate inserted
(A)
dyn Qtz
1000um
(B)
1000um
(C)
dyn Qtz
dyn Feld
1000um
(D)
1000um
(E)
dyn Qtz
dyn Feld
1000um
(F)
dyn Qtz
dyn Feld
500um

[redacted]

4.1.2 Hanging Wall (Upper Plate) Geology

Rocks in the hanging wall (HW) of the BCF are comprised of Quaternary-Tertiary gravel (QTg) deposits, Tertiary breccia (Tbr) units, and Jurassic diorite (Jd) with zones of intense gouge development, brecciation, and fracturing adjacent to the BCF. QTg fans are comprised of gravel to boulder sized clasts with lithologies consistent with plutonic lithologies present in the Granite Mountains. QTg units are assumed to be large fan deposits shed from the Granite Mountains during the final exhumational stages associated with the BCF. It is interpreted that they lie in fault contact with the BCF. However, ambiguous field relations allow for an alternative that at least the youngest parts of the deposits overlapped the BCF at one point and have since been eroded. Tbr units crop out in the immediate HW of the BCF locally and form low-hummocky topography with wide ranges of lithologies and colors resembling a melange. Large blocks of highly fractured plutonic rocks comprise the unit, though lithologies are indistinguishable. These are interpreted to be large slide blocks coming from the top of the Granite Mountains during Miocene extension and exhumation. Jurassic diorite that is in direct contact with the BCF is highly fractured with zones of breccia and gouge.

4.2 Bristol Mountains

4.2.1 Geologic Mapping

Geologic mapping was performed across a portion of the central Bristol Mountains at 1:24,000. Mapping demonstrates that plutonic lithologies are similar to those in the Granite Mountains (Figure 7a), though subtle phase variations do exist between plutons. Plutonic units include a large Cretaceous granodiorite pluton composed of quartz, feldspar and biotite - this pluton comprises most of the mapped area (Kgd) and forms large rounded, highly weathered and crumbly outcrops. Immediately west and north of Kgd is a more porphyritic phase (Kpg), with K-feldspar phenocrysts ranging in size from 0.5 – 2 cm; Kpg is much more resistant than Kgd, and forms steeper slopes with large boulders that are highly varnished, and holds up the highest peaks in the range. A large Cretaceous granitic pluton overlies Kpg in the central and western portions of the range (Kg). This unit is distinguished from Kgd and Kpg by the presence of salmon colored equigranular K-feldspar phenocrysts, ranging in size from 0.8 – 1 cm, and the noticeable low percent (<5%) of biotite, as compared to Kgd. Kg weathers as large sheets parallel to the mylonitic foliation and is highly varnished and resistant. Jurassic diorite (Jd) lies along the western flank of the range. In the NW portion of the map area the diorite is in shear-zone contact with the highly-deformed Kg, and is undeformed. To the SSE the Jd pluton is mylonitically deformed and is in intrusive contact with Jg and Kgd (Figure 7a). The Jd pluton caps Kg to the east, and resembles a large sill-like intrusion (Figure 7b and 8).

4.2.2 Mylonitic Shear Zone

A solid-state, high-strain, mylonitic shear zone is mapped in the western and southern portion of the range, deforming all units, and most notably Kg (Figure 7a). The shear zone deforms Jd in the south, demonstrating high strain fabrics and S>L textures. Moving NW, mylonitic deformation is most prevalent in unit Kg. Deformation within Kg displays variable protomylonite to ultramylonite textures. Predominately, the highest strain observed is partitioned into more quartz-rich sills within Kg, displaying elongated quartz grains with high aspect ratios. Moreover, strain is highest at the western-most upper margin of the shear zone where Kg is in contact with

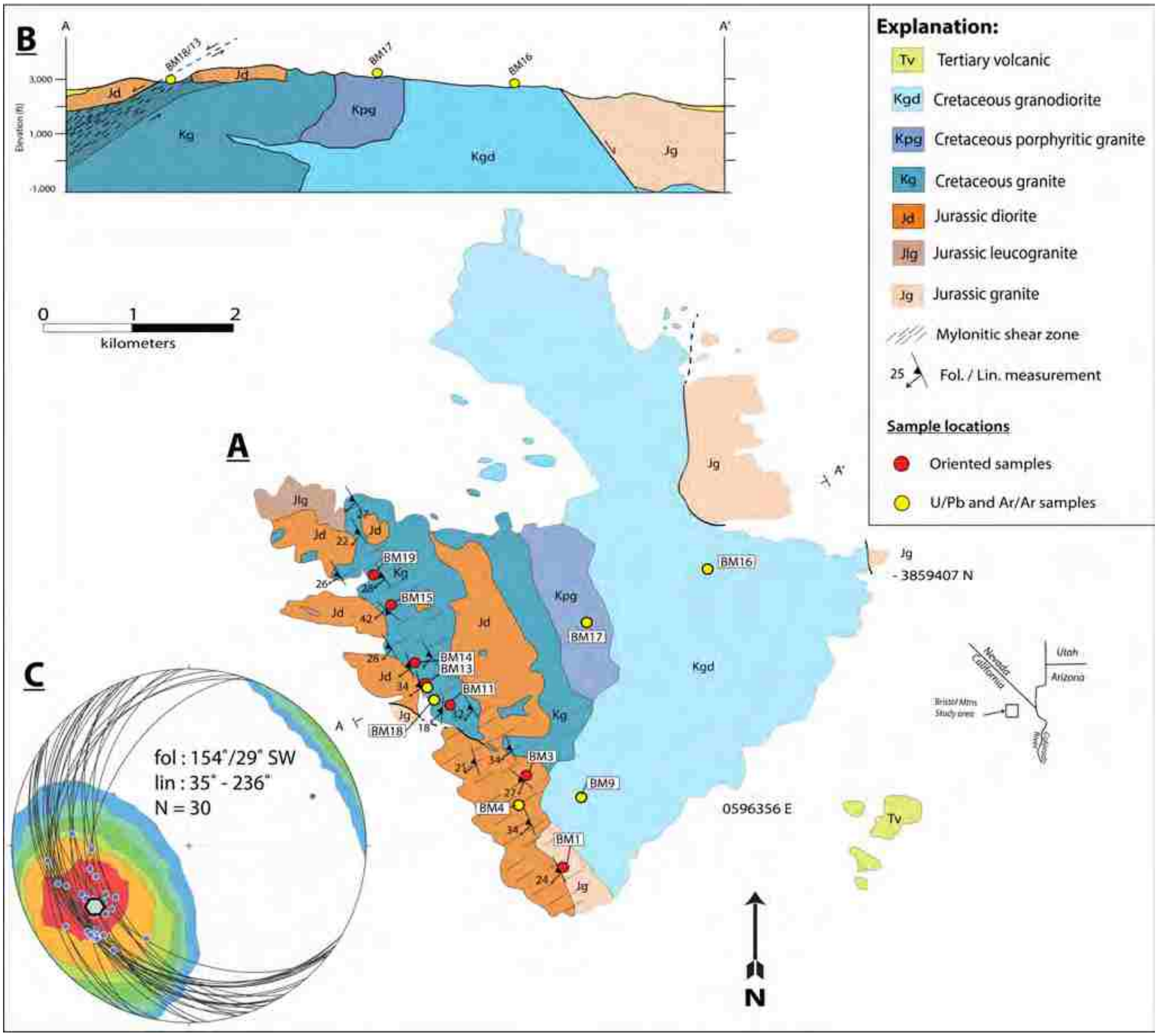
B
A
A'
BM18/13
BM17
BM16
3,000
1,000
-1,000
Elevation (ft)
Jd
Kg
Kpg
Kgd
Jg
Explanation:
Tv Tertiary volcanic
Kgd Cretaceous granodiorite
Kpg Cretaceous porphyritic granite
Kg Cretaceous granite
Jd Jurassic diorite
Jlg Jurassic leucogranite
Jg Jurassic granite
Mylonitic shear zone
25 Fol. / Lin. measurement
Sample locations
Oriented samples
U/Pb and Ar/Ar samples
0 1 2
kilometers
A
Jlg
BM19
BM15
BM14
BM13
BM11
BM18
BM3
BM4
BM1
BM9
Tv
- 3859407 N
0596356 E
Nevada
California
Utah
Arizona
N
C
fol : 154°/29° SW
lin : 35° - 236°
N = 30

[redacted]

Jd to the immediate west. Unit Jd, here, is undeformed and the shear zone is interpreted to extend beneath Jd in the subsurface, within Kg, for an unknown horizontal distance (Figure 7b). The total thickness of the shear zone is unknown, as the outcrop nature is seemingly a "window" looking through the undeformed Jd unit into the deformed Kg. In the southern portion of the shear zone the minimum thickness estimate from map pattern is ~ 500 –1000 m.

[redacted]

Structural measurements were collected along the length of the shear zone to determine the overall extent, geometry, and kinematics. Multiple oriented samples were collected to perform a microstructural analysis and determine deformation mechanisms, as well as shear sense. Sample locations for oriented thin sections discussed are shown in Figure 7a. Chiefly, the shear zone strikes NW-SE and dips gently to the SW. The highest strain portion, as determined from field observations, of the shear zone is at its top, at the contact with undeformed Jd along the central length of the shear zone (Figure 8). Moving from the highest strained portion of the shear zone down the structural section to the NE, strain generally decreases down structural section for ~ 1 km, where it is no longer observable. Foliation within the shear zone has an average strike of 154˚ and dip of 29˚ SW. Stretching lineations indicate a transport direction of ~236˚ SW and plunge of 35˚SW (Figure 7c).

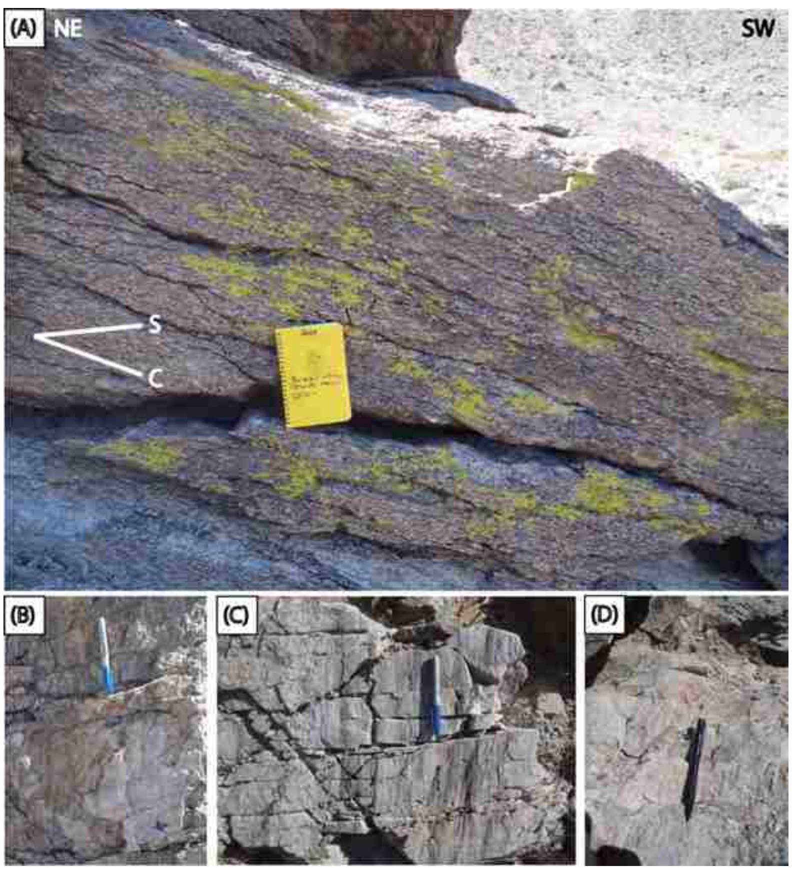

[redacted]

Kinematic indicators are abundant throughout the shear zone, and unequivocally demonstrate non-coaxial shearing with a top-to-the-SW down-dip sense of shear. Kinematic indicators include myrmekite quarter structures (Figure 10e-f), dynamically recrystallized quartz ribbons with oblique grain shape fabrics (Figure 10c-d), sigmodial muscovite fish (Figure 10a-b), feldspar porphyroclasts with sigmoidal tails (Figure 13e-f), as well as well-developed S-C fabrics (Figure 9a) (Berthe et al., 1979; Lister and Snoke, 1984; Passchier and Simpson, 1986; Simpson and Wintsch, 1989; Passchier and Trouw, 2005).

Deformation mechanisms were studied from microstructures, specifically, the degree and style of dynamically recrystallized quartz and feldspar, to determine the temperature of deformation. Deformation mechanisms indicate plastic deformation occurring from upper greenschist to lower amphibolite facies conditions. K-feldspar shows dynamic recrystallization throughout the shear zone, specifically around tails of porphyoclasts. Furthermore, strain-induced myrmekite is evident along K-feldspar porphyroclast boundaries. Grain boundary migration recrystallization of quartz is apparent in every sample studied, indicating deformation occurred at temperatures in the range of 450-550˚C. Plastic deformation of K-feldspar may indicate deformation temperatures likely exceeded 500-550˚C (Figure 11) (Simpson, 1985; Simpson and Wintsch, 1989; Gapais, 1989; Pryer, 1993; FitzGerald and Stunitz, 1993).

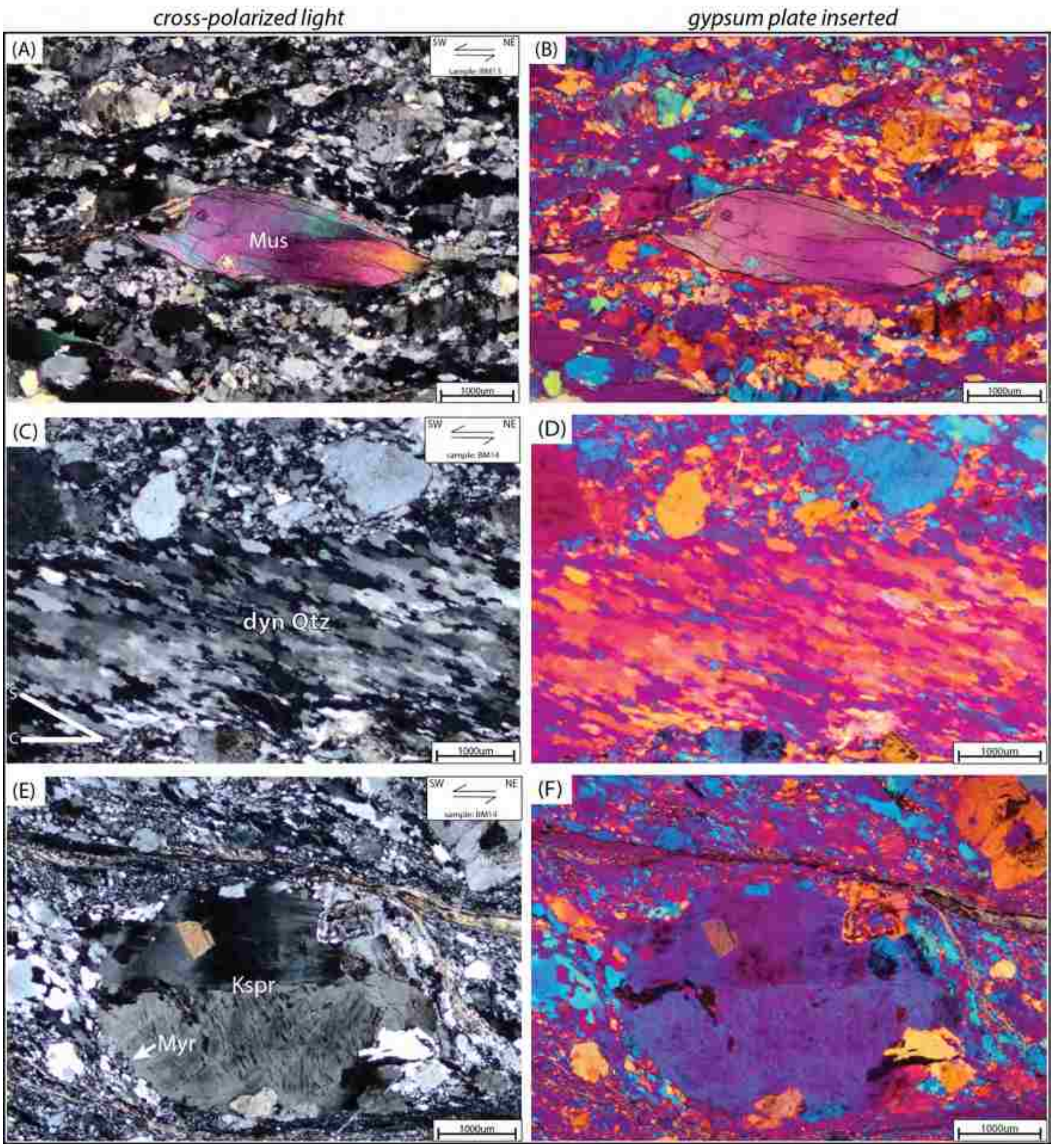
cross-polarized light
gypsum plate inserted
(A)
SW
NE
Mus
(B)
(C)
dyn Qtz
S
C
(D)
(E)
Kspr
Myr
(F)
1000um

[redacted]

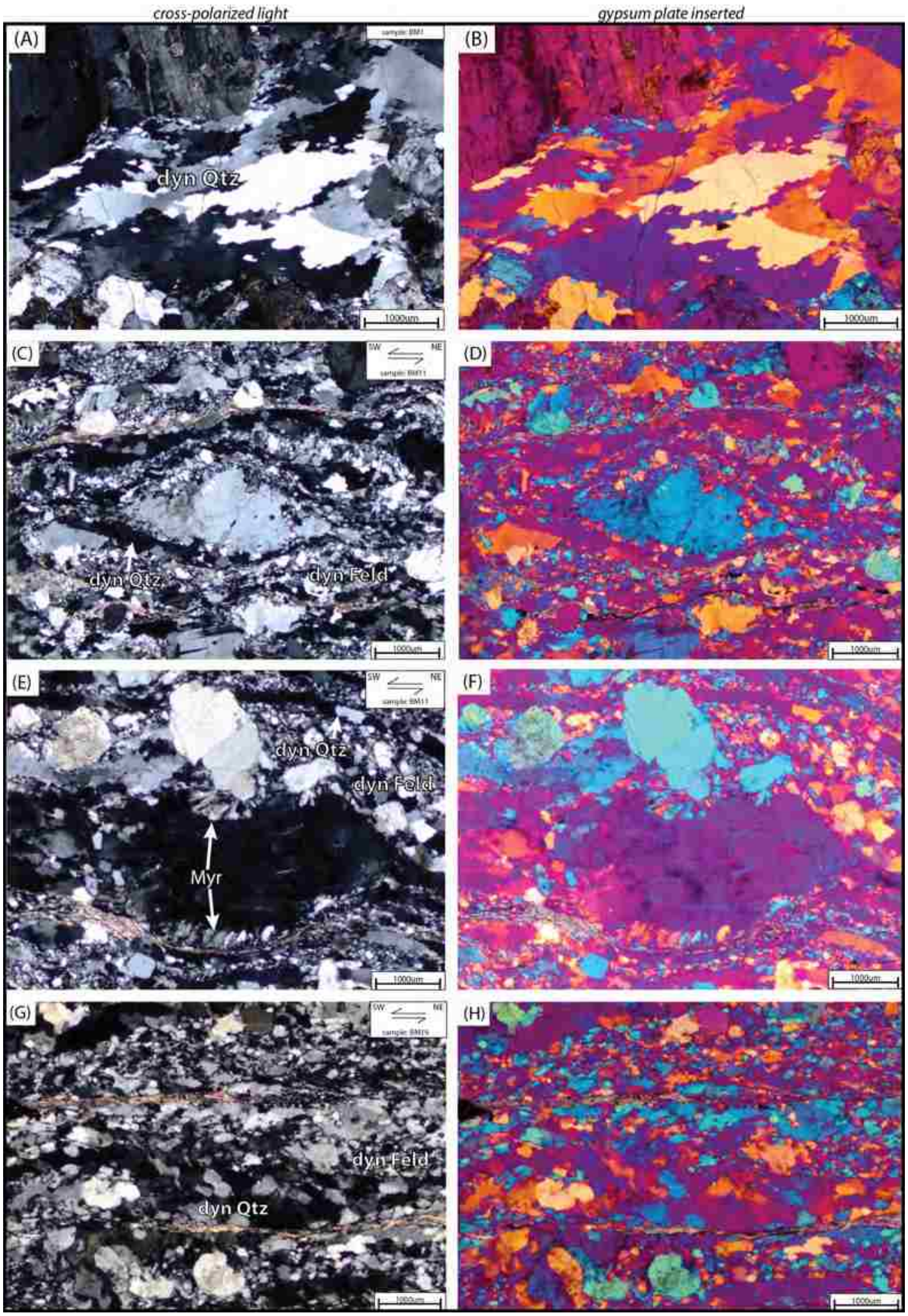
cross-polarized light
gypsum plate inserted
(A)
(B)
dyn Qtz
(C)
(D)
SW
NE
dyn Qtz
dyn Feld
(E)
(F)
dyn Qtz
dyn Feld
Myr
(G)
(H)
dyn Feld
dyn Qtz

[redacted]

4.3 U/Pb Geochronology

Three samples from the Bristol Mountains were collected for zircon U/Pb geochronology to constrain crystallization ages for Jurassic (BM4) and Cretaceous (BM9 and BM18) plutons (Figure 7). Additionally, seven samples were analyzed from the Granite Mountains for zircon U/Pb analyses. Three of the samples were reanalyzed from the sampling transect of Kula (2002) - (GM515 (NE), GM313 (Central), and GM317 (SW)) - to increase the accuracy and precision of the earlier analyses. For example, Kula (2002) reported zircon ages younger than hornblende $^{40}Ar/^{39}Ar$ cooling ages, motivating the refinement of crystallization ages, reported here. Four new samples were analyzed in this study; two from Cretaceous plutons on a sampling transect from SE to NW (GM7(SE) and GM6(NW)), parallel to the transport direction of the BCF and mylonitic shear fabrics, and two from Jurassic rocks including a dioritic pluton (GM5) and a leucogranitic pluton (GM138) (Figure 3). The Jurassic leucogranite sample was previously analyzed by Kula (unpublished) for K-feldspar thermochronology, which showed a very different cooling history than Cretaceous plutons. These data are reported below at 2 sigma uncertainties.

4.3.1 Bristol Mountains

Samples BM4, BM9, and BM18 from the Bristol Mountains were analyzed for zircon U/Pb geochronology to obtain crystallization ages for Cretaceous and Jurassic plutons. Sample locations are shown in Figure 12. The Jurassic pluton analyzed yielded an age of ~157 Ma and showed no inheritance or core and zoning textures. Cretaceous plutons yielded indistinguishable ages of ~75 Ma and both samples showed cores and detailed zoning textures. Cretaceous plutons show inherited cores ranging from Early Cretaceous and Late-to-Middle Jurassic ages and some Cambrian and Precambrian core ages.

Sample BM9 targeted a Cretaceous granodiorite pluton, mapped as Kgd, and yielded thirty-two spot analyses from crystal rims, ranging in age from 72.3-82.5 Ma and a weighted mean $^{206}Pb/^{238}U$ age of 75.68±1.3 Ma (Figure 12a), with a 95% confidence and MSWD of 1.09. Additionally, eighteen inherited cores were analyzed in this sample of mostly Early Cretaceous and Mid-to-Late Jurassic ages, with two core ages of 527.1±12.4 Ma and 1709.5±12.8 Ma. The inherited core ages are consistent with surrounding country rock ages as well as basement rock ages. Sample BM-18 was collected from a Cretaceous (Kg) pluton located within the mylonitic shear zone in the western portion of the range. Forty-six spot analyses were obtained from crystal rims and cores. Twenty-six rim analyses yielded a weighted mean $^{206}Pb/^{238}U$ age of 75.55±1.2 Ma with a 98% confidence and an MSWD of 1.08 (Figure 12b). The remaining twenty core analyses yielded inheritance ages from Early Cretaceous to Mid-to-Late Jurassic, and two ages at 1085.7±14.1 Ma and 1097.8±22.1 Ma. The inherited core ages are consistent with surrounding country rock ages as well as basement rock ages. Sample BM4 targeted a Jurassic dioritic pluton, mapped as Jd, and yielded a weighted mean $^{206}Pb/^{238}U$ age of 157.3±1.7 Ma (Figure 12c). Fifty- six spot analyses were obtained from this sample with ages ranging from 148-168 Ma, yielding the mean $^{206}Pb/^{238}U$ age with 95% confidence and an MSWD of 1.19. No inherited cores were found in this sample.

4.3.2 Granite Mountains

Seven samples were analyzed from the Granite Mountains to obtain crystallization ages for Cretaceous and Jurassic plutons. Three samples were reanalyzed from Kula (2002) – GM515 (NE), GM313 (Central), and GM317 (SW) - and four additional samples were analyzed (GM7 (SE), GM6 (NW), GM5, and GM138) for this study. Results presented below are at 2 sigma errors. Sample locations are shown in Figure 3.

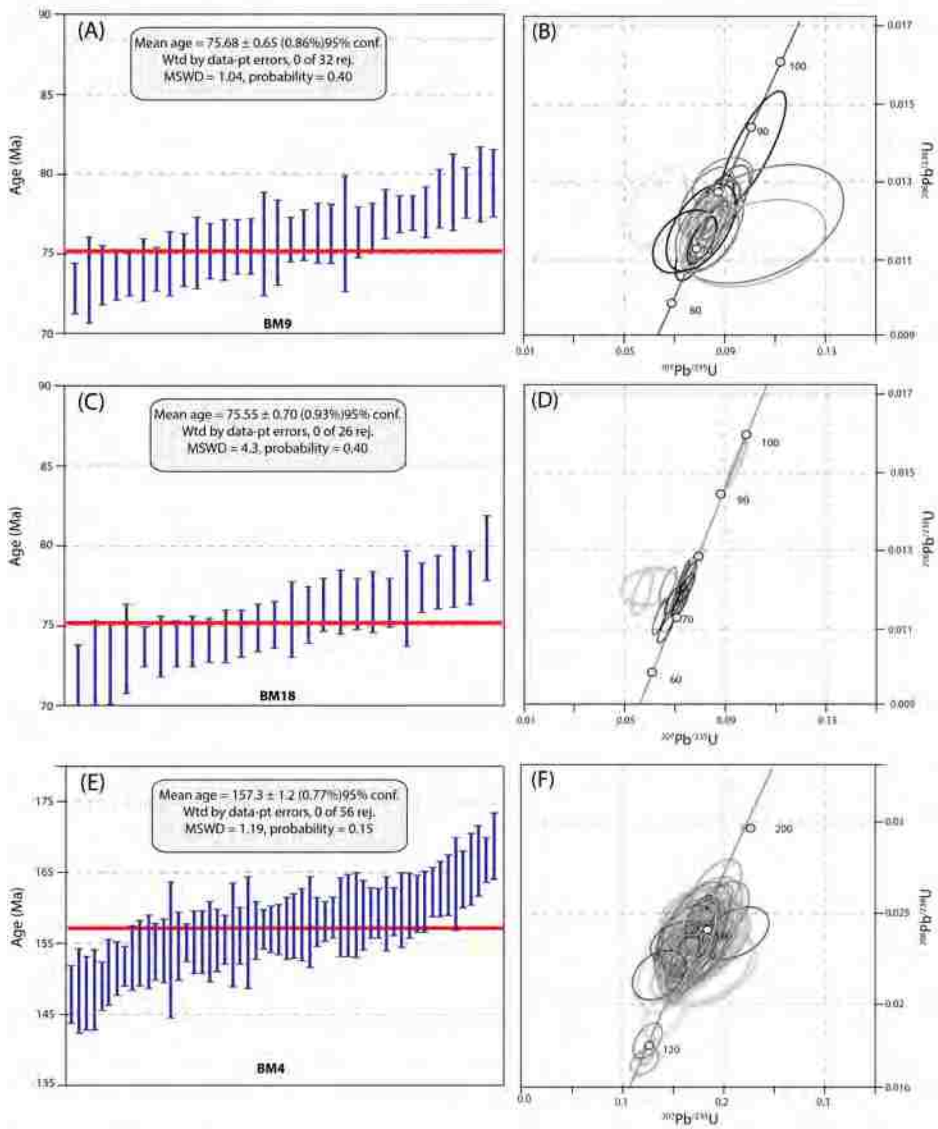

[redacted]

Sample GM515 was collected from the NE portion of the Granite Mountains by Kula (2002), from a pluton mapped as Kgd. Kula (2002) reported an age of 76.0 ± 3.3 Ma (MSWD = 1.80) for this sample from a total of eight analyses. A total of sixty new spot analyses were obtained to constrain the age of this pluton. Fifty-eight analyses yielded a weighted mean $^{206}Pb/^{238}U$ age of 78.61±0.9 Ma (MSWD = 0.84). Two inherited cores were analyzed from this sample yielding ages of 115.1±5.6 Ma and 156.6±8.4 Ma. The new results obtained for this sample have a much lower error and MSWD value, constrained by fifty-eight analyses, furthering the confidence for the age of crystallization for the pluton. Sample GM313 was collected by Kula (2002) from a granodiorite pluton mapped a Kgd in the central portion of the Granite Mountains (Figure 3). A total of fifty- one new spot analyses yield a mean age of 77.18±0.6 Ma (MSWD 0.83). Six analyses from inherited cores yielded ages from Early Cretaceous and Mid-to-Late Jurassic. Sample GM317 was sampled by Kula (2002) from the SW Granite Mountains, from a Cretaceous granodiorite pluton. A total of sixty spot analyses were obtained from this sample. Fifty-nine analyses yielded a weighted mean $^{206}Pb/^{238}U$ age of 75.55±0.81 Ma (MSWD = 1.3). One analysis yielded an age of 97.2±3.4 Ma and is interpreted as an inherited core and was excluded from the final age calculation. Figure 13 shows detailed CL images of single zircon crystals from the Granite Mountains, demonstrating complex zoning and cores of Cretaceous zircons. Weighted mean plots and concordia diagrams are shown in Figure 14.

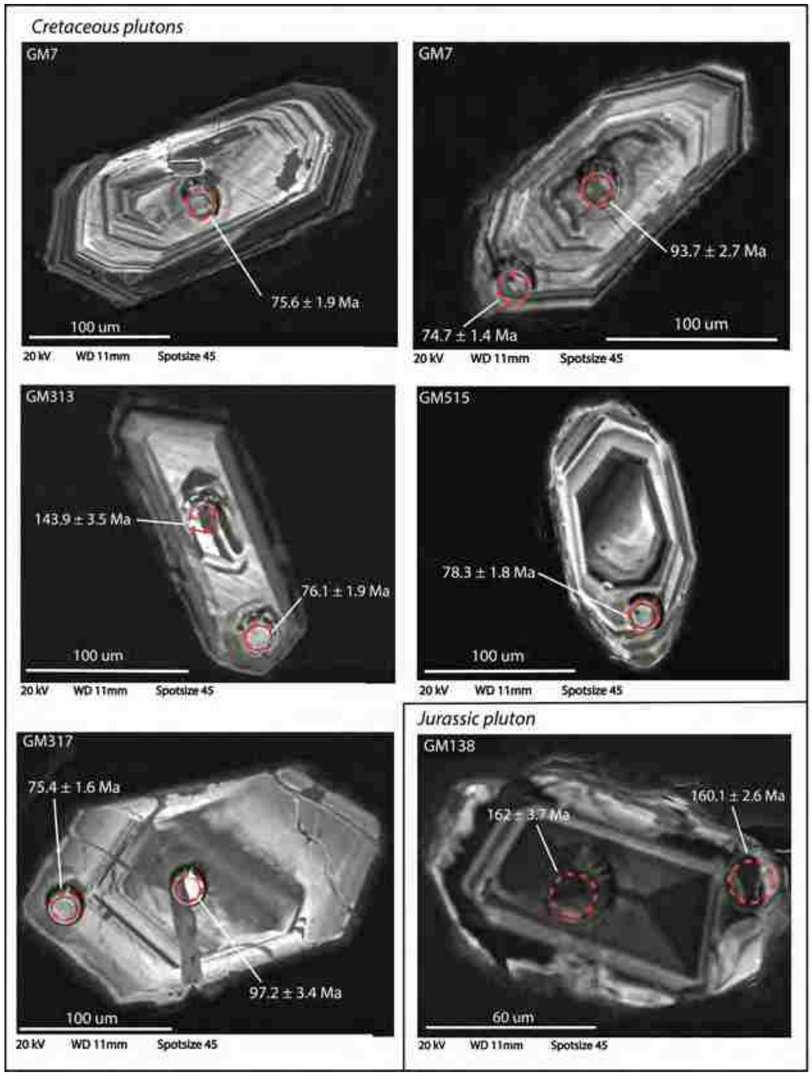

[redacted]

New samples added form a transect SE-NW, and utilize the sample (GM313) from Kula (2002). Sample GM7 was collected from the SE portion of the Granite Mountains from the large, voluminous, Cretaceous porphyritic monzonite mapped as Kpm. A total of forty-nine spot analyses were obtained from this sample, of which forty-eight analyses yielded a weighted mean $^{206}Pb/^{238}U$

age of 74.19±0.44 Ma (MSWD = 3.0). One analysis yielded an age of 93.7±2.7 Ma, interpreted to be an inherited core. Sample GM6 was collected from a hornblende-bearing Cretaceous granodioritic pluton (Kgd) located in the NW Granite Mountains. This sample is located nearest to the mylonitic shear zone, as well as the BCF. Fifty-one spot analyses were obtained from cores and rims of crystals. One analysis yielded a highly discordant analysis and was rejected from the data. Eight cores were analyzed yielding ages ranging from Early Cretaceous to Late Jurassic and one yielding an age of 1582.1±22.2 Ma (not shown in plots). The remaining forty-two analyses yielded a weighted mean $^{206}Pb/^{238}U$ age of 80.43±0.62 Ma (MSWD = 1.10).

Sample GM-5 was collected from a Jurassic diorite pluton, located in the NW portion of the range, mapped as Jd. A total of thirty-seven spot analyses were obtained from this sample. Five analyses yielded discordant ages; these analyses were rejected from the age calculation. The remaining thirty-two analyses yielded a weighted mean $^{206}Pb/^{238}U$ age of 158.1±1.4 Ma (MSWD = 1.07). The mean age of 158.1±1.4 Ma is interpreted to be the crystallization age for this pluton. This is within analytical error of the age from the Jurassic diorite dated in the Bristol Mountains. Sample GM138 was collected by Kula (unpublished) from a Jurassic leucogranite, within the hanging wall of the BCF. Fifty-eight spot analyses were obtained from this sample. Three analyses were rejected from the dataset; two were interpreted as inherited ages, and one was anomalously young, which is likely a bad analysis or significant Pb loss had occurred. The remaining fifty-five analyses were used to determine the crystallization age for this pluton. These data yielded a weighted mean $^{206}Pb/^{238}U$ age of 160.3±1.2 Ma (MSWD =1.8).

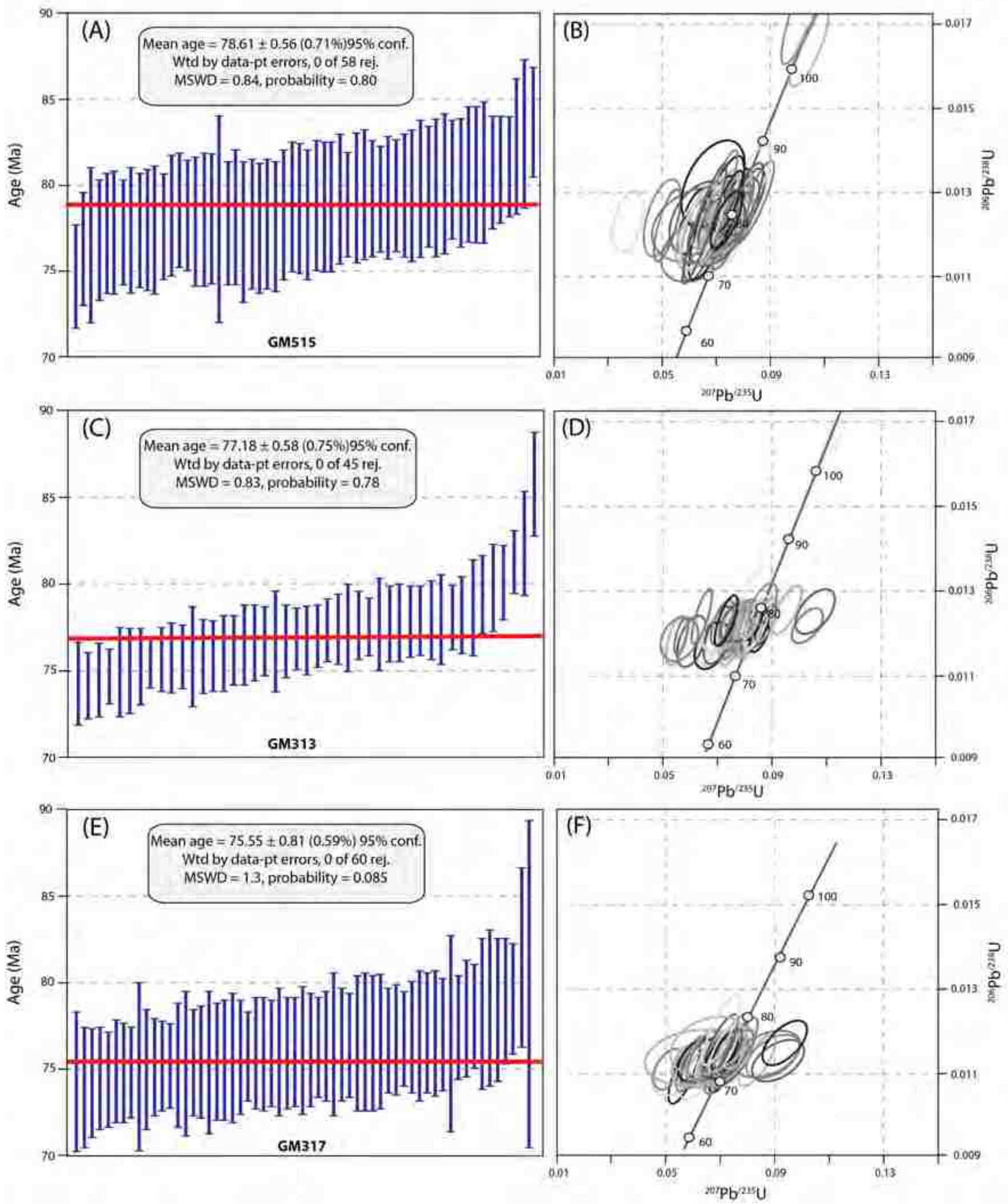
(A)
Mean age = 78.61 ± 0.56 (0.71%)95% conf.
Wtd by data-pt errors, 0 of 58 rej.
MSWD = 0.84, probability = 0.80
Age (Ma)
GM515
(B)
(C)
Mean age = 77.18 ± 0.58 (0.75%)95% conf.
Wtd by data-pt errors, 0 of 45 rej.
MSWD = 0.83, probability = 0.78
GM313
(D)
(E)
Mean age = 75.55 ± 0.81 (0.59%) 95% conf.
Wtd by data-pt errors, 0 of 60 rej.
MSWD = 1.3, probability = 0.085
GM317
(F)
207Pb/235U
206Pb/238U

[redacted]

[redacted]

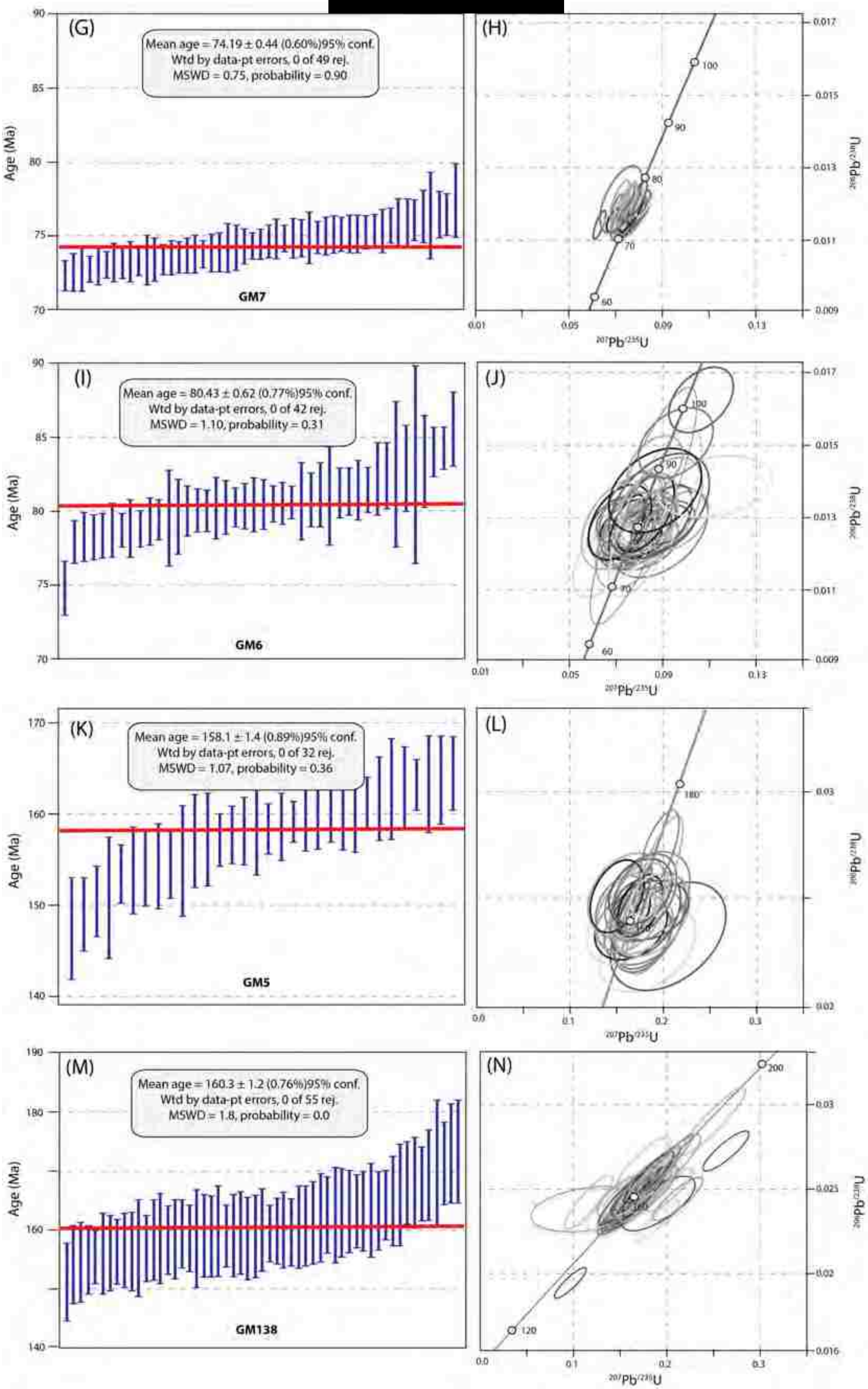

(G)
Mean age = 74.19 ± 0.44 (0.60%)95% conf.
Wtd by data-pt errors, 0 of 49 rej.
MSWD = 0.75, probability = 0.90
GM7
Age (Ma)
(H)
207Pb/235U
206Pb/238U
(I)
Mean age = 80.43 ± 0.62 (0.77%)95% conf.
Wtd by data-pt errors, 0 of 42 rej.
MSWD = 1.10, probability = 0.31
GM6
(J)
(K)
Mean age = 158.1 ± 1.4 (0.89%)95% conf.
Wtd by data-pt errors, 0 of 32 rej.
MSWD = 1.07, probability = 0.36
GM5
(L)
(M)
Mean age = 160.3 ± 1.2 (0.76%)95% conf.
Wtd by data-pt errors, 0 of 55 rej.
MSWD = 1.8, probability = 0.0
GM138
(N)

4.4 $^{40}Ar/^{39}Ar$ Thermochronology

Five samples from the Bristol Mountains were collected from the footwall and from within the mylonitic shear zone for $^{40}Ar/^{39}Ar$ thermochronology analyses. Samples were collected on a transect parallel to transport direction of the shear zone, spanning the footwall on spacing intervals of ~1 km. Sample locations are shown in Figure 7. From the five samples we analyzed four biotite, one muscovite, and two K-feldspar separates to determine thermal histories of Cretaceous plutons. Additionally, two samples from the Granite Mountains were collected for $^{40}Ar/^{39}Ar$ thermochronology to build off the dataset of Kula (2002). Kula (2002) presented hornblende and K-feldspar analyses from three locations across the Granites Mountains on a NE-SW sampling transect. This study utilized the central sample of Kula (2002) to assess the cooling history along a sampling transect that is parallel to the BCF and shear zone transport direction. From the two additional samples in the Granite Mountains, one hornblende, two biotite, and two K-feldspar separates were analyzed.

4.4.1 Bristol Mountains

Muscovite and Biotite

Four biotite (B) and one muscovite (M) were sampled from the Bristol Mountains transect, and are reported below. Biotite in the four samples are of magmatic origin, being a dominant rock forming mineral. Muscovite bearing rocks were only found within highest strain mylonite to ultra-mylonite along the western boundary of the shear zone.

Sample BM16 yielded a pseudo-plateau biotite age of 73.65±0.35 Ma, for steps 2-8, and a total gas age of 72.46 ± 0.24 Ma (Figure 15a). Sample BM17 yielded a preferred biotite age of 73.37±0.44 Ma, and a total gas age of 72.55±0.24 Ma. This sample did not meet the requirements for a plateau age. Step 10 yielded a slightly older age than steps 2-9 and 11-14. Removing steps

1 and 10 yields the preferred age (Figure 15b). Biotite sample BM18 from the mapped Kg unit is located within the mylonitic shear zone, adjacent to the sample BM13. This sample yielded a total gas age of 75.17±0.07 Ma. Steps 1 and 2, as well as step 12 yielded low argon release. Steps 3 through 11, with >90% ^{40}Ar release, were used to determine a preferred age of 74.97±0.22 Ma (Figure 15c). This age is within analytical error of the U/Pb zircon crystallization age. Sample BM9 yielded a preferred biotite age of 71.94±0.24 Ma, and a total gas age of 71.23±0.24 Ma. Step 9 yielded a slightly younger age than steps 2-8 and 10-14 making this sample fail the plateau age constraints. Step 1 and 9 were removed to obtain the preferred age for this sample (Figure 15d). Muscovite from sample BM13, from within the shear zone, yielded a plateau age of 72.57±0.80 Ma, from steps 1-13 (Figure 15e). This sample yielded a slightly higher error despite the well- constrained plateau age, due to decreased mass spectrometer sensitivity at the time of analysis. The muscovite plateau age of 72.57±0.80 Ma, from sample BM13 is interpreted to be best age for cooling for this pluton. As it is unlikely to expect significant differences in cooling over such short distances, we regard sample BM18 biotite to be affected by excess Ar.

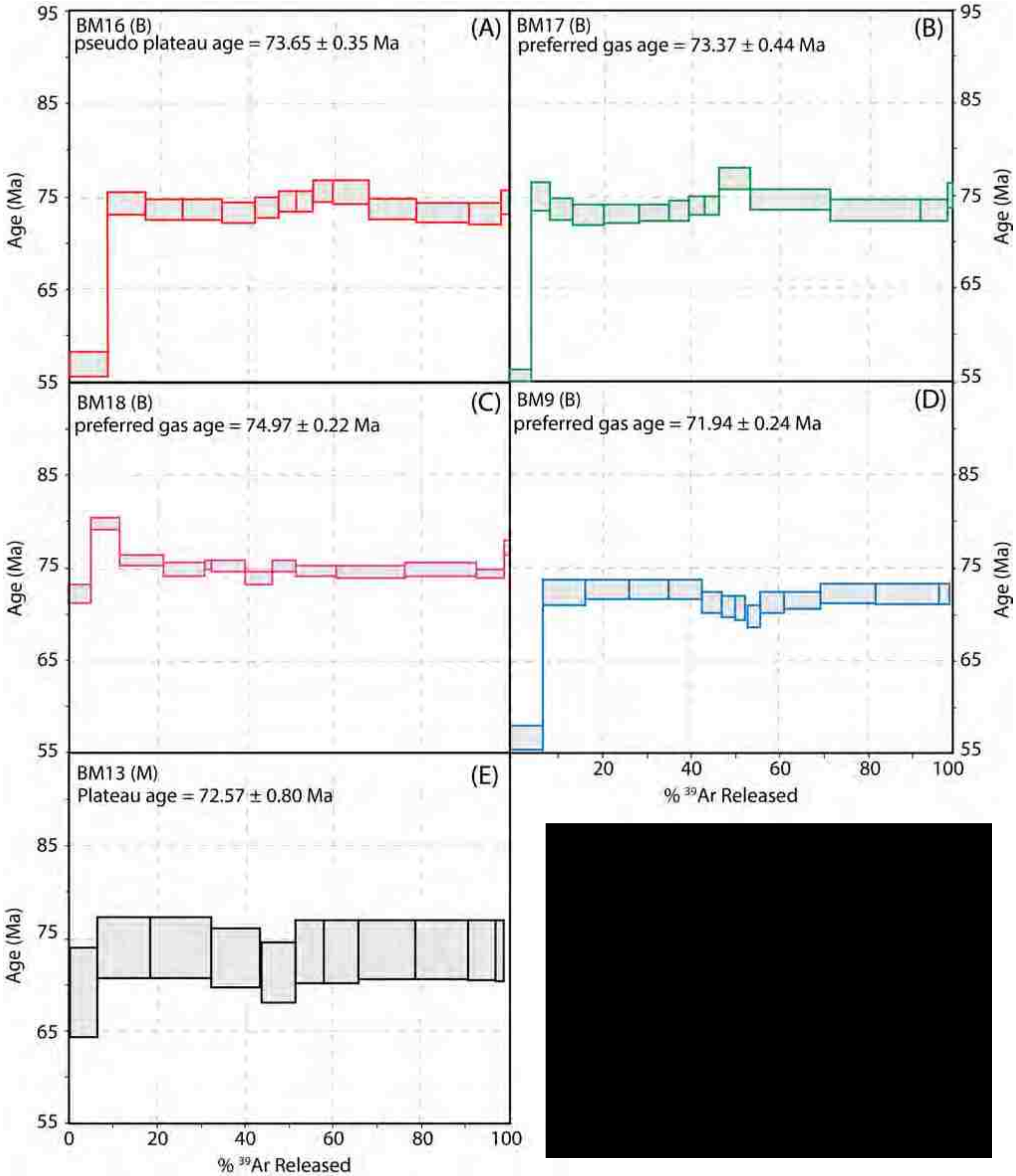
BM16 (B)
pseudo plateau age = 73.65 ± 0.35 Ma
(A)
BM17 (B)
preferred gas age = 73.37 ± 0.44 Ma
(B)
BM18 (B)
preferred gas age = 74.97 ± 0.22 Ma
(C)
BM9 (B)
preferred gas age = 71.94 ± 0.24 Ma
(D)
BM13 (M)
Plateau age = 72.57 ± 0.80 Ma
(E)
Age (Ma)
95
85
75
65
55
0
20
40
60
80
100
% 39Ar Released

[redacted]

K-feldspar

Two K-feldspar separates were analyzed from the Bristol Mountains transect to constrain the lower temperature thermal history for Late Cretaceous plutons. One sample was collected from the NE portion (BM16) of the transect, and the other was collected from within the shear zone (BM18) on the SW portion of the transect (Figure 7). These samples and analyses provide insight into the lower temperature cooling histories of the mylonitic shear zone, and the footwall ~2 km from the shear zone.

Sample BM16 was collected from the Cretaceous granodiorite (Kgd) pluton on the NE portion of the mountain range (Figure 7). BM16 K-feldspar yielded an $^{40}Ar/^{39}Ar$ age spectrum with a total gas age of 73.24 ± 0.35 Ma. Steps 1-3 yielded varying ages of ~400 Ma, 77 Ma, and 116 Ma, respectively. Steps 4-12 yielded an age gradient varying from ~58 Ma to ~81 Ma. Steps 12-28 and 32-34 yielded an apparent flat age spectrum from ~71 Ma to 73 Ma (Figure 16a). The relatively flat apparent age spectrum from sample BM16 suggests the NE granodiorite pluton underwent rapid cooling. Sample BM18 was collected from the Cretaceous granite (Kg) located within the mylonitic shear zone on the SW portion of the transect. BM18 yielded an $^{40}Ar/^{39}Ar$ age spectrum with a total gas age of 73.43±0.33 Ma. Steps 1-3 yielded varying ages of ~33 Ma, 176 Ma, and 110 Ma, respectively. Steps 4-33 yielded apparent ages varying from ~63 Ma to 87 Ma, with an overall increase in age with respect to increasing heating steps (Figure 16b). These samples show signs of variable excess argon during step heating. It is noted that the first step of the isothermal duplicates is older than the second, which is common in the lower temperature portion of the K-feldspar gas release effected by excess argon. Nonetheless, with the aid of isothermal duplicates, meaningful cooling histories can be extracted through MDD modeling, discussed below.

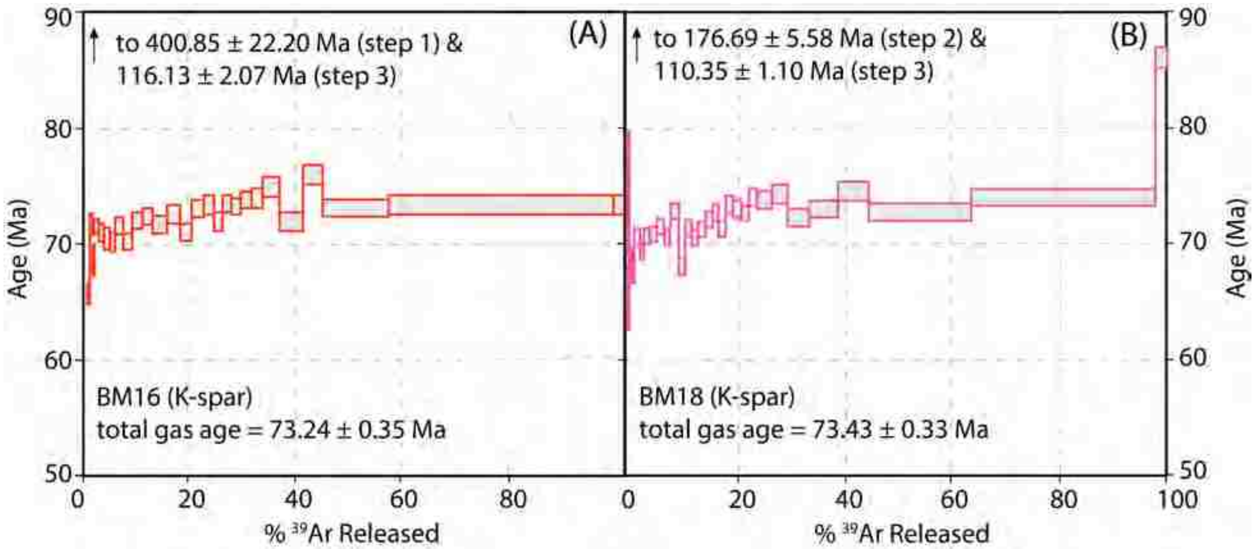

[redacted]

<u>K-feldspar MDD Modeling</u>

Multiple domain diffusion (MDD) modeling, following the approach of Lovera (1992), was performed on K-feldspar samples to constrain a continuous T-t thermal history for plutons from ~300-150˚C. Software *SizeExtractor* (Zeitler, 1993) was used to model the diffusion parameters and domain distributions, as well as domain sizes and volumes. Inversion modeling was performed with *Arvert* (Zeitler, 1993) to determine the age spectrum fit of the sample vs. model, as well as T-t cooling histories. *Arvert* uses the Controlled Random Search (CRS) method to determine convergence of cooling curves and thermal history recorded by K-feldspar. Data was best fit by using 6 to 7 domains and activation energies (Ea) of ~37 and 38 kcal/mol.

Sample BM16 was best modeled using 6 domains. Diffusion parameters were obtained by fitting a linear regression to the initial low-T steps on the Arrhenius plot. Steps 2-6, plus their isothermal duplicates, were regressed to obtain an Ea of 38.85 kcal/mol and D/r^2 value of 5.84. Arrhenius and domain distribution plots show a high correlation between modeled data and sample data (Figure 17a-b). Low temperature steps with excess Ar were excluded from the inversion modeling, and only steps showing a systematic age increase were used to constrain cooling histories. Excess Ar in low temperature steps is demonstrated by employing isothermal duplicates during the lab heating schedules. Duplicates that show a decrease in age with respect to the initial duplicate suggests the presence of excess Ar. 5000 CRS iterations were used to pool the cooling curves obtained in the inversion modeling, and lower and upper closure temperatures on the cooling curves were constrained from diffusion domain calculations. Modeling demonstrates sample BM16 underwent rapid cooling from 73.1 Ma to 67.2 Ma, and temperatures of ~294˚C and 163˚C, providing a cooling rate of ~22.2˚C/m.y. (Figure 17c-d).

Sample BM18 was best modeled using 7 domains. Diffusion parameters were obtained by fitting a linear regression line to the initial low-T steps on the Arrhenius plot. Steps 1-4, plus their isothermal duplicates, were used to obtain an Ea of 37.77 kcal/mol and D/r^2 value of 6.807 (Figure 18a-b). Initial low-T steps with excess Ar were excluded from the model, to obtain the best fit between model results and sample data. Only steps with a systematic increase in age were used to determine cooling histories. Initial low-T heating steps showed a slight divergence between modeled age spectrum and sample age spectrum. Model and sample data converge and show a high correlation once the sample released ~10% ^{39}Ar. Steps below 10% ^{39}Ar release demonstrate a lower correlation fit between modeled data and sample data, likely due to the presence of excess Ar in the sample. Model run "h20" showed the highest correlation between model results and sample data, and is interpreted to demonstrate reliable cooling histories for sample BM18. 5000 CRS iterations were used to pool cooling histories. Upper and lower closure temperatures were obtained during diffusion domain calculation. Modeling demonstrates sample BM18 cooled at a rate of 18.6 ˚C/m.y., from 72.1 Ma to 65.1 Ma and temperatures of 271˚C and 141˚C (Figure 18c-d).

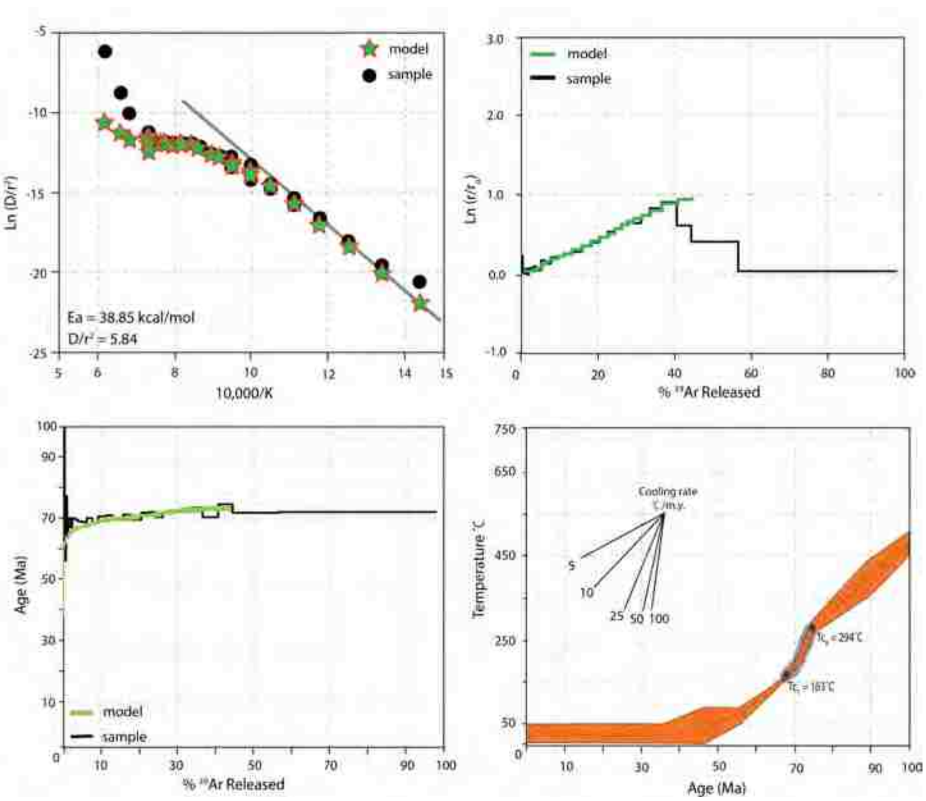

[redacted]

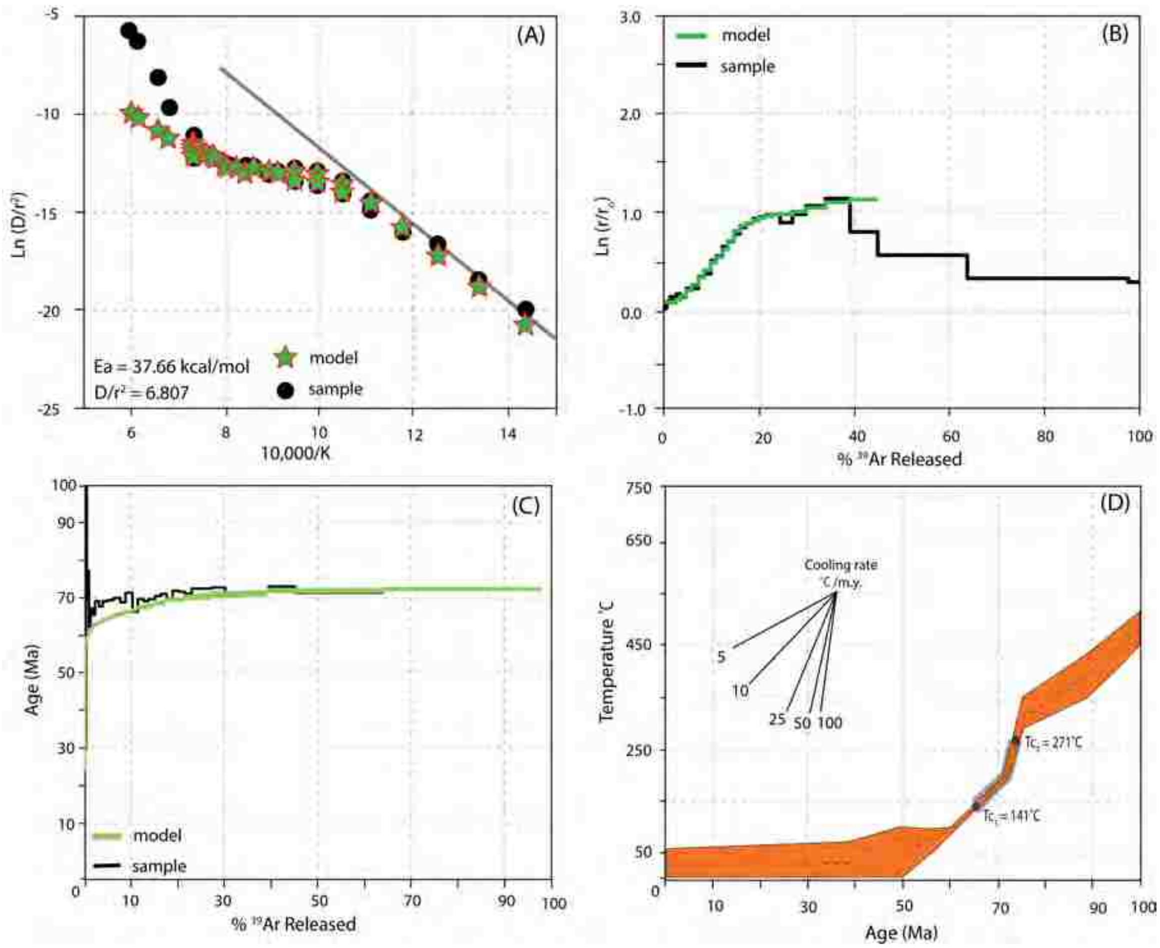

[redacted]

4.4.2 Granite Mountains

<u>Biotite and Hornblende</u>

Two biotite (B) samples and one hornblende (H) sample were analyzed from the Granite Mountains transect and are reported below. Biotite was separated from the Kgd and Kpm plutonic phases, hornblende-bearing rocks were only found in the Kgd pluton on the NW portion of the transect. Sample locations are shown in Figure 3.

Biotite sample GM7 is a Cretaceous porphyritic monzonite in the SE portion of the Granite Mountains. This sample produced a discordant age spectrum with a total gas age of 72.08±0.07 Ma. Incipient chloritization of biotite may explain the discordant age spectrum and unreliable age (Figure 19a). Biotite sample GM6 is from the Cretaceous granodiorite pluton from the NW portion of the sampling transect. This sample yielded a discordant age spectra with a total gas age of 60.20±0.23 Ma. It is interpreted that the discordant age spectra and unreliable age is a result of chloritic alteration of biotite (Figure 19b). Hornblende was also analyzed from sample GM6 (H). The total gas age for this sample is 79.18±0.11 Ma. Steps 1-7 yielded anomalously old ages resulting from excess argon, followed by an argon loss, producing the younger ages. Steps 8-13 define the flattest portion of the age spectrum and are determined to be meaningful steps yielding ~82% ^{39}Ar release and a preferred age of 78.66± 0.26 Ma (Figure 19c).

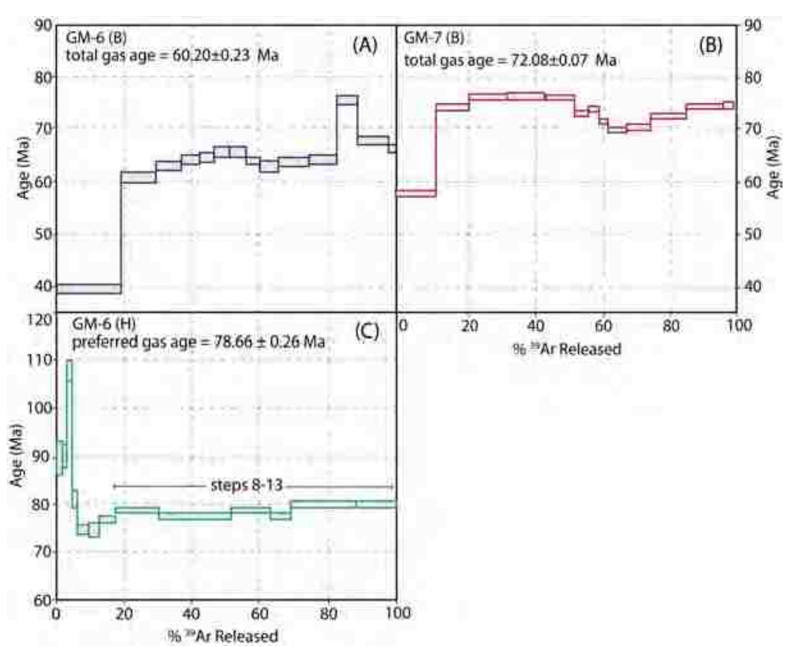

[redacted]

K-feldspar

Two new K-feldspar separates were analyzed from the NW-SE transect across the Granite Mountains to constrain the lower temperature thermal profile for Cretaceous plutons; these samples were combined with the central most sample from Kula (2002). GM7 was collected from the SE portion of the range, furthest from the BCF and mylonitic zone, whereas GM6 was collected from the NW portion of the range, closest to the BCF and mylonitic shear zone (Figure 3).

Sample GM7, collected from a Cretaceous porphyritic monzonite (Kpm), yielded an $^{40}Ar/^{39}Ar$ apparent age spectrum with a total gas age of 73.31 ± 0.40 Ma (Figure 20a). Steps 1-4 yielded ages varying from ~261 Ma, 98 Ma, 158 Ma, and 87 Ma, respectively. Varying ages produced from steps 1-4 are attributed to the release of excess argon from fluid inclusions during initial lower temperature heating steps. Following the initial steps that showed degrees of excess argon, steps 5-34 produced ages ranging from ~68 Ma to 74 Ma, defining a very gentle age gradient for the sample. Sample GM6 was collected from a Cretaceous granodiorite pluton in the NW portion of the range. GM6 produced an $^{40}Ar/^{39}Ar$ apparent age spectrum with a total gas age of 69.72 ± 0.23 Ma (Figure 20b). Steps 1-5 yielded varying ages of ~72 Ma, 94 Ma, 81 Ma, 50 Ma, and 77 Ma, respectively. Steps 6-34 produced apparent ages ranging from ~54 Ma to 72 Ma, defining an age gradient.

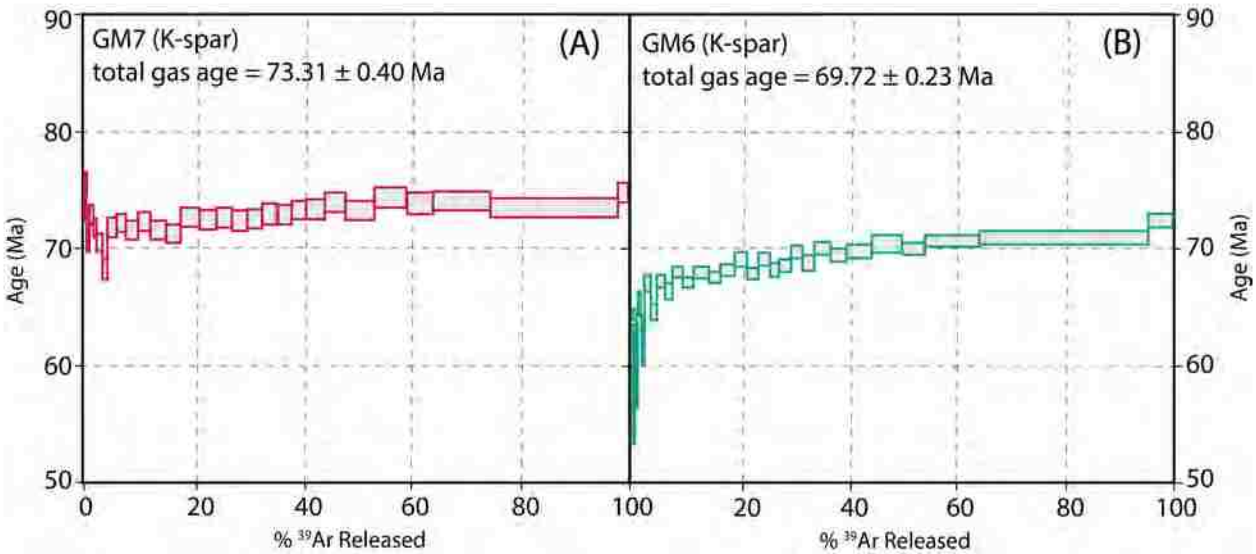

[redacted]

K-feldspar MDD Modeling

Multiple domain diffusion (MDD) modeling was performed on K-feldspar separates from Granite Mountains to constrain a continuous T-t thermal history for plutons from ~300-150˚C, and to build off the dataset of Kula (2002). Modeling followed the routine and approach of Lovera (1992) and Zeitler (1993), as described above. Data was best fit by using 5 to 9 domains and activation energies (Ea) of ~38 kcal/mol.

Sample GM7 was modeled using 9 domains. Diffusion parameters where obtained by fitting a linear regression line to the initial low-T steps on the Arrhenius plot. Steps 2 – 6 where regressed giving an Ea of 38.98 kcal/mol and D/r^2 value of 2.404. Domain structure and Arrhenius plots show a well constrained fit between modeled data and sample data (Figure 21a-b). Furthermore, an infinite slab geometry was used to the model diffusion domains. Low temperature initial steps with excess Argon were excluded from the model. Maximum Monte-Carlo and CRS cooling rates of 60 and 80˚C/m.y. were used to best fit model results with sample age spectrum results. The continuous cooling curves obtained from 5000 CRS iterations provide a tight convergence. Furthermore, upper and lower closure temperatures on the cooling curves were calculated when diffusion domains were calculated. Modeling demonstrates that sample GM7 (Kpm) was rapidly cooled from 74.09 Ma to 71.26 Ma and temperatures of ~304 and 147˚C, providing a cooling rate of 53.28˚C/m.y. (Figure 21c-d). Additionally, steps with significantly older ages were excluded. Heating steps with a systematic increase in age were selected to use in the model, which provided the modeled age spectrum results.

Sample GM6 was modeled using 8 domains with an activation energy of 38.98 kcal/mol. Maximum Monte-Carlo and CRS cooling rates of 20 and 40˚C/m.y. were used to best fit model results with sample age spectrum results. Low-T initial heating steps that demonstrated excess Ar and significantly old ages were excluded from the model (Figure 22a-b). Steps that displayed a systematic increase in age, defining a continuous upward stepping age spectrum were used to obtain model results. 5000 CRS iterations were pooled to obtain continuous cooling curves. Results demonstrate that the sample rapidly cooled from 73.43 Ma to 67.47 Ma from temperatures of 307 to 154˚C, providing a cooling rate of 25.93 ˚C/m.y. (Figure 22c-d).

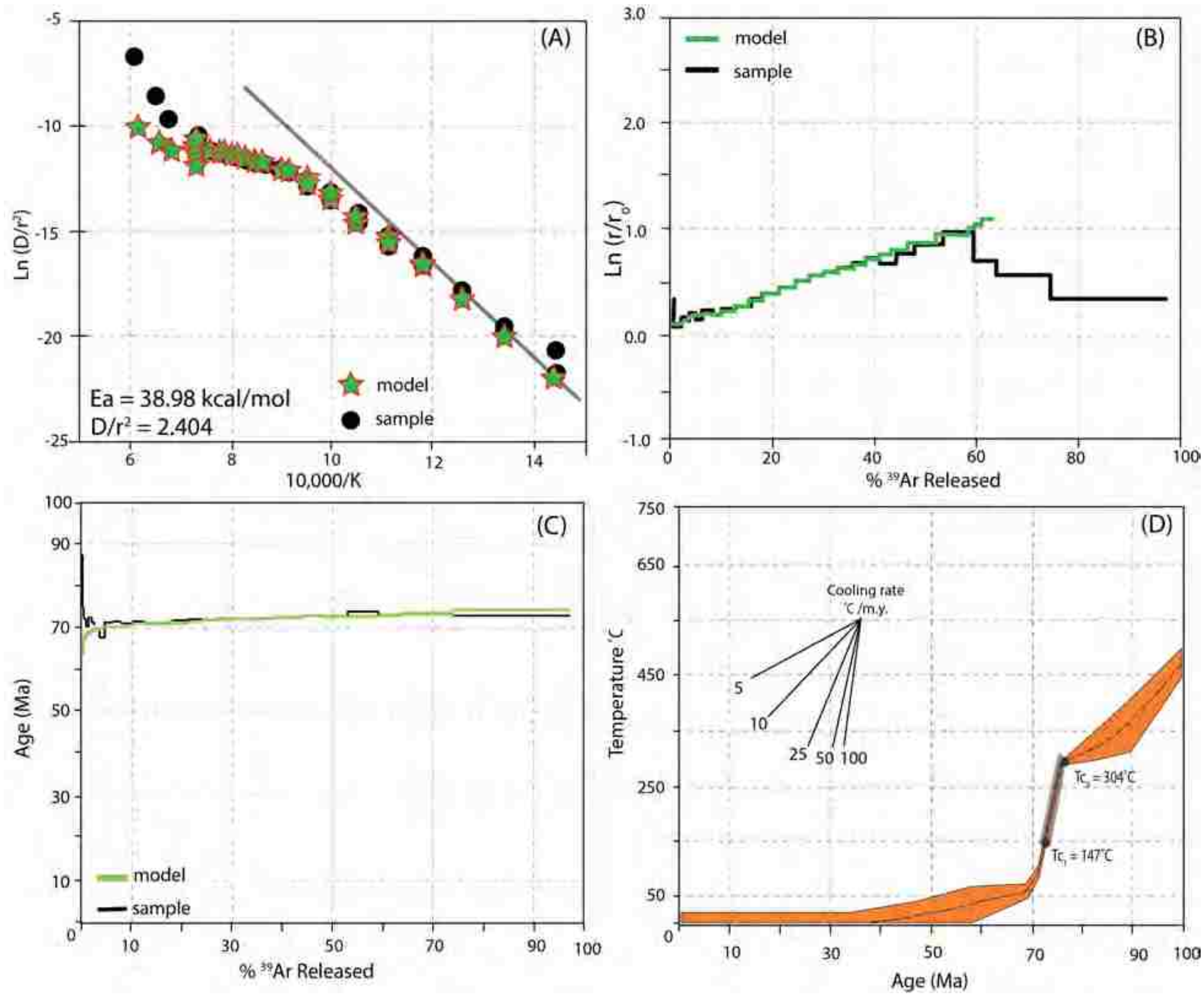
(A)
Ln (D/r²)
10,000/K
Ea = 38.98 kcal/mol
D/r² = 2.404
model
sample
(B)
Ln (r/r₀)
% ³⁹Ar Released
model
sample
(C)
Age (Ma)
% ³⁹Ar Released
model
sample
(D)
Temperature °C
Age (Ma)
Cooling rate
°C /m.y.
5
10
25
50
100
Tc₂ = 304°C
Tc₁ = 147°C

[redacted]

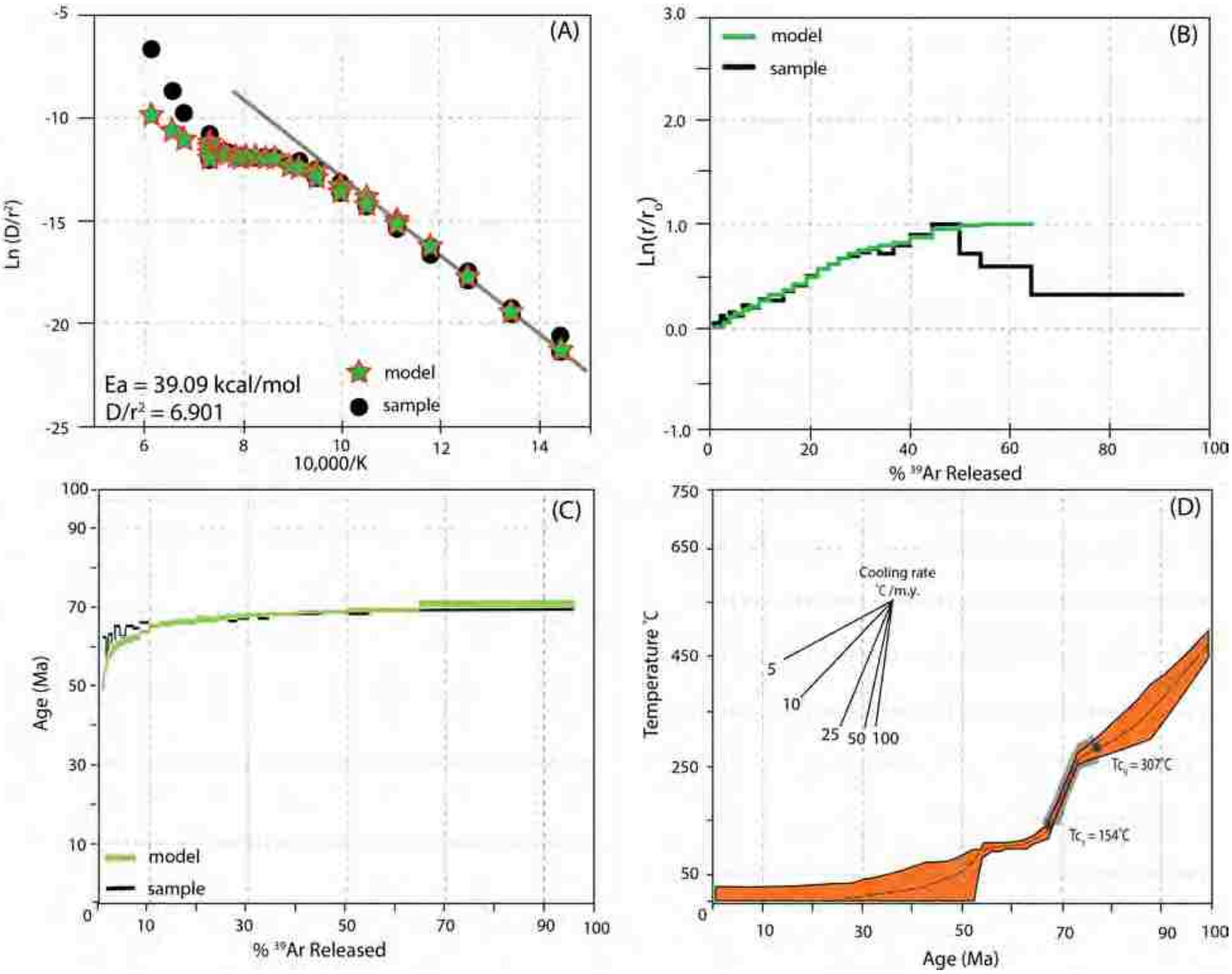

[redacted]

4.5 Reconstructed T-t profiles

U/Pb zircon geochronology, $^{40}Ar/^{39}Ar$ thermochronology, and Multiple Domain Diffusion modeling of K-feldspar provide insight into the temperature-time thermal histories of plutonic rocks from crystallization at ~750 ˚C through K-feldspar small domain closure temperatures of ~150

˚C. Furthermore, cooling rates can be inferred between T-t points and through continuous cooling curves of modeled K-feldspar. Thus, T-t cooling curves can be reconstructed.

For the Granite Mountains, this study adds two new reconstructed T-t profiles (GM6 and GM7), which, combined with the central most sample from Kula (2002) provides a NW-SE transect. Sample GM7 from the SE portion of the Granite Mountains yielded a U/Pb zircon crystallization age of 74.19 ± 0.93 Ma. GM7 yielded a discordant biotite age spectrum and we don't use it in cooling history construction. MDD modeling of K-feldspar indicates GM7 continued to cool rapidly from 74.09 Ma to 71.26 Ma, from ~304 ˚C to 147 ˚C. Modeled MDD cooling curves indicate a cooling rate of 53 ˚C/m.y. Additionally, the cooling rate from emplacement temperatures through lower K-feldspar MDD closure temperatures is ~204 ˚C/m.y. (Figure 23a). The U/Pb crystallization age and upper MDD K-feldspar age are all concordant for the sample, suggesting almost instantaneous cooling from ~750 ˚C to ~300 ˚C. This is likely due to very rapid denudation of the pluton during extension or emplacement at very shallow crustal levels followed by rapid thermal equilibration with the surrounding country rock, and is interpreted herein to be an artifact of both. Given the younger age and position within the Granite Mountains, and the fact that this 74 Ma pluton crystallized while the older Late Cretaceous plutons were undergoing rapid cooling, this pluton was likely emplaced during extension and rapid exhumation into shallow crustal levels followed by continued cooling and exhumation.

Sample GM6 is from the NW Granite Mountains and is closest to the mylonitic shear zone and the BCF. GM6 yielded a zircon crystallization age of 80.43 ± 0.97 Ma and a hornblende preferred age of 78.66 ± 0.26 Ma, indicating the pluton cooled at a rate of ~141˚C/m.y. from emplacement through ~500 ˚C. The biotite analysis yielded a highly-disrupted age spectra, with most steps yielding ages not consistent with the hornblende and K-feldspar analyses, and is not considered in the T-t reconstruction. Sample GM6 cooled from 78.66 Ma to 73.43 Ma at a rate of

~37 ˚C/m.y. K-feldspar MDD modeling indicates the pluton continued to cool from 307 ˚C at 73.4 to 154 ˚C at 67.5 Ma, at a rate of ~26 ˚C/m.y. (Figure 23b).

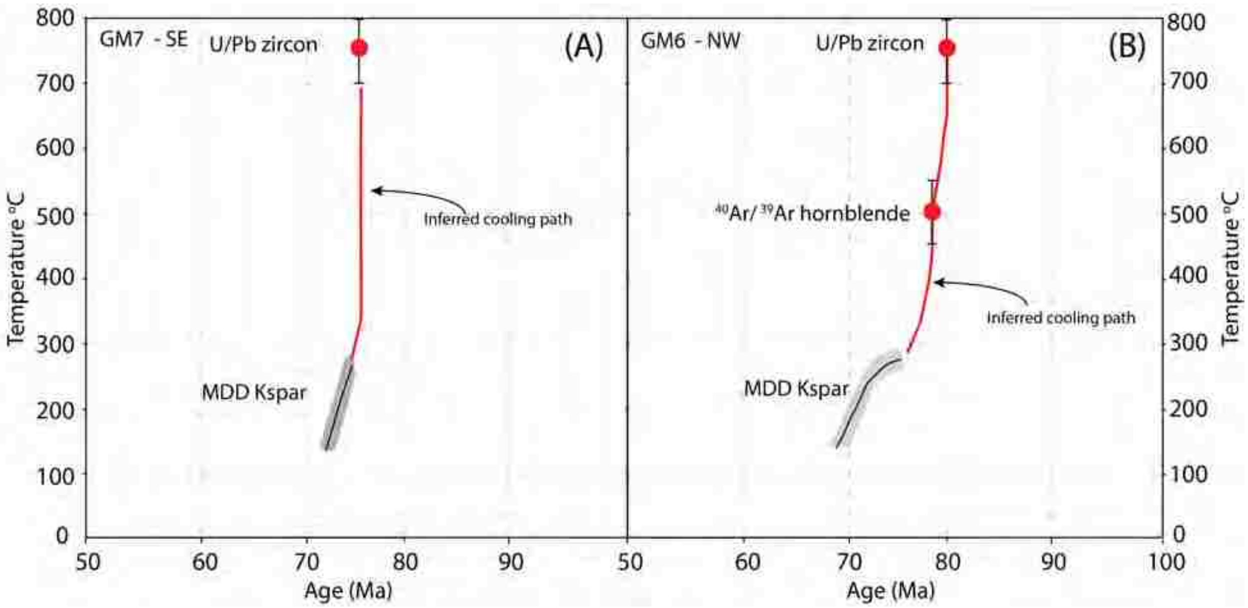

[redacted]

For the Bristol Mountains, this study adds two reconstructed T-t profiles on a SW – NE transect. Sample BM16 is from a large granodiorite pluton (Kgd) in the NE portion of the range, furthest from the mylonitic shear zone. The crystallization age for Kgd is determined from the U/Pb zircon age of 75.68 ± 0.65 Ma for sample BM9, approximately 3 km to the SW of BM16. Sample BM16 yielded a pseudo-plateau biotite age of 73.65±0.35 Ma, suggesting the pluton cooled at a rate of ~184 ˚C/m.y. from ~750 ˚C to 350 ˚C. MDD modeling of K-feldspar demonstrates continued fast cooling from 294 ˚C through 163 ˚C and 73.1 Ma to 67.2 Ma, indicating a cooling rate of 22.2 ˚C/m.y. (Figure 24a).

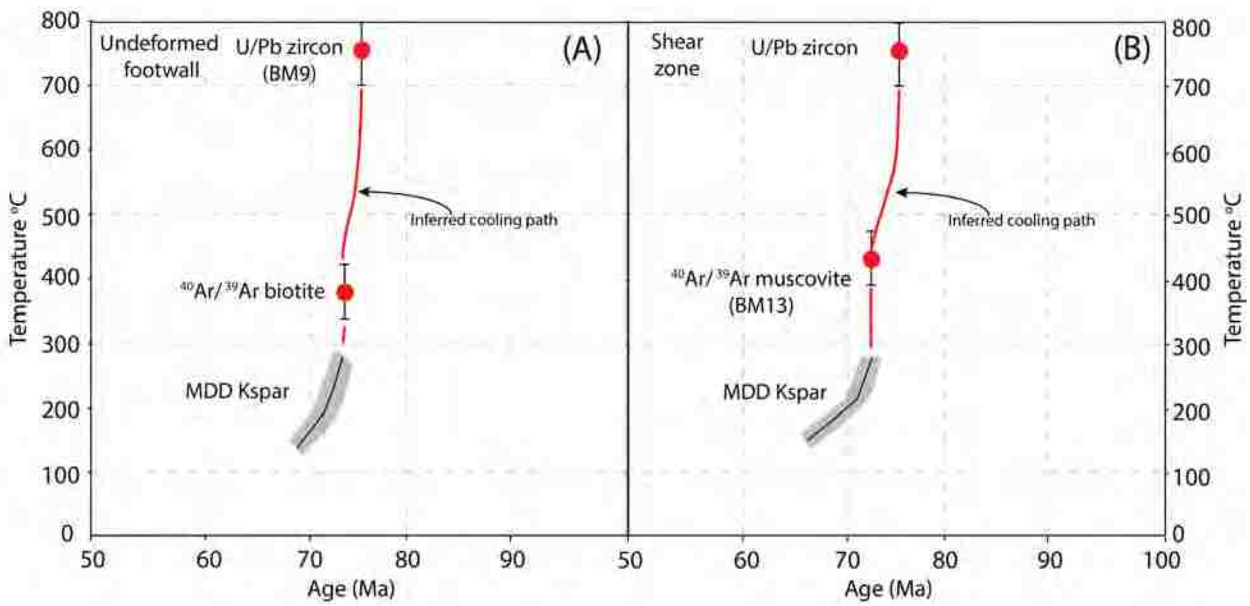

[redacted]

Sample BM18, is collected from the shear zone within the Kg in the SW portion of the range. Sample BM18 yielded a zircon crystallization age of 75.55 ± 1.2 Ma. A muscovite rich border phase of Kg ~100 m NNW of sample BM18 yielded a $^{40}Ar/^{39}Ar$ plateau age of 72.57 ± 0.80 Ma (BM13), indicating that the pluton cooled at a rate of ~ 117.5 ˚C/m.y. MDD modeling of K-feldspar from sample BM18 indicates continued, slower cooling from 72.1 Ma to 65.1 Ma and 271 ˚C through 141 ˚C, at a rate of 18.6 ˚C/m.y. (Figure 24b).

4.5.1 Previous Results – Granite Mountains

Kula (2002) performed U/Pb geochronology, $^{40}Ar/^{39}Ar$ and U-Th/He thermochronology, as well as Al-in-hornblende geobarometry on a SW-NE sampling transect of Cretaceous plutonic rocks across the Granite Mountains, and on a single sample from a Jurassic pluton in the Providence Mountains to the NE. The goal of the study was to constrain thermal profiles, as well as emplacement depths for Jurassic and Cretaceous plutons across the transect, to address whether the Granite Mountains represented a tilted crustal block. Al-in-hornblende geobarometry performed by Kula (2002) indicate that Late Cretaceous plutons across the range were emplaced at similar depths, with pressures from ~4.0 to 4.89 kbar, suggesting deep burial of the entire range and not showing evidence for significant tilting. These pressures correspond to depths ranging from 14.5 to 17 km in the Late Cretaceous (see Table 1 from Kula, 2002).

Here, we summarize the reconstructed temperature-time (T-t) profiles and geobarometry results from Kula (2002), integrating the new U/Pb zircon age constraints. The SW monzogranite sample (GM317) was reanalyzed for zircon U/Pb crystallization age and yielded an age of 75.55±0.81 Ma. U/Pb zircon (this study) and $^{40}Ar/^{39}Ar$ hornblende (74.80±0.42 Ma; Kula, 2002) yield indistinguishable ages, demonstrating rapid cooling from zircon crystallization through the hornblende closure temperature of ~500˚C. Following hornblende closure, sample GM317 experienced slower but still rapid cooling from ~75 Ma (500˚C) to 71 Ma (300˚C), yielding a cooling rate of ~49˚C/m.y. K-feldspar MDD modeling indicates that from 71 to 69.1 Ma the pluton cooled at a rate of ~63˚C/m.y. After rapid cooling in the Late Cretaceous, the pluton underwent very slow cooling until the Miocene, as indicated by a (U-Th)/He apatite age of ~23.6 Ma (Figure 25).

Reanalysis of the central granodiorite sample (GM313) from Kula (2002) yields a U/Pb zircon crystallization age of 77.18±0.86 Ma, which combined with the prior hornblende plateau age of 76.46±0.53 Ma (Kula, 2002) indicates this pluton cooled rapidly following crystallization. Between ~76.5 Ma and 71.6 Ma the pluton cooled at a rate of ~60˚C/m.y. through ~293˚C. K-feldspar MDD data demonstrate further cooling from ~293-157˚C, from 71.6 to 67.3 Ma at a rate of ~32˚C/m.y. The pluton experienced a period of slow cooling from 67 to 40 Ma, as demonstrated by a U-Th/He apatite age of ~40.2 Ma (Figure 25).

The NE quartz monzonite sample (GM515) from Kula (2002) was reanalyzed for zircon U/Pb age, yielding an age of 78.61±0.9 Ma. Zircon analysis from this study and the hornblende age determined from Kula (2002) of 76.57±0.9 Ma, indicates this pluton experience geologically rapid cooling after intrusion. Very rapid cooling from 500 ˚C through ~251 ˚C occurred after initial cooling, at a rate of 67˚C/m.y. (Kula, 2002). K-feldspar data indicate a cooling interval ~251 to 145˚C occurred from 72.9 to 66.3 Ma, constraining a lower cooling rate of ~16˚C/m.y. (Kula, 2002). An apatite age of ~21.2 Ma demonstrates this pluton underwent slow cooling from ~66 to 22 Ma, at a rate 1.7˚C/m.y. (Kula, 2002) (Figure 25).

An additional K-feldspar, not reported in Kula (2002), was analyzed by Kula in the Granite Mountains (Kula, personal communication), from a Jurassic leucogranite pluton (GM138) in the NW portion of the mountains. Sample GM138 is in a horse block within the BCF. This pluton yielded an age spectrum and K-feldspar MDD cooling history distinct from the surrounding Cretaceous plutons, motivating the analysis of zircon crystallization age reported in this study. Zircon U/Pb crystallization age and $^{40}Ar/^{39}Ar$ K-feldspar indicate this pluton underwent slow cooling from ~160 to ~79 Ma at a rate of 4.9˚C/m.y. Additionally, K-feldspar MDD modeling indicates a cooling rate of 4.3˚C/Ma from ~79 to ~40 Ma (Figure 25).

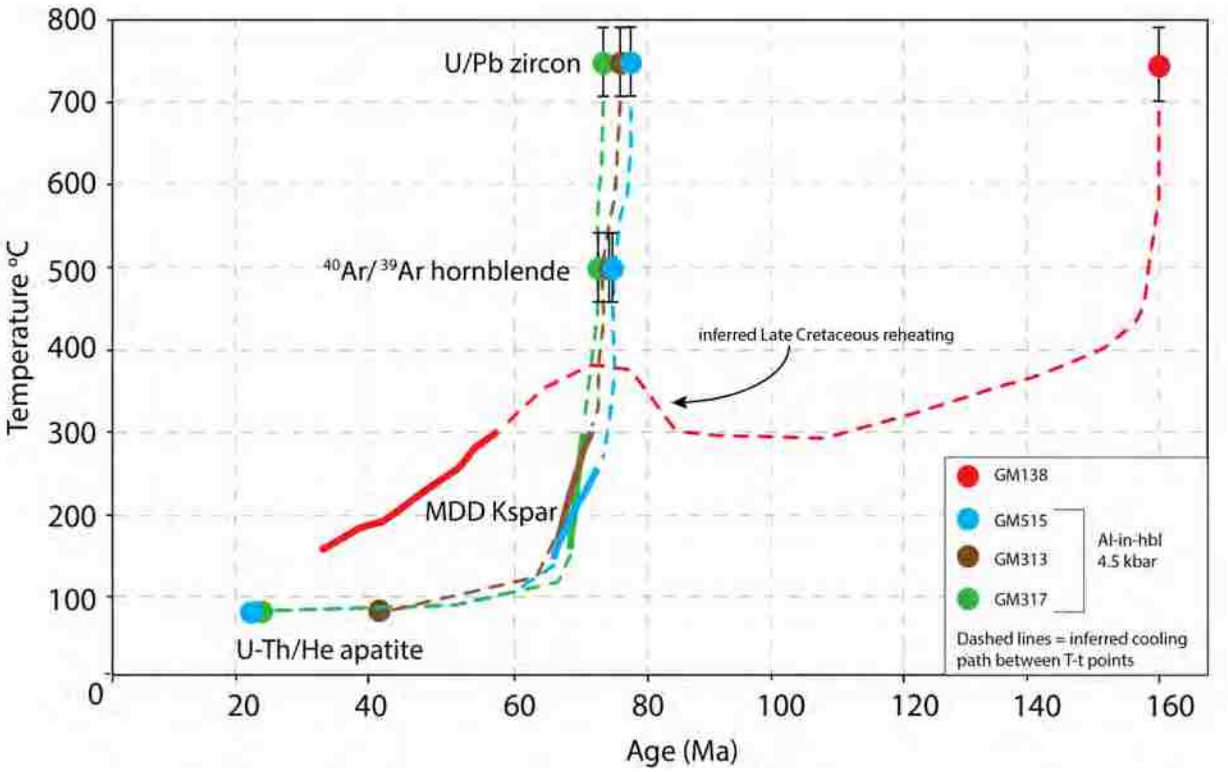

[redacted]

5. SUMMARY AND DISCUSSION

5.1 Mechanisms of Cooling in the Eastern Mojave Desert

The cause of Late Cretaceous synconvergent cooling within the southern Cordillera has been a subject of controversy (Dumitru et al., 1991; Hodges and Walker, 1992; George and Dokka, 1994; Miller et al., 1995; Grove et al., 2003; Saleeby et al., 2003; Wells et al., 2005; Wells and Hoisch, 2008; Wells et al., 2012). Rapid Late Cretaceous cooling of mid-crustal peraluminous granitic melts in the eastern Mojave, as shown by isotopic studies, have been interpreted to be a product of extensional exhumation (Foster et al., 1990; Foster et al., 1992; Kula, 2002; Wells et al., 2002;

Wells et al., 2005). Cooling signatures in the southern Cordillera have also been attributed to a refrigeration effect, which is a manifestation of the Farallon plate flattening beneath North America and replacing hot asthenosphere with a cold oceanic slab (Dumitru et al., 1992; Jacobson et al., 1996; Saleeby, 2003). In contrast, cooling of Cretaceous plutons in the Peninsular Range of southern California has been attributed to erosional exhumation (George and Dokka, 1994; Grove et al., 2003a). Erosion-induced cooling is also predicted over the Kingman arch, east of the Bristol and Granite mountains, a paleo-structural high in the California-Nevada-Arizona border region during the latest Cretaceous to earliest Paleocene (Beard and Faulds, 2010; Young and Hartman, 2014). Uplift was manifest by erosional stripping of Paleozoic and Mesozoic rocks, suggesting that erosional exhumation was likely a major event post-70 Ma. The timing and geographic extent of the Kingman arch is poorly understood, and may be a result of Laramide-style end-loading of the North American plate, basal traction, dynamic uplift following passage of the subducted oceanic plateau (Liu et al., 2010), or isostatic uplift due to delamination (Wells and Hoisch, 2008).

Other mechanisms explaining Late Cretaceous cooling and exhumation are deliberated herein. For example, erosional exhumation is considered to have aided in exhumation of mid-crustal rocks in the latest Cretaceous to early Paleocene. Evidence for the structurally high Kingman arch in the latest Cretaceous to early Paleocene and subsequent stripping of Paleozoic and Mesozoic rocks suggests erosion of the southern Cordillera was significant at the time following the wake of the subducted oceanic plateau. Additionally, lithospheric refrigeration of the eastern Mojave region, during the Late Cretaceous, is considered trifling. Lithospheric refrigeration may have local effects and may contribute to the slowing of cooling rates once the leading edge of flat-slab subduction passed the east Mojave Block sector, but is not considered to be causative mechanism for the observed rapid cooling. These mechanisms do not alone explain the rapid and region Late Cretaceous cooling of mid-crustal rocks. The observed rapid cooling therefore requires extensional exhumation, and is postulated to be the major contributor to exhumation and cooling during the Late Cretaceous, which was trailed by continued exhumation via erosional stripping during the latest Cretaceous to early Paleocene. The southern Cordillera experienced tectonic quiescence until the Neogene, when Basin and Range and Eastern California Shear Zone tectonics began to evolve.

5.2 Age of Extensional Deformation in the Granite Mountains

The age of mylonitic deformation is best constrained by combining footwall cooling histories with deformation temperatures recorded in the shear zone. Mylonitically deformed granitoid rocks in the Granite Mountains form a discontinuous belt in the footwall of the Bull Canyon Fault. Mylonitic fabrics are dominately preserved in Jurassic leucocratic plutons and sills within dioritic plutons. Structural measurements demonstrate an overall geometry and transport direction of 231˚/28˚NW and 324˚/31˚, respectively. Shear-sense indicators, at the thin-section scale, consistently show a top-to-the-NW non-coaxial down-dip sense of shear. Geometry, transport direction, and kinematic indicators suggest that the mylonitic shear zone demonstrates a normal sense of motion. Microstructures from mylonitic rocks in the Granite Mountains record high temperatures of deformation (~400 - 600˚C). Incipient gneissic banding is present across the shear zone, displaying distinct bands of dynamically recrystallized quartz and feldspar. SGR of feldspar is pervasive throughout the Granite Mountains shear zone suggesting that deformation occurred at lower amphibolite facies conditions.

New and refined U/Pb geochronology and $^{40}Ar/^{39}Ar$ thermochronology from the Granite Mountains indicate that mid-crustal Cretaceous plutons were rapidly cooled after emplacement, whereas Jurassic rocks experienced slow cooling post emplacement through the Cretaceous. Kula (2002) reports, from K-feldspar MDD modeling, that the studied plutons cooled through K-feldspar closure temperatures by ~66 Ma at rates of ~63˚C/m.y., 32˚C/m.y., and 16˚C/m.y., and suggested that fast cooling rates advocate tectonic exhumation as opposed to erosional exhumation. New samples added from this study, GM6 and GM7, which define a transect across the Granite Mountains from SE to NW, yield crystallization ages of ~80 Ma and 74 Ma, respectively. K-feldspar MDD modeling indicates sample GM7 underwent rapid cooling through ~150˚C, at a rate of ~53 ˚C/m.y. Furthermore, K-feldspar MDD modeling indicates GM6 experienced rapid cooling, at a rate of ~23˚C/m.y. Data from Kula (2002), combined with new data presented here, provides unequivocal documentation of the age of emplacement and T-t thermal histories for footwall rocks in the Granite Mountains.

New U/Pb zircon data from Jurassic plutons demonstrate crystallization ages of ~157 Ma (GM5) and 160 Ma (GM138). Unpublished K-feldspar data from Kula suggests that Jurassic leucogranite pluton (GM138) experienced very slow cooling through K-feldspar closure temperatures at a rate of ~4.3˚C/m.y. Figure 26 shows shallow age gradients for K-feldspar age spectra for undeformed footwall rocks and a steep age gradient for a K-feldspar age spectrum for GM138, which sits in a horse block within the BCF (upper plate?). The steep age spectrum is

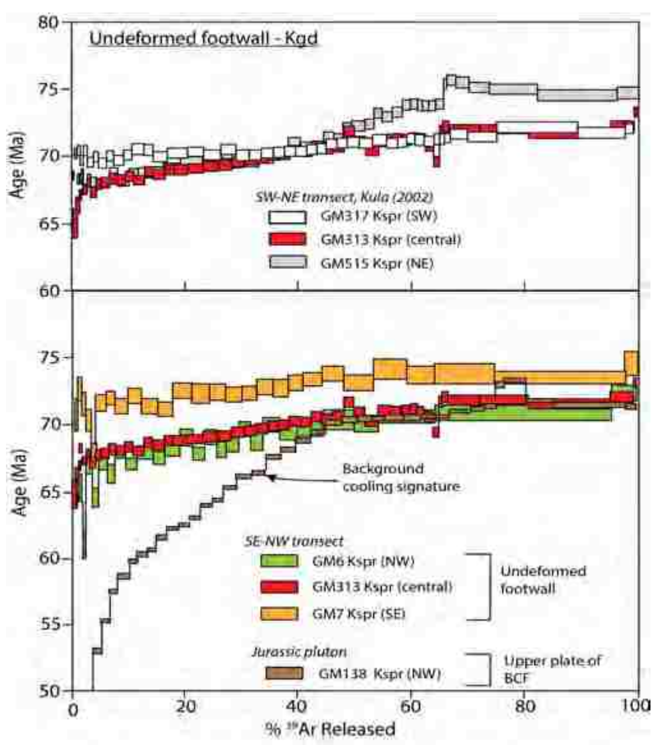

[redacted]

interpreted to record the background cooling signature not associated with rapid extensional exhumation. The Jurassic pluton was likely reheated during Cretaceous magmatism, resetting all diffusion domains in the K-feldspar. The departure from Cretaceous plutons at ca. 69 Ma may indicate movement into the hanging-wall ambient cooling regime.

Reconstructed T-t thermal profiles for GM6, GM313, and GM7, combined with deformation temperatures from microstructures bracket the age of top-NW mylonitic deformation. The maximum age of mylonitic deformation is inferred from the 80 Ma emplacement age of GM6, closest to the mapped trace of the shear zone, assuming Late Cretaceous plutons are emplaced synextensional, and is bracketed from 80 to 67 Ma (Figure 27). The minimum age range of deformation is bracketed between 78 to 75 Ma, and is constrained by microstructural deformation temperatures and the T-t path. Erosion is considered a likely contributor to exhumation post-71 Ma and slower MDD cooling rates (GM6) may record more erosional exhumation than extensional.

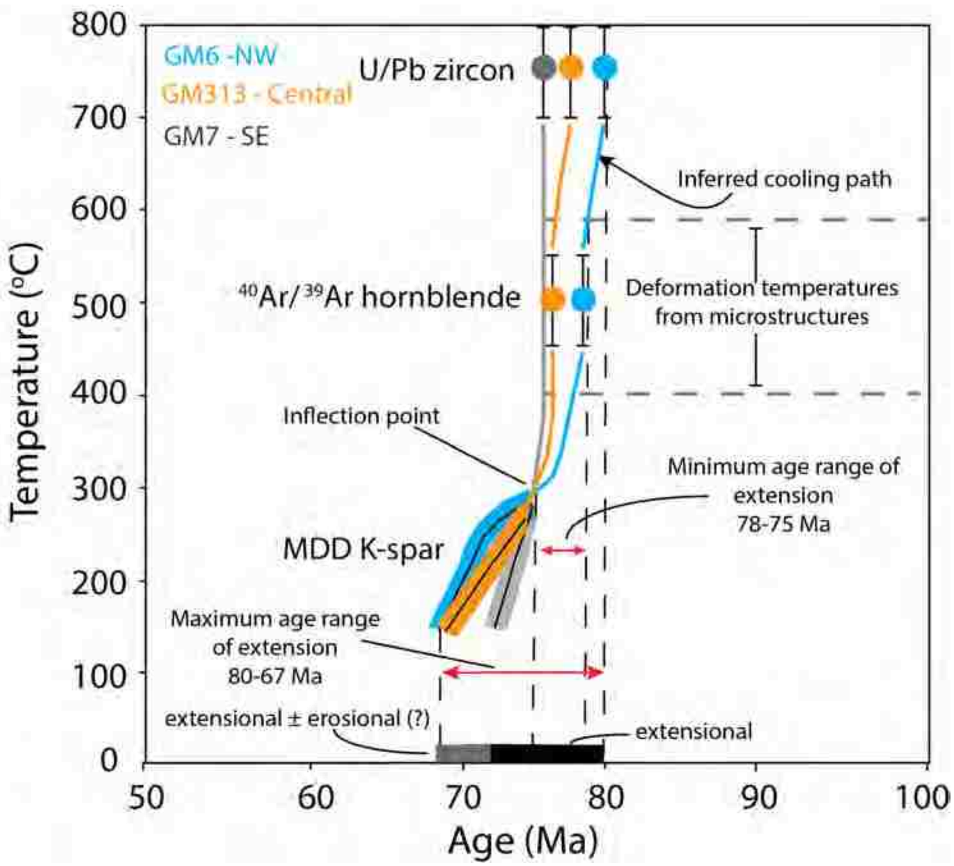

[redacted]

5.2.1 Miocene Inheritance of Late Cretaceous Fabric in the Granite Mountains

Many structures that may have been responsible for Late Cretaceous exhumation have been overprinted by Cenozoic extension, making documentation of Late Cretcaeous extension challenging. Distinguishing Late Cretaceous extension from Cenozoic extension requires looking through the extensive overprint and reactivation by Cenozoic normal faulting, such as the Bull Canyon Fault. To address this issue, we present compelling data documenting the emplacement and thermal histories of plutonic rocks from the Granite Mountains, mylonitic shear zone kinematics and geometries as well as microstructural deformation mechanisms to elucidate the age of mylonitic deformation, and geometry and kinematics of the Bull Canyon fault. These data provide unequivocal evidence linking Late Cretaceous cooling signatures of Cretaceous mid-crustal granitoid rocks to Late Cretaceous extension and exhumation, and for later overprinting and reactivatation by Miocene detachment faulting along the Bull Canyon fault.

The (BCF) is a low-angle normal fault, present along the northern margin of the Granite Mountains, demonstrating brittle deformation (Howard et al., 1987). The age of the BCF is poorly constrained from Tertiary gravel and breccia deposits that are cut by the BCF. The BCF has an arcuate geometry with the average fault surface striking 252˚ and dipping 41˚NW; mechanical striations indicate an average hanging-wall transport direction of 324˚ and a plunge of 39˚. The arcuate shape of the BCF follows the average geometry of mylonitic foliation. Furthermore, mechanical striations associated with the BCF are within statistical error of stretching lineations associated with mylonitic deformation. The similar geometries and transport directions between the BCF and mylonitic rocks suggests that the BCF likely inherited the architecture of the older mylonitic shear zone, experiencing geometric and kinematic reactivation (e.g., Holdsworth et al., 1997). Furthermore, the BCF largely excised and/or displaced most evidence of the shear zone from the Granite Mountains.

5.3 Age of Bristol Mountain Shear Zone

The age of mylonitic deformation in the Bristol Mountains, similar to the Granite Mountains mylonites, is best constrained by combining footwall and shear zone cooling histories with deformation temperatures recorded in mylonitically deformed rocks. Shear zone geometry and kinematics within the Bristol Mountains demonstrate a top-to-the-SW non-coaxial down-dip sense of shear, indicating extensional deformation. Microstructural studies consistently show mid-to-upper greenschist and lower amphibolite facies deformation conditions. Furthermore, deformation lamellae are pervasive across the shear zone, and may suggest a progressive decrease in deformation temperature during denudation of the shear zone. The presence of higher temperature microstructures (feldspar SGR and quartz GBM), as well as lower temperature deformation lamellae indicates that mylonitic rocks were deformed during decreasing temperature conditions over the range of ~550-350 ˚C.

New U/Pb zircon crystallization ages and $^{40}Ar/^{39}Ar$ thermochronology from the Bristol Mountains indicate Cretaceous plutons experienced rapid cooling after emplacement. U/Pb zircon data indicate Cretaceous plutons were emplaced at ~750˚C by 75 Ma. Additionally, $^{40}Ar/^{39}Ar$ thermochronology data from biotite and muscovite indicates plutons cooled very rapidly through mica closure temperatures by ~72.5 Ma. The muscovite age of 72.5 Ma is interpreted to be the age of peak deformation and time of most rapid cooling, followed by slower cooling through K-feldspar closure temperatures with MDD modeled rates of ~22 and 16 ˚C/m.y. The rapid cooling observed in Cretaceous plutons from the Bristol Mountains through upper MDD model ages is interpreted to be associated with tectonic exhumation via extension. Solid-state deformation of Late Cretaceous (75 Ma) plutons provides a maximum constraint on deformation. Furthermore, rapid cooling through mica (biotite and muscovite) closure temperatures suggests plutons underwent rapid cooling post-emplacement (~73-72 Ma).

Reconstructed T-t thermal profiles for the Bristol Mountains, coupled with deformation temperatures place broad constraints on mylonitic deformation (Figure 28). A maximum age of deformation is inferred from ~75 Ma to 65 Ma, using the U/Pb crystallization age of the mylonitically deformed Kg pluton and the small domain K-feldspar closure temperatures from MDD modeling as age brackets. The minimum age range of extensional deformation in the Bristol Mountains is inferred from ~75 to 72.5 Ma. Slower cooling rates recorded in K-feldspar MDD may suggestion erosion contributed to exhumation and was perhaps increasingly more important as extension waned. (Figure 28).

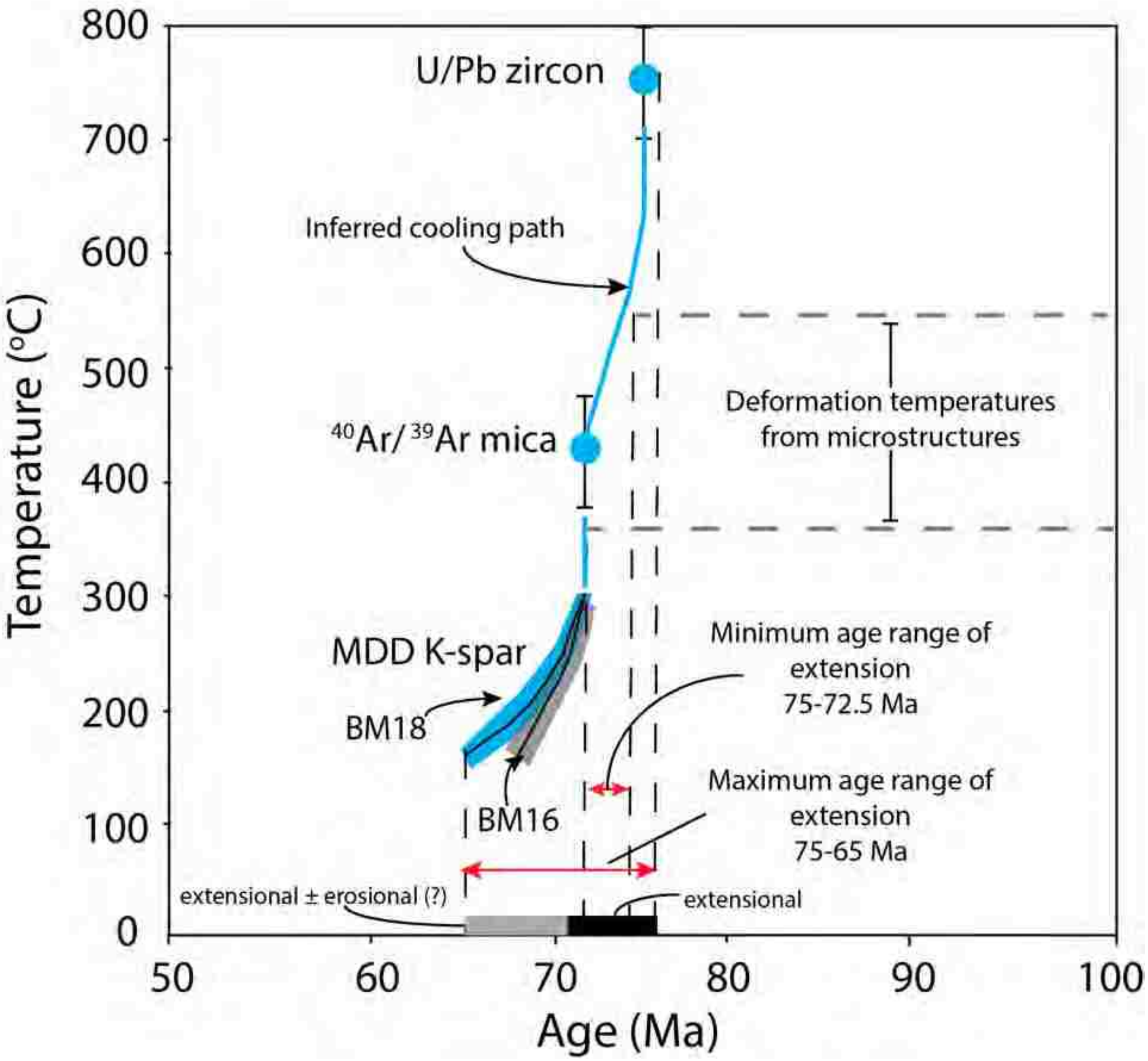

[redacted]

5.4 Tectonic Evolution and Displacement of the Bristol and Granite Mountains

5.4.1 Discrepancy between Shear Zone Geometries and Transport Directions

Several possible scenarios may explain the differences in shear zone geometry and kinematics between the Bristol and Granite mountains. Four scenarios are discussed herein to explain the tectonic evolution and displacement of the Bristol and Granite mountains, leading to the differences in shear zone geometries and kinematics. Firstly, during Miocene BCF deformation, assuming the Bristol and Granite mountains had the same initial geometry and kinematics, there was a hanging-wall vertical axis rotation, causing the Bristol Mountains and mylonitic fabrics therein to rotate anticlockwise relative to the Granite Mountains. This model assumes that rocks of the Bristol Mountains originated on top of or adjacent to the Granite Mountains prior to Cenozoic faulting. The amount of hanging-wall rotation would be ~78˚ anticlockwise. This is a large amount of HW rotation, considering the apparent slip (~4-6 km) associated with the BCF (Figure 29a).

Secondly, during displacement along the BGMFZ there was a vertical axis rotation across the fault. In this scenario, it is assumed that the Bristol Mountains originated adjacent to the Granite Mountains, and that progressive transport along the BGMFZ caused block rotation of the Bristol Mountains, with respect to the Granite Mountains, to present day geographic orientations. Lease et al. (2009), and others, suggest that there has been no net rotation across the BGMFZ. This model is considered an unlikely cause for the misorientation of shear zone geometry and kinematics between the Bristol and Granite Mountains (Figure 29b).

Thirdly, there has been no rotation of the shear zone(s), and the original geometries and kinematics are preserved, though displaced along the BGMFZ. This scenario assumes that the Bristol Mountains originated adjacent to the Granite Mountains prior to Cenozoic deformation, and dextral separation of the Bristol and Granite mountains would have taken place across the BGMFZ, with no net rotation. In this model, after restoring the Bristol Mountains along the BGMFZ to within geographic proximity of the Granite Mountains, the initial shear zone geometry would have formed a highly curved and arcuate shape wrapping around the present-day Granite Mountains to the south, where mylonitic shearing was top-to-the-SW. This scenario is considered likely, and removes the need for large scale vertical axis rotation across faults (Figure 29c).

Lastly, it is possible that the shear zone(s) present in the Bristol and Granite mountains are unrelated spatially, i.e., they were two different shear zones recording orthogonal kinematics and geometries. The geometry and hanging-wall transport direction for the Bristol Mountain shear zone are similar to those in the nearby Pinto shear zone in the New York Mountains (Wells et al., 2005). Furthermore, it is likely that the Bristol Mountains shear zone is related spatially and temporally to the East Mojave Fault proposed by Miller et al. (1996).

We consider the third and fourth scenarios as the most likely as the magnitudes of rotation required for options one and two are significantly larger than what has been documented either in extensional settings or in tectonic blocks within the Eastern California Shear Zone.

5.4.2 Temporal kinematic switch in exhumation

Plutons transecting the Granite Mountains demonstrate a spatial gradient in emplacement ages, cooling rates, and in onset of cooling. Reconstructed cooling paths show an inflection point with initial rapid cooling transitioning to slower cooling. Kula (2002) suggested a conjugate fault system to explain the gradients in cooling rates and inflection points observed. Kula (2002) sampled three locations transecting the Granite Mountains from NE – SW and noted that the NE sample was emplaced and conductively cooled through hornblende closure temperatures the earliest (~78 Ma), whereas the central and SW plutons were emplaced later and did not cool through hornblende closure temperatures until ~74 Ma. This was interpreted as the NE sample being near a top-to-the-

NE normal fault in the vicinity of Granite Pass, active from ~76-74 Ma. Furthermore, a top-to-the-NE normal fault, with the Granite Mountains in the footwall, would explain the juxtaposition of deep-seated Granite Mountain plutons with shallowly emplaced plutons in the Providence Mountains. Kula (2002) noted that the NE sample switched from initially fast cooling to slower cooling at a distinct inflection point, whereas the SW sample continued to cool very rapidly. The inflection in cooling across the Granite Mountains is interpreted as a tectonic switch from extension along a top-to-the NE normal fault to extension along a top-to-the-SW normal fault. Kula (2002) also concluded that bulk exhumation in the Late Cretaceous was likely associated with top-to-the-SW faulting.

This study adds two new samples to the Granite Mountains forming a SE-NW transect, which is parallel to the mylonitic transport direction preserved in the footwall of the BCF. The new sampling transect also demonstrates a distinct gradient in cooling rates. The NW pluton, which is closest to the NW mylonitic shear zone, was emplaced first (80 Ma) and cooled through hornblende closure temperatures by ~78 Ma, whereas the central pluton (GM313) was emplaced and cooled through hornblende temperatures by ~76 Ma. Emplacement and cooling ages suggests a top-to-the-NW normal fault, active from the emplacement of the NW pluton at ~80 Ma through ~76 Ma, assuming plutons are synextensional. The sampling transect here also demonstrates an inflection in T-t paths. Post ~74 Ma, the SE pluton cooled virtually instantaneously through upper K-feldspar MDD closure temperatures. Whereas the central and NW plutons continued cooling at slower and very similar rates, which may be suggestive of a kinematic switch in extension.

The Cretaceous plutons sampled on the Bristol Mountains sampling transect, parallel to the mylonitic transport direction, yield indistinguishable emplacement ages. Mica cooling ages, while complex in detail, are all broadly similar, indicating footwall cooling was nearly uniform through ~375 ˚C. K-feldspar MDD modeling suggests the pluton within the shear zone cooled slower and later (~65 Ma), whereas the sample from the footwall to the NE cooled through K- feldspar closure earlier (~67 Ma), which is expected to occur with a top-to-the-SW normal fault and progressive exhumation of the hanging wall. If the shear zone present in the Bristol Mountains is restored for slip along the BGMFZ to be adjacent to the Granite Mountains, the shear zone in the Bristol Mountains may be responsible for the exhumation of the Granite Mountains plutons along a top-to-the-SW normal fault proposed by Kula (2002). Figure 29c shows reconstruction of the Bristol Mountains along the BGMFZ to lie adjacent to the Granite Mountains. Reconstructed T-t thermal profiles from Kula (2002), and from this study, may indicate a polyphase history with kinematic switches in extension direction from a top-to-the-NW extension active from ~80-76 Ma, to top-to-the-NE extension active from ~76-74 Ma, and finally top-to-the-SW extension active from ~74-65 Ma (Figure 29d).

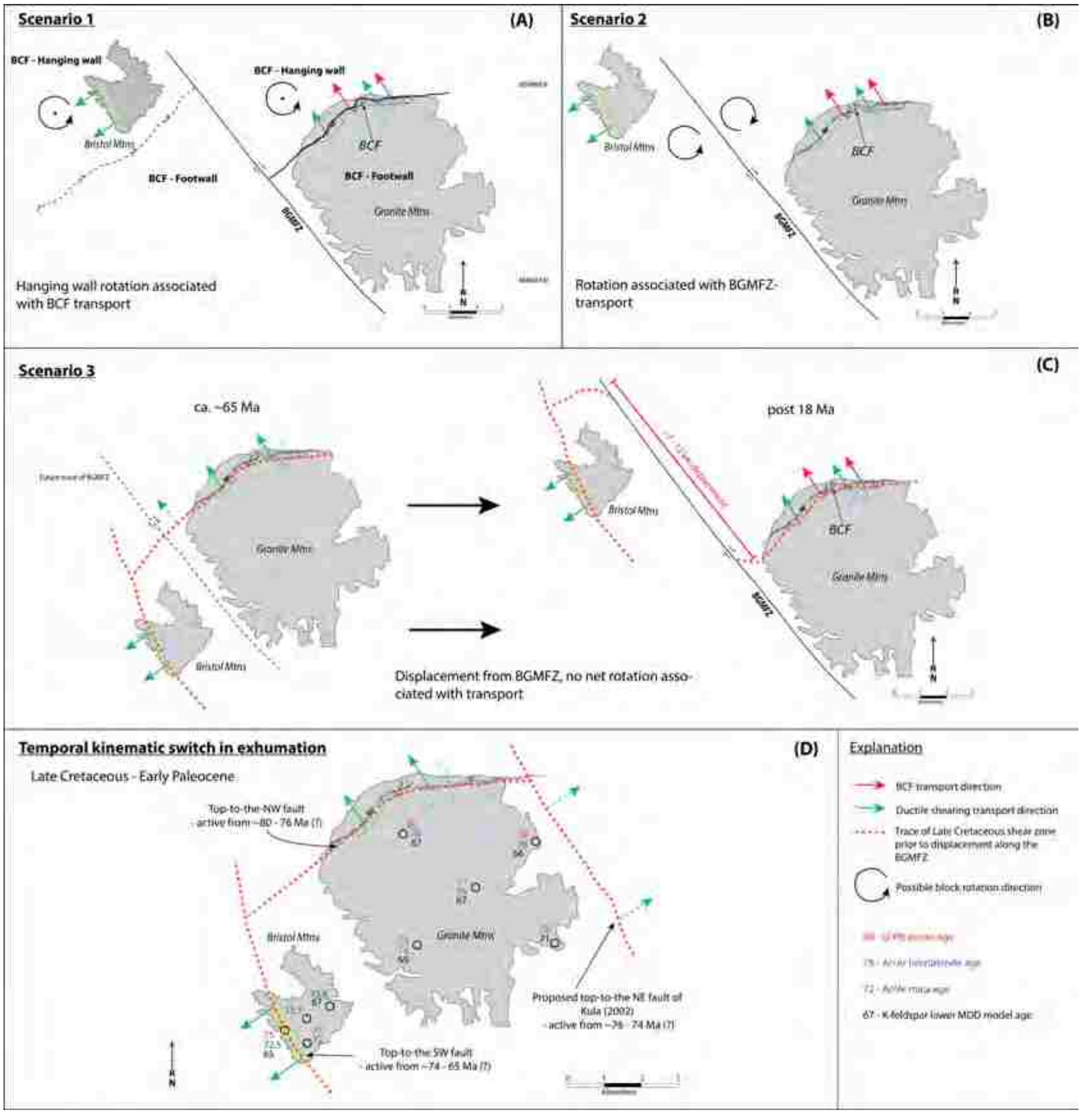
Scenario 1
(A)
BCF - Hanging wall
Bristol Mtns
BCF - Footwall
BCF - Hanging wall
BCF
BCF - Footwall
Granite Mtns
BGMFZ
Hanging wall rotation associated
with BCF transport
Scenario 2
(B)
Bristol Mtns
BCF
Granite Mtns
BGMFZ
Rotation associated with BGMFZ-
transport
Scenario 3
(C)
ca. ~65 Ma
post 18 Ma
Granite Mtns
Bristol Mtns
BCF
BGMFZ
Displacement from BGMFZ, no net rotation asso-
ciated with transport
Temporal kinematic switch in exhumation
(D)
Late Cretaceous - Early Paleocene
Top-to-the-NW fault
active from ~80 - 76 Ma (?)
Bristol Mtns
Granite Mtns
Proposed top-to-the NE fault of
Kula (2002)
- active from ~76 - 74 Ma (?)
Top-to-the SW fault
- active from ~74 - 65 Ma (?)
Explanation
BCF transport direction
Ductile shearing transport direction
Trace of Late Cretaceous shear zone
prior to displacement along the
BGMFZ
Possible block rotation direction
67 - K-feldspar lower MDD model age

[redacted]

5.5 Late Cretaceous Unroofing in the East Mojave Desert

Three examples from the Mojave Desert are chosen herein to show similarity in timing and kinematics for Late Cretaceous extension throughout the southwestern Cordillera: (1) the New York Mountains; (2) the Old Woman Mountains; and (3) the Iron Mountains. (1) The New York Mountains, located to the NE of the Granite Mountains (Figure 2a), are composed mainly of mid-late Cretaceous plutonic rocks, Cretaceous metavolcanic rocks, Paleozoic metasedimentary rocks, and Proterozoic basement gneisses (Burchfiel and Davis, 1977; Miller et al., 1991; Beyene, 2000; Smith et al., 2003; Wells et al., 2005). The Pinto shear zone in the southern New York Mountains records Late Cretaceous extension and rapid cooling of the Mid Hills Monzogranite. Kinematic indicators within the Pinto shear zone show a top-to-the-SW down-dip shearing, consistent with extensional deformation as opposed to shortening. Detailed $^{40}Ar/^{39}Ar$ thermochronology across the footwall of the Pinto shear zone constrains deformation to 74-68 Ma (Wells et al., 2005). K-feldspar MDD modeling indicates cooling of the footwall at a rate of 76-62˚C/m.y. (Wells et al., 2005). (2) The Old Woman Mountains, located to the ESE of the Granite Mountains (Figure 2a), are composed of Paleozoic metasedimentary rocks, Proterozoic basement rocks, and Mesozoic granitoid rocks. The Old Woman pluton exhibits synmagmatic and solid-state shearing interpreted as recording extension (Foster et al., 1989; Foster et al., 1992 McCaffrey et al., 1999). U/Pb geochronology and $^{40}Ar/^{39}Ar$ thermochronology indicates that the Old Woman pluton was emplaced at 74 Ma and cooled below the apatite fission track closure temperature of ~100˚C by 66 Ma (Carl et al., 1991; Foster et al., 1992). (3) The Iron Mountains are located to the SSE of the Granite Mountains (Figure 2a) and are composed of a Cretaceous sill complex, separated by screens of Precambrian metasedimentary rocks, in the roof of the Cadiz Valley Batholith (Miller and Howard, 1984). A Late Cretaceous porphyritic monzogranite (~ 75 Ma, Wells et al., 2002) forms the main phase of the batholith. Within the sills and overlying metasedimentary rocks a thick mylonitic shear zone with top-to-the-E kinematic indicators is present. $^{40}Ar/^{39}Ar$ cooling ages from biotite within the footwall of the shear zone, coupled with emplacement ages, brackets extensional deformation from 75 to 67 Ma. These data are temporally consistent with the Late Cretaceous extension observed in the Bristol and Granite mountains, demonstrating that Late Cretaceous extension was widespread across the Eastern Mojave region.

5.6 Causative Mechanisms for Exhumation and a Collapsing Orogen in the Late Cretaceous

Demonstrating the age and geographic extent of Late Cretaceous extension across the North American Cordillera is crucial to understanding the possible causes, as well as developing a robust geodynamic model for the Sevier and Laramide orogenies. Late Cretaceous cooling and partial exhumation of mid-to-lower crustal rocks was a widespread event across the North American Cordillera, from the Great Basin region to the SW Mojave Block (Hodges and Walker, 1992; Wells and Hoisch, 2008). Wells and others (2005) postulated that synconvergent extension was the major contributor to exhumation, which was caused by an orogen-wide delamination event of the North American lithospheric mantle. Geodynamical modeling by Liu et al. (2010) and others suggest subduction of the oceanic plateau rooted to the Farallon plate caused wide spread dynamic topographic responses. At the leading edge of the plateau, dynamic subsidence manifested in response to the basaltic plateau undergoing eclogitization causing a draw-down of the upper plate (Liu et al., 2010; Copeland et al., 2017). Furthermore, a dynamic uplift of the upper plate ensued subsequent to the passage of the plateau. A dynamic uplift in the Laramide deformational corridor and Mojave Block may have led to extension and exhumation during the latest Cretaceous to earliest Paleocene, but does not explain Late Cretaceous extension in the Great Basin region.

Many studies, discussed previously, demonstrate Late Cretaceous extension was a major event leading to the development and evolution of the southern Cordillera and Mojave region

(Foster et al., 1992; Hodges and Walker, 1992; Wells et al., 2002; Wells et al., 2005; Wells and Hoisch, 2008). Structures responsible for Late Cretaceous exhumation in the southern Cordillera are mostly preserved as low-angle ductile shear zones that are commonly overprinted and obscured by Cenozoic deformation. Kinematic studies from Late Cretaceous shear zones across the eastern Mojave Block indicate shear took place in three directions throughout the southern Cordillera, dominated by top-SW, top-NW, and top-NE structures. Structures across the eastern Mojave that demonstrate similar kinematics and footwall cooling histories were correlated by Miller et al. (1996) and interpreted to be part of a continuous shear zone belt from the Death Valley region to the southern Old Woman Mountains. Miller et al. (1996) speculated that the East Providence fault, Pinto shear zone, and Cima fault zone formed the East Mojave Fault zone, prior to disaggregation in the Cenozoic. These shear zones all demonstrate top-SW extension active from ~75-66 Ma. Kinematics, deformation age, and location from the Bristol Mountains fit well with the proposed East Mojave Fault of Miller et al. (1996), and may in fact be a fragment of the disaggregated East Mojave Fault zone. It is speculated herein that initial extensional deformation recorded in the Granite Mountains took place from ~80 Ma to 76 Ma along a top-NW structure and from ~76 Ma to 74 Ma along top-NE structures. Subsequently, deformation switched, and bulk exhumation and extension took place along a top-SW structure active from ~74-65 Ma.

Late Cretaceous extensional structures in the southern Mojave are unique, in that they are mostly associated with peraluminous crustal melts which are part of a larger belt of crustal melts within the Cordilleran interior (Miller and Bradfish, 1980; Patino Douce et al., 1990). Late Cretaceous Cordilleran peraluminous granites are chiefly attributed to crustal anatexis (Wright and Wooden, 1991). Wells et al. (2005) postulate that Late Cretaceous extension, anatexis, and magmatism implies delamination of the North American mantle lithosphere pre-75 Ma, occurring before the Farallon flat slab reached the eastern Mojave region (Figure 30). It is interpreted here that removal of the mantle lithosphere played a key role in providing adequate conditions for crustal anatexis to occur, leading to the production of Cordilleran-type peraluminuous granites. Furthermore, removal of the mantle lithosphere promoted uplift of the orogen through isostatic rebound, resulting in large variations in gravitational potential energy and highly unstable regions within the crust. Crustal anatexis together with an increase in gravitational potential energy could lead to extensional collapse. The cause for removal of the lithospheric mantle is debated. Delamination of a thick root developed beneath the overthickened Sevier orogen is postulated as a likely cause for removal of the mantle lithosphere (Wells et al., 2005; Wells and Hoisch, 2008; Wells and Hoisch, 2012). Delamination is proposed to have occurred before the eastward migration of the low-angle Farallon slab and development of the Laramide orogeny, and before the asthenospheric wedge was effectively removed from beneath the North American plate (Wells et al., 2005). Moreover, upwelling asthenospheric mantle after lithospheric removal would allow the production of mafic melts and crustal anatexis to occur. This also allows room for the flattening Farallon plate to couple with the overriding North American plate and begin to underplate Pelona-Orocopia-Rand schist. Removal of the mantle lithosphere via delamination is considered a probable cause for the Cordilleran-type magmatism and associated regional collapse of the Sevier orogen in the Late Cretaceous.

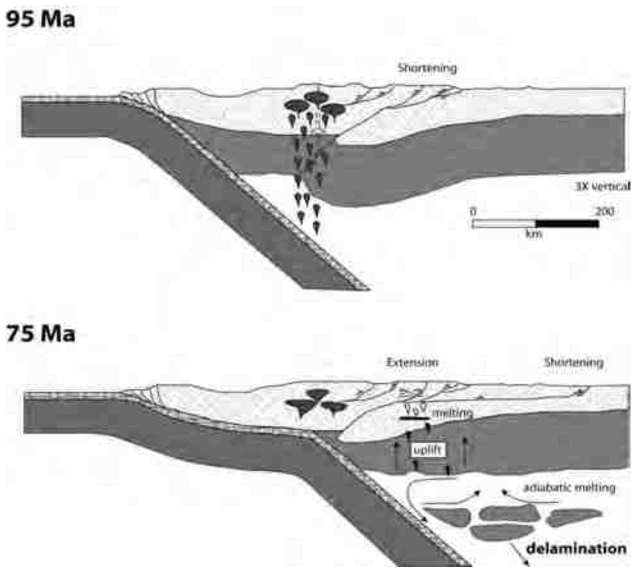

[redacted]

6. CONCLUSION

New data from the Bristol and Granite mountains in southeastern California demonstrate that ductile shear zones record crustal extension and rapid exhumation of mid-crustal rocks in the Late Cretaceous. Geochronology and thermochronology show that footwall(s) rocks were rapidly cooled from crystallization temperatures through lower temperature MDD K-feldspar model ages. Kinematic indicators from the Bristol Mountains shear zone indicates a top-to-the-SW non-coaxial downdip shear sense, and mylonitic fabric preserved in the Granite Mountains records top-to-the-NW non-coaxial downdip shearing – indicating extensional deformation. Microstructural analyses show deformation occurred at lower amphibolite to upper greenschist facies conditions. Microstructures also indicate a lower temperature overprint, suggesting a progressive unroofing of the shear zone during exhumation. Deformation temperatures coupled with geochronology and thermochronology bracket the age of extensional deformation in the Granite Mountains from ~80 Ma to 66 Ma and from ~75 Ma to 65 Ma in the Bristol Mountains.

These data provide unequivocal evidence for extensional collapse of the Sevier orogen in the Late Cretaceous. Moreover, removal of the mantle lithosphere during the Late Cretaceous is seemingly the ubiquitous cause for synconvergent extension in the southern Cordillera. This study supports the proposed delamination theory by Wells et al. (2005), Wells and Hoisch (2008), and Wells and Hoisch (2012) as being the root mechanism for removal of the mantle lithosphere in the Late Cretaceous, which led to crustal anatexis, peraluminuous magmatism, and extensional collapse – synchronous with continued contraction in the Sevier FTB as well as the nascent Laramide deformational belt to the north and south. Other mechanisms that explain exhumation and cooling are also considered. Erosion may be an important contributor to exhumation post-70 Ma, based on evidence for a highland (Kingman arch) existing in the southern Cordillera in the latest Cretaceous which was subsequently erosionally denuded, producing a widespread sub-Tertiary unconformity and shedding gravels onto the Colorado Plateau

Following Late Cretaceous extension, the southern Cordillera entered a period of tectonic quiescence until the development of the southern Basin and Range and Eastern California Shear Zone in the Neogene, which resulted in the final exhumation of the Bristol and Granite mountains. Detailed structural measurements and field mapping show that the Miocene (?) Bull Canyon Fault reactivated the top-to-the-NW Late Cretaceous extensional structure in the Granite Mountains. The Bull Canyon Fault apparently inherited the architecture of the Late Cretaceous shear zone, likely excising and/or displacing most of the earlier shear zone from the Granite Mountains. Restoration of the Bristol Mountains along the Bristol-Granite Mountain fault zone, approximately 8-10 km, would place the Bristol Mountains SW of the Granite Mountains; this configuration would allow the Granite Mountains to be in the footwall of the top-to-the-SW shear zone present in the Bristol

Mountains, and may be responsible for the continued exhumation of the Granite Mountains from ~75-66 Ma. It is interpreted that incipient extension and exhumation took place a long the top-to-the-NW structure present in the Granite Mountains from ~80-76 Ma, and continued extension occurred along top-to-the-SW structures active from ~76-65 Ma. These data and observations from the Bristol and Granite mountains provide key insight into the development and evolution of the North American Cordillera, from the Late Jurassic to Quaternary deformation, and informs our understanding of causitive mechanisms to explain regional Late Cretaceous cooling and exhumation of mid-to-lower crustal rocks.

APPENDIX A

U/Pb Geochronology Data Tables

LH15GM6

						Isotope ratios					Apparent ages (Ma)							
Analysis	U (ppm)	206Pb 204Pb	U/Th	206Pb* 207Pb*	± (%)	207Pb* 235U*	± (%)	206Pb* 238U	± (%)	error corr.	206Pb* 238U*	± (Ma)	207Pb* 235U	± (Ma)	206Pb* 207Pb*	± (Ma)	Best age (Ma)	± (Ma)
Spot 84	74	5718	3.0	24.3571	6.6	0.0653	7.3	0.0115	3.0	0.42	73.9	2.2	64.2	4.5	284.1	169.4	73.9	2.2
Spot 115	132	38440	2.1	20.0490	7.1	0.0834	7.5	0.0121	2.3	0.31	77.7	1.8	81.3	5.8	189.3	165.6	77.7	1.8
Spot 109	81	11067	2.8	19.8245	8.0	0.0848	8.4	0.0122	2.5	0.30	78.1	2.0	82.6	6.7	215.4	185.9	78.1	2.0
Spot 119	133	80855	4.1	21.4806	6.5	0.0783	6.9	0.0122	2.3	0.33	78.2	1.8	76.5	5.1	26.4	156.2	78.2	1.8
Spot 103	152	16953	3.4	21.7424	4.9	0.0774	5.5	0.0122	2.4	0.43	78.2	1.9	75.7	4.0	2.7	119.0	78.2	1.9
Spot 82	80	18130	2.4	21.1957	7.0	0.0799	7.5	0.0123	2.8	0.37	78.7	2.2	78.0	5.6	58.3	165.9	78.7	2.2
Spot 79	106	70747	3.9	20.1348	4.7	0.0841	5.0	0.0123	1.7	0.35	78.7	1.4	82.0	3.9	179.3	109.6	78.7	1.4
Spot 76	62	32158	2.2	21.0558	8.6	0.0805	9.2	0.0123	3.1	0.34	78.8	2.4	78.6	6.9	74.1	205.7	78.8	2.4
Spot 117	118	16230	2.5	19.3532	6.2	0.0877	6.5	0.0123	1.8	0.28	78.8	1.4	85.3	5.3	270.9	142.9	78.8	1.4
Spot 83	194	101240	2.5	20.0752	5.3	0.0851	5.8	0.0124	2.5	0.43	79.3	2.0	82.9	4.6	186.2	122.7	79.3	2.0
Spot 105	191	21507	1.3	20.5145	4.5	0.0834	4.9	0.0124	2.1	0.42	79.5	1.6	81.3	3.8	135.6	104.9	79.5	1.6
Spot 71	54	12518	1.9	20.6530	7.8	0.0829	9.2	0.0124	5.0	0.54	79.6	3.9	80.9	7.2	119.8	184.1	79.6	3.9
Spot 99	60	26667	1.4	18.3467	8.8	0.0935	9.7	0.0124	4.0	0.41	79.7	3.2	90.7	8.4	392.0	198.3	79.7	3.2
Spot 118	88	36979	1.8	20.9691	7.7	0.0823	8.2	0.0125	2.7	0.33	80.2	2.2	80.3	6.3	83.9	183.1	80.2	2.2
Spot 95	81	13474	3.1	21.6505	5.4	0.0797	5.8	0.0125	2.2	0.38	80.2	1.8	77.9	4.4	7.5	129.4	80.2	1.8
Spot 111	76	13529	1.1	19.8328	5.6	0.0871	5.9	0.0125	2.1	0.35	80.3	1.7	84.8	4.8	214.5	128.6	80.3	1.7
Spot 112	71	20806	3.1	19.7822	5.3	0.0874	6.2	0.0125	3.2	0.52	80.4	2.6	85.1	5.0	220.4	121.6	80.4	2.6
Spot 104	75	4405	2.8	23.5391	6.8	0.0736	7.3	0.0126	2.8	0.38	80.4	2.2	72.1	5.1	197.8	169.9	80.4	2.2
Spot 94	69	49992	2.6	21.5008	8.1	0.0806	8.4	0.0126	2.0	0.24	80.5	1.6	78.7	6.3	24.1	195.5	80.5	1.6
Spot 89	138	433573	1.2	20.7335	3.8	0.0836	4.4	0.0126	2.4	0.53	80.6	1.9	81.6	3.5	110.6	88.6	80.6	1.9
Spot 88	130	24574	2.3	22.1970	3.2	0.0782	4.3	0.0126	2.7	0.65	80.7	2.2	76.5	3.1	52.9	79.1	80.7	2.2
Spot 100	51	15608	3.8	21.1405	8.4	0.0822	8.8	0.0126	2.5	0.29	80.7	2.0	80.2	6.8	64.5	201.1	80.7	2.0
Spot 113	117	21624	2.7	20.3164	5.7	0.0856	6.0	0.0126	1.8	0.31	80.8	1.5	83.4	4.8	158.4	134.5	80.8	1.5

Spot 77	105	51670	3.6	18.3284	6.0	0.0949	6.4	0.0126	2.2	0.35	80.8	1.8	92.1	5.6	394.2	134.0	80.8	1.8
Spot 101	297	55140	2.2	18.1729	4.5	0.0959	4.9	0.0126	1.7	0.36	81.0	1.4	93.0	4.3	413.3	101.7	81.0	1.4
Spot 74	56	5518	2.5	23.6450	8.1	0.0738	8.9	0.0126	3.9	0.43	81.0	3.1	72.3	6.2	209.1	202.7	81.0	3.1
Spot 86	110	9884	2.4	21.5617	6.4	0.0809	6.9	0.0127	2.8	0.40	81.1	2.2	79.0	5.3	17.3	153.3	81.1	2.2
Spot 114	85	9703	3.0	23.2873	7.2	0.0752	7.9	0.0127	3.2	0.41	81.4	2.6	73.6	5.6	171.0	179.6	81.4	2.6
Spot 70	188	90811	1.5	20.7135	4.6	0.0846	6.7	0.0127	4.9	0.73	81.4	3.9	82.5	5.3	112.9	108.1	81.4	3.9
Spot 85	122	39247	1.5	17.3659	5.3	0.1013	5.9	0.0128	2.5	0.43	81.7	2.1	97.9	5.5	514.0	116.1	81.7	2.1
Spot 110	58	13761	3.2	21.2531	8.8	0.0828	9.1	0.0128	2.4	0.26	81.7	1.9	80.8	7.1	51.9	209.9	81.7	1.9
Spot 102	133	28789	1.9	18.4973	4.7	0.0952	5.6	0.0128	3.0	0.53	81.8	2.4	92.4	4.9	373.6	106.9	81.8	2.4
Spot 90	156	33483	2.9	19.8715	5.7	0.0887	6.1	0.0128	2.3	0.37	81.9	1.8	86.3	5.1	209.9	132.0	81.9	1.8
Spot 80	60	5060	2.9	22.2238	6.5	0.0802	7.4	0.0129	3.6	0.48	82.8	3.0	78.3	5.6	55.8	158.4	82.8	3.0
Spot 108	192	39153	2.6	20.6597	5.4	0.0865	6.4	0.0130	3.3	0.52	83.0	2.7	84.3	5.1	119.0	128.2	83.0	2.7
Spot 69	119	63051	1.8	19.6134	6.3	0.0913	9.5	0.0130	7.1	0.75	83.1	5.9	88.7	8.1	240.2	145.0	83.1	5.9
Spot 91	59	161994	2.7	19.3530	7.6	0.0930	8.7	0.0131	4.3	0.50	83.6	3.6	90.3	7.6	270.9	174.5	83.6	3.6
Spot 68	87	13879	2.5	21.0453	6.0	0.0861	11.6	0.0131	9.9	0.85	84.2	8.3	83.9	9.4	75.2	143.5	84.2	8.3
Spot 78	54	16879	2.3	19.4546	9.0	0.0932	10.0	0.0131	4.4	0.43	84.2	3.6	90.5	8.7	258.9	208.3	84.2	3.6
Spot 107	87	26398	2.5	20.6933	5.4	0.0884	5.9	0.0133	2.3	0.40	84.9	2.0	86.0	4.9	115.2	127.9	84.9	2.0
Spot 75	282	31971	1.5	20.9863	3.5	0.0875	4.0	0.0133	2.0	0.49	85.3	1.7	85.2	3.3	81.9	82.8	85.3	1.7
Spot 123	42	6023	2.2	20.4711	8.8	0.0913	9.5	0.0136	3.4	0.36	86.8	2.9	88.7	8.0	140.6	207.9	86.8	2.9
Spot 116	91	28430	3.2	15.8725	8.6	0.1187	9.0	0.0137	2.5	0.28	87.5	2.1	113.9	9.7	708.3	183.7	87.5	2.1
Spot 98	30	18500	1.5	8.7804	33.9	~~0.2206~~	~~34.0~~	~~0.0140~~	~~3.0~~	~~0.09~~	~~89.9~~	~~2.6~~	~~202.4~~	~~62.4~~	~~1862.4~~	~~630.7~~	~~89.9~~	~~2.6~~
Spot 93	144	20217	4.9	21.5219	5.3	0.0914	5.7	0.0143	2.2	0.38	91.3	2.0	88.8	4.9	21.8	127.2	91.3	2.0
Spot 61	89	72471	2.6	20.2844	6.5	0.1009	7.0	0.0148	2.6	0.37	95.0	2.5	97.6	6.5	162.1	151.5	95.0	2.5
Spot 81	86	15016	2.7	19.6278	4.9	0.1124	5.4	0.0160	2.3	0.42	102.3	2.3	108.2	5.6	238.5	114.0	102.3	2.3
Spot 96	226	128135	6.3	20.5349	4.1	0.1110	5.2	0.0165	3.2	0.62	105.7	3.4	106.9	5.3	133.3	96.2	105.7	3.4
Spot 124	83	45947	9.2	14.1448	11.5	0.1636	13.4	0.0168	6.8	0.51	107.3	7.2	153.9	19.1	948.7	237.1	107.3	7.2
Spot 97	28	4847	1.4	20.5399	8.9	0.1266	9.6	0.0189	3.7	0.38	120.4	4.4	121.0	11.0	132.7	208.8	120.4	4.4

LH15GM5

						Isotope ratios					Apparent ages (Ma)							
Analysis	U ppm	206Pb 204Pb	U/Th	206Pb* 207Pb*	± (%)	207Pb* 235U*	± (%)	206Pb* 238U	± (%)	error corr.	206Pb* 238U*	± (Ma)	207Pb* 235U	± (Ma)	206Pb* 207Pb*	± (Ma)	Best age (Ma)	± (Ma)
Spot 10	25	4831	1.5	17.4234	10.7	0.1824	11.4	0.0230	4.0	0.35	146.9	5.9	170.1	17.9	506.7	236.1	146.9	5.9
Spot 2	132	36583	2.3	17.6065	4.6	0.1827	5.4	0.0233	2.9	0.53	148.7	4.2	170.4	8.5	483.7	102.4	148.7	4.2
Spot 41	47	75844	2.3	18.2360	6.5	0.1780	7.1	0.0235	2.7	0.39	150.0	4.1	166.4	10.9	405.5	146.1	150.0	4.1
Spot 55	44	2978	2.7	15.9035	11.4	0.2047	12.3	0.0236	4.7	0.38	150.4	7.0	189.1	21.3	704.2	243.1	150.4	7.0
Spot 36	153	18076	3.4	20.2687	3.0	0.1635	3.7	0.0240	2.2	0.60	153.2	3.3	153.8	5.3	163.9	69.2	153.2	3.3
Spot121	24	8525	0.8	18.6737	9.1	0.1780	9.7	0.0241	3.3	0.34	153.5	5.0	166.3	14.8	352.2	205.2	153.5	5.0
Spot 3	48	3279	2.0	20.2020	9.3	0.1647	9.7	0.0241	2.9	0.30	153.7	4.4	154.8	13.9	171.6	216.3	153.7	4.4
Spot 25	21	1925	1.2	21.0977	9.8	0.1579	10.3	0.0242	3.3	0.32	153.9	5.0	148.9	14.3	69.4	233.6	153.9	5.0
Spot 6	23	7399	0.8	19.8325	9.7	0.1683	10.0	0.0242	2.5	0.25	154.2	3.8	157.9	14.6	214.5	224.5	154.2	3.8
Spot 26	31	8169	1.3	18.1432	7.6	0.1845	8.7	0.0243	4.2	0.49	154.6	6.4	171.9	13.7	417.0	168.9	154.6	6.4
Spot 51	37	15865	1.0	18.8188	7.8	0.1806	8.5	0.0246	3.5	0.41	157.0	5.4	168.6	13.2	334.7	176.0	157.0	5.4
Spot 57	28	4758	0.7	18.2091	8.3	0.1867	9.0	0.0247	3.4	0.38	157.0	5.3	173.8	14.3	408.8	185.7	157.0	5.3
Spot 39	197	21405	1.6	19.6480	3.5	0.1731	4.0	0.0247	2.0	0.49	157.1	3.1	162.1	6.1	236.1	81.2	157.1	3.1
Spot 59	116	111607	1.2	20.3086	3.5	0.1681	4.1	0.0248	2.1	0.51	157.6	3.3	157.7	6.0	159.3	83.0	157.6	3.3
Spot 19	51	13986	0.6	20.6911	5.4	0.1653	5.9	0.0248	2.5	0.43	158.0	4.0	155.4	8.5	115.5	126.3	158.0	4.0
Spot 42	36	17611	0.9	20.8688	8.5	0.1641	9.1	0.0248	3.3	0.36	158.1	5.1	154.3	13.0	95.2	200.7	158.1	5.1
Spot 5	66	7698	1.0	19.5218	5.2	0.1756	5.6	0.0249	1.9	0.35	158.3	3.0	164.3	8.4	250.9	120.1	158.3	3.0
Spot 29	32	8763	1.2	18.5713	8.7	0.1849	9.0	0.0249	2.5	0.27	158.6	3.9	172.2	14.3	364.6	196.5	158.6	3.9
Spot 31	228	22282	0.6	19.7622	3.6	0.1744	3.9	0.0250	1.5	0.39	159.1	2.4	163.2	5.9	222.7	83.3	159.1	2.4
Spot 32	47	6691	0.8	22.4874	6.7	0.1539	7.2	0.0251	2.6	0.36	159.8	4.1	145.3	9.8	84.6	164.9	159.8	4.1
Spot 21	43	9384	0.7	19.8551	5.1	0.1745	5.7	0.0251	2.5	0.45	160.0	4.0	163.3	8.6	211.8	117.8	160.0	4.0
Spot 9	651	36605	0.9	20.0506	2.0	0.1734	3.1	0.0252	2.3	0.75	160.5	3.7	162.3	4.6	189.1	47.6	160.5	3.7

Spot 47	59	6117	1.6	21.6794	3.6	0.1605	4.7	0.0252	3.0	0.65	160.7	4.8	151.1	6.6	4.3	85.9	160.7	4.8
Spot 13	3158	52753	12.6	20.2251	1.5	0.1720	3.5	0.0252	3.1	0.90	160.7	5.0	161.2	5.2	168.9	35.2	160.7	5.0
Spot 16	123	17360	1.4	20.1494	5.9	0.1734	6.2	0.0253	1.9	0.30	161.4	3.0	162.4	9.3	177.6	137.6	161.4	3.0
Spot 40	35	7733	1.3	20.0801	6.6	0.1744	7.3	0.0254	3.0	0.42	161.7	4.8	163.2	10.9	185.7	153.6	161.7	4.8
Spot 44	23	4411	1.1	19.3464	9.5	0.1824	10.2	0.0256	3.6	0.36	162.9	5.8	170.1	15.9	271.7	218.2	162.9	5.8
Spot 33	48	2499	1.4	23.5979	7.4	0.1497	7.9	0.0256	2.9	0.37	163.1	4.7	141.7	10.5	204.1	185.4	163.1	4.7
Spot 12	57	23824	1.3	18.7963	5.0	0.1882	5.3	0.0257	1.8	0.34	163.3	2.9	175.1	8.5	337.4	112.2	163.3	2.9
Spot 1	21	2702	0.7	22.2041	10.0	0.1595	10.6	0.0257	3.4	0.32	163.5	5.5	150.3	14.8	53.6	244.2	163.5	5.5
Spot 7	36	15334	0.8	19.7794	7.1	0.1795	7.8	0.0257	3.2	0.40	163.9	5.1	167.6	12.1	220.7	165.4	163.9	5.1
Spot 53	29	12576	0.7	20.4224	7.5	0.1746	7.9	0.0259	2.6	0.33	164.6	4.3	163.4	12.0	146.2	176.0	164.6	4.3
Spot 38	36	4623	0.8	10.9129	12.2	~~0.3296~~	~~12.6~~	~~0.0261~~	~~3.3~~	~~0.26~~	~~166.0~~	~~5.3~~	~~289.2~~	~~31.8~~	~~1459.8~~	~~232.5~~	~~166.0~~	~~5.3~~
Spot 14	200	8930	0.6	9.9694	6.0	~~0.3643~~	~~6.5~~	~~0.0263~~	~~2.5~~	~~0.39~~	~~167.6~~	~~4.2~~	~~315.4~~	~~17.6~~	~~1629.8~~	~~111.4~~	~~167.6~~	~~4.2~~
Spot 23	258	43105	3.1	19.0787	3.5	0.1934	5.6	0.0268	4.4	0.79	170.2	7.4	179.5	9.3	303.5	79.2	170.2	7.4
Spot 27	141	40988	2.4	19.7758	3.3	0.1949	4.4	0.0279	3.0	0.67	177.7	5.2	180.8	7.3	221.1	76.0	177.7	5.2
Spot 28	39	2070	2.7	22.7692	8.5	0.1720	9.0	0.0284	3.1	0.34	180.6	5.5	161.2	13.5	115.2	209.8	180.6	5.5
Spot 4	76	13002	4.0	17.6505	4.3	0.2502	5.3	0.0320	3.2	0.60	203.2	6.3	226.7	10.8	478.1	94.2	203.2	6.3
Spot 43	196	38164	3.9	14.7588	6.9	~~0.3655~~	~~7.5~~	~~0.0391~~	~~3.0~~	~~0.41~~	~~247.4~~	~~7.4~~	~~316.3~~	~~20.4~~	~~861.1~~	~~142.4~~	~~247.4~~	~~7.4~~
Spot 87	869	259930	91.6	10.2277	1.2	3.2097	2.3	0.2381	1.9	0.85	1376.8	24.0	1459.5	17.6	1582.1	22.2	1582.1	22.2

LH15BM4

						Isotope ratios					Apparent ages (Ma)							
Analysis	U ppm	206Pb 204Pb	U/Th	206Pb* 207Pb*	± %	207Pb* 235U*	± (%)	206Pb* 238U	± (%)	error corr.	206Pb* 238U*	± (Ma)	207Pb* 235U	± (Ma)	206Pb* 207Pb*	± (Ma)	Best age (Ma)	± (Ma)
Spot 1	238	26996	1.1	19.7422	2.3	0.1766	3.6	0.0253	2.8	0.76	160.9	4.4	165.1	5.5	225.0	53.9	160.9	4.4
Spot 2	39	11208	5.4	17.9096	4.8	0.1907	5.9	0.0248	3.4	0.57	157.7	5.2	177.2	9.5	445.8	106.9	157.7	5.2
Spot 3	270	27233	6.3	20.0865	3.7	0.1633	4.5	0.0238	2.6	0.57	151.6	3.8	153.6	6.4	184.9	86.8	151.6	3.8
Spot 4	871	85013	19.1	20.5209	2.2	0.1649	5.2	0.0245	4.7	0.91	156.3	7.3	155.0	7.5	134.9	52.2	156.3	7.3
Spot 5	121	19744	0.8	19.7290	4.1	0.1744	5.6	0.0250	3.7	0.67	158.9	5.9	163.3	8.4	226.6	95.7	158.9	5.9
Spot 6	252	30448	6.5	20.3554	3.8	0.1583	5.4	0.0234	3.8	0.71	148.9	5.7	149.2	7.5	153.9	88.6	148.9	5.7
Spot 7	200	108936	4.8	19.4748	3.2	0.1738	4.1	0.0245	2.5	0.63	156.3	3.9	162.7	6.1	256.5	72.7	156.3	3.9
Spot 8	235	54940	1.8	21.0115	4.7	0.1555	5.8	0.0237	3.3	0.57	150.9	4.9	146.7	7.9	79.1	112.4	150.9	4.9
Spot 9	63	68757	1.0	19.5733	5.2	0.1767	6.2	0.0251	3.3	0.54	159.7	5.3	165.3	9.4	244.9	119.8	159.7	5.3
Spot 10	88	48716	1.6	20.0856	5.7	0.1676	6.4	0.0244	2.8	0.44	155.5	4.4	157.3	9.3	185.0	133.1	155.5	4.4
Spot 11	46	3747	1.0	21.2322	7.0	0.1621	8.0	0.0250	3.9	0.49	159.0	6.1	152.6	11.3	54.2	166.7	159.0	6.1
Spot 12	77	26751	1.5	18.8783	5.2	0.1939	5.9	0.0265	2.8	0.47	168.9	4.6	179.9	9.7	327.6	118.0	168.9	4.6
Spot 13	49	8986	1.7	18.7734	7.3	0.1823	8.3	0.0248	4.1	0.49	158.1	6.3	170.1	13.0	340.2	164.4	158.1	6.3
Spot 14	69	9060	1.1	18.6997	4.8	0.1798	6.1	0.0244	3.6	0.60	155.3	5.6	167.9	9.4	349.1	109.6	155.3	5.6
Spot 15	137	37251	2.0	19.6889	4.8	0.1740	5.1	0.0248	1.9	0.36	158.2	2.9	162.9	7.7	231.3	110.3	158.2	2.9
Spot 16	119	12599	2.9	19.5678	4.2	0.1736	5.0	0.0246	2.7	0.54	156.9	4.2	162.5	7.5	245.5	97.2	156.9	4.2
Spot 17	87	19000	1.0	20.2170	6.4	0.1693	6.8	0.0248	2.3	0.33	158.1	3.5	158.8	10.0	169.8	149.3	158.1	3.5
Spot 18	205	13430	1.7	18.7372	5.4	0.1834	5.7	0.0249	1.9	0.33	158.7	2.9	170.9	9.0	344.6	122.5	158.7	2.9
Spot 19	455	33027	1.3	20.1023	3.3	0.1640	3.8	0.0239	1.8	0.48	152.3	2.7	154.2	5.4	183.1	76.9	152.3	2.7
Spot 20	72	14032	0.9	19.8832	5.6	0.1738	6.0	0.0251	2.2	0.36	159.5	3.4	162.7	9.0	208.6	129.1	159.5	3.4
Spot 21	509	34409	16.2	20.4928	1.9	0.1660	2.9	0.0247	2.3	0.77	157.1	3.5	155.9	4.2	138.1	43.8	157.1	3.5

Spot 22	66	23479	3.9	21.4930	6.2	0.1603	7.0	0.0250	3.1	0.45	159.1	4.9	151.0	9.8	25.0	149.7	159.1	4.9
Spot 23	52	7904	3.7	17.6672	10.2	0.1817	10.8	0.0233	3.6	0.33	148.3	5.3	169.5	16.8	476.1	225.2	148.3	5.3
Spot 24	236	31124	1.9	20.1770	3.6	0.1589	4.5	0.0232	2.7	0.60	148.2	3.9	149.7	6.2	174.5	83.4	148.2	3.9
Spot 25	690	47508	2.5	20.6531	2.0	0.1648	3.4	0.0247	2.8	0.80	157.2	4.3	154.9	4.9	119.8	48.2	157.2	4.3
Spot 26	386	120729	3.6	20.0323	3.0	0.1759	3.9	0.0255	2.4	0.62	162.6	3.9	164.5	5.9	191.3	70.3	162.6	3.9
Spot 27	290	33469	2.0	20.6271	3.0	0.1672	3.8	0.0250	2.3	0.60	159.3	3.6	157.0	5.5	122.7	71.6	159.3	3.6
Spot 28	69	5820	1.7	21.5756	6.4	0.1661	7.1	0.0260	3.1	0.44	165.4	5.1	156.0	10.3	15.8	153.8	165.4	5.1
Spot 29	136	11667	1.5	16.6394	5.8	0.2091	6.3	0.0252	2.5	0.40	160.7	4.0	192.8	11.1	607.1	125.6	160.7	4.0
Spot 30	57	13057	1.8	19.9581	6.9	0.1775	8.0	0.0257	4.0	0.50	163.5	6.4	165.9	12.2	199.9	160.7	163.5	6.4
Spot 40	100	12658	1.5	21.4388	5.7	0.1609	6.6	0.0250	3.3	0.50	159.3	5.2	151.5	9.3	31.1	136.1	159.3	5.2
Spot 41	600	44287	14.8	19.7437	2.8	0.1705	3.6	0.0244	2.2	0.62	155.5	3.4	159.9	5.3	224.9	64.7	155.5	3.4
Spot 42	128	22818	1.2	20.2540	4.3	0.1678	4.7	0.0247	1.9	0.39	157.0	2.9	157.5	6.9	165.6	101.1	157.0	2.9
Spot 43	27	2799	1.7	17.6214	8.7	0.1820	9.6	0.0233	4.1	0.43	148.2	6.0	169.8	15.0	481.8	192.5	148.2	6.0
Spot 44	79	4953	1.7	19.4327	6.5	0.1712	7.2	0.0241	3.1	0.43	153.7	4.7	160.4	10.6	261.5	149.0	153.7	4.7
Spot 45	79	8091	1.5	21.7416	7.5	0.1564	7.8	0.0247	2.1	0.27	157.0	3.3	147.5	10.7	2.6	181.6	157.0	3.3
Spot 46	75	3844	1.5	22.1612	4.3	0.1596	5.0	0.0257	2.6	0.52	163.3	4.2	150.4	7.0	48.9	103.6	163.3	4.2
Spot 47	89	40992	1.7	19.1703	5.8	0.1799	6.2	0.0250	2.2	0.36	159.3	3.5	168.0	9.6	292.6	131.8	159.3	3.5
Spot 48	169	34721	1.5	20.4068	4.0	0.1724	4.5	0.0255	2.2	0.48	162.4	3.5	161.5	6.8	148.0	93.3	162.4	3.5
Spot 49	129	44013	0.8	20.2870	4.6	0.1656	5.4	0.0244	2.9	0.53	155.2	4.4	155.6	7.8	161.8	107.0	155.2	4.4
Spot 50	53	33303	1.5	19.5034	7.9	0.1739	9.4	0.0246	5.1	0.54	156.6	7.8	162.8	14.1	253.1	182.4	156.6	7.8
Spot 51	61	4211	1.0	19.6608	6.4	0.1704	7.2	0.0243	3.1	0.44	154.8	4.8	159.8	10.6	234.6	148.9	154.8	4.8
Spot 52	256	16097	2.6	19.5897	4.0	0.1701	4.7	0.0242	2.6	0.55	154.0	4.0	159.5	7.0	242.9	91.3	154.0	4.0
Spot 53	90	7649	1.0	20.6247	4.1	0.1684	5.0	0.0252	2.9	0.59	160.4	4.7	158.1	7.3	123.0	95.6	160.4	4.7
Spot 54	332	25631	1.9	20.0143	3.3	0.1611	4.1	0.0234	2.4	0.57	149.0	3.5	151.7	5.8	193.4	77.8	149.0	3.5
Spot 55	117	82686	1.6	19.3838	3.1	0.1863	4.3	0.0262	3.1	0.71	166.6	5.0	173.4	6.9	267.2	70.5	166.6	5.0
Spot 56	150	39660	1.4	20.1701	3.1	0.1763	3.9	0.0258	2.5	0.63	164.1	4.0	164.9	6.0	175.2	71.3	164.1	4.0
Spot 57	133	11882	1.9	20.9262	5.8	0.1606	6.5	0.0244	2.9	0.45	155.2	4.4	151.2	9.1	88.8	137.5	155.2	4.4
Spot 58	57	72274	1.0	19.5664	6.6	0.1704	7.3	0.0242	3.0	0.41	154.0	4.6	159.8	10.8	245.7	152.7	154.0	4.6

Spot 59	481	45490	1.8	20.6073	2.9	0.1753	3.5	0.0262	2.0	0.57	166.7	3.3	164.0	5.3	125.0	67.9	166.7	3.3
Spot 60	34	3128	1.5	21.8952	8.1	0.1525	10.2	0.0242	6.3	0.61	154.2	9.5	144.1	13.7	19.6	195.1	154.2	9.5
Spot 61	252	14847	2.1	20.7678	2.8	0.1604	4.5	0.0242	3.5	0.78	153.9	5.3	151.1	6.3	106.7	66.6	153.9	5.3
Spot 62	111	4802	4.9	21.1512	5.9	0.1587	6.1	0.0243	1.7	0.28	155.1	2.6	149.6	8.5	63.3	140.5	155.1	2.6
Spot 63	52	2926	1.5	20.2389	7.9	0.1637	8.4	0.0240	3.0	0.36	153.0	4.6	153.9	12.1	167.3	184.1	153.0	4.6
Spot 64	80	75095	5.3	20.2637	5.4	0.1683	6.1	0.0247	2.9	0.48	157.5	4.6	157.9	9.0	164.4	125.7	157.5	4.6
Spot 65	41	151417	1.6	18.9536	8.6	0.1813	9.4	0.0249	3.6	0.38	158.7	5.6	169.2	14.6	318.5	196.9	158.7	5.6

LH15BM9

						Isotope ratios					Apparent ages (Ma)							
Analysis	U (ppm)	206Pb 204Pb	U/Th	206Pb* 207Pb*	± (%)	207Pb* 235U*	± (%)	206Pb* 238U	± (%)	error corr.	206Pb* 238U*	± (Ma)	207Pb* 235U	± (Ma)	206Pb* 207Pb*	± (Ma)	Best age (Ma)	± (Ma)
Spot 70	879	43054	2.0	21.1900	3.6	0.0764	5.9	0.0117	4.7	0.79	75.2	3.5	74.7	4.3	59.0	85.6	75.2	3.5
Spot 71	916	30634	1.3	21.0416	2.3	0.0791	3.2	0.0121	2.2	0.70	77.3	1.7	77.3	2.4	75.7	53.6	77.3	1.7
Spot 72	586	37812	1.7	20.2712	2.1	0.1234	2.7	0.0181	1.7	0.63	115.9	1.9	118.1	3.0	163.6	48.7	115.9	1.9
Spot 73	143	159381	3.9	20.1776	4.6	0.1901	5.3	0.0278	2.7	0.51	176.9	4.7	176.7	8.6	174.4	107.3	176.9	4.7
Spot 74	47	3359	0.8	20.7440	6.8	0.1697	8.1	0.0255	4.4	0.54	162.5	7.0	159.1	11.9	109.4	161.0	162.5	7.0
Spot 75	736	76958	2.3	20.8058	2.7	0.0747	3.7	0.0113	2.5	0.67	72.3	1.8	73.1	2.6	102.4	64.9	72.3	1.8
Spot 76	59	3743	1.1	19.9682	6.7	0.1816	7.6	0.0263	3.6	0.47	167.3	5.9	169.4	11.9	198.7	156.4	167.3	5.9
Spot 77	881	19687	2.5	20.6728	2.4	0.0771	3.4	0.0116	2.5	0.72	74.1	1.8	75.4	2.5	117.5	55.6	74.1	1.8
Spot 78	60	1711	1.2	28.9579	7.1	0.0585	7.9	0.0123	3.4	0.43	78.7	2.7	57.7	4.4	746.2	199.8	78.7	2.7
Spot 79	110	18599	1.4	21.0874	5.4	0.1482	5.9	0.0227	2.3	0.39	144.5	3.3	140.3	7.7	70.5	128.9	144.5	3.3
Spot 80	465	48540	2.8	20.3441	2.8	0.0832	3.5	0.0123	2.1	0.61	78.7	1.7	81.2	2.8	155.2	65.9	78.7	1.7
Spot 81	449	47608	3.6	20.3362	3.5	0.0839	4.7	0.0124	3.2	0.67	79.3	2.5	81.8	3.7	156.1	82.5	79.3	2.5
Spot 82	741	27292	1.0	21.2737	2.2	0.0747	3.7	0.0115	3.0	0.81	73.9	2.2	73.1	2.6	49.6	52.3	73.9	2.2
Spot 83	358	47098	2.9	19.8386	4.0	0.0809	5.2	0.0116	3.3	0.64	74.6	2.5	79.0	4.0	213.8	93.1	74.6	2.5
Spot 84	291	33037	2.5	19.9612	3.2	0.0950	5.4	0.0138	4.4	0.80	88.0	3.8	92.1	4.8	199.5	74.7	88.0	3.8
Spot 85	263	38014	1.8	20.7846	2.7	0.1513	3.4	0.0228	2.1	0.61	145.3	3.0	143.0	4.5	104.8	63.7	145.3	3.0
Spot 86	544	13809	3.6	20.5022	2.9	0.0787	3.8	0.0117	2.5	0.66	75.0	1.9	76.9	2.8	137.1	67.0	75.0	1.9
Spot 87	594	31485	6.5	19.9328	2.7	0.1561	3.7	0.0226	2.6	0.69	143.9	3.7	147.3	5.1	202.8	62.4	143.9	3.7
Spot 88	1126	24507	2.4	20.4705	2.9	0.0788	3.9	0.0117	2.6	0.67	75.0	1.9	77.1	2.9	140.7	67.5	75.0	1.9
Spot 89	571	29523	1.7	21.4043	4.0	0.0759	4.5	0.0118	2.0	0.45	75.5	1.5	74.2	3.2	34.9	95.4	75.5	1.5
Spot 90	146	26244	4.0	21.9998	4.8	0.0776	5.7	0.0124	3.0	0.52	79.3	2.3	75.9	4.1	31.2	117.2	79.3	2.3
Spot 91	372	21046	1.9	20.5996	2.8	0.1601	3.6	0.0239	2.2	0.62	152.4	3.4	150.8	5.0	125.9	66.0	152.4	3.4
Spot 92	914	34514	3.1	21.7084	2.8	0.0753	3.7	0.0119	2.3	0.64	76.0	1.8	73.7	2.6	1.0	67.8	76.0	1.8
Spot 94	720	30278	1.9	21.4280	3.5	0.0750	4.4	0.0117	2.6	0.59	74.7	1.9	73.5	3.1	32.3	84.0	74.7	1.9
Spot 95	585	64515	2.9	21.1792	2.7	0.0770	3.6	0.0118	2.4	0.66	75.8	1.8	75.3	2.6	60.2	63.8	75.8	1.8

Spot 96	140	18621	1.1	19.5383	5.0	0.1658	5.9	0.0235	3.1	0.52	149.7	4.5	155.8	8.5	249.0	116.0	149.7	4.5
Spot 97	359	53879	1.4	20.6870	3.4	0.0765	4.0	0.0115	2.0	0.51	73.6	1.5	74.9	2.9	115.9	81.0	73.6	1.5
Spot 98	320	34797	5.5	21.3084	5.2	0.0834	5.6	0.0129	2.0	0.37	82.5	1.7	81.3	4.4	45.7	124.2	82.5	1.7
Spot 99	139	6222	2.1	21.5181	6.1	0.0753	7.3	0.0117	3.9	0.54	75.3	2.9	73.7	5.2	22.2	147.1	75.3	2.9
Spot 100	688	31979	3.3	20.5027	2.7	0.0797	3.8	0.0118	2.7	0.70	75.9	2.0	77.8	2.9	137.0	64.5	75.9	2.0
Spot 101	843	67289	3.0	21.0057	2.7	0.0792	3.2	0.0121	1.6	0.50	77.3	1.2	77.4	2.4	79.7	65.0	77.3	1.2
Spot 102	268	16768	1.1	20.9953	4.2	0.0802	4.9	0.0122	2.6	0.52	78.2	2.0	78.3	3.7	80.9	99.9	78.2	2.0
Spot 103	212	18314	1.4	21.0185	4.1	0.1235	4.7	0.0188	2.3	0.49	120.3	2.7	118.3	5.2	78.3	97.3	120.3	2.7
Spot 104	1773	33391	4.1	21.1852	1.5	0.0785	2.2	0.0121	1.6	0.72	77.3	1.2	76.7	1.6	59.5	36.3	77.3	1.2
Spot 105	636	36772	1.7	21.7886	2.8	0.0763	3.5	0.0121	2.2	0.61	77.3	1.7	74.7	2.5	7.8	67.2	77.3	1.7
Spot 106	49	3082	1.8	23.3137	7.5	0.1344	7.9	0.0227	2.6	0.33	144.8	3.8	128.0	9.6	173.8	187.1	144.8	3.8
Spot 107	892	57299	2.9	20.7516	2.1	0.0787	3.5	0.0118	2.8	0.80	75.9	2.1	76.9	2.6	108.6	49.6	75.9	2.1
Spot 108	606	47947	4.0	20.0993	2.2	0.1560	3.9	0.0227	3.2	0.83	145.0	4.6	147.2	5.3	183.4	50.4	145.0	4.6
Spot 109	29	3750	1.0	16.7369	12.4	0.0976	13.5	0.0118	5.2	0.39	75.9	4.0	94.6	12.2	594.5	270.6	75.9	4.0
Spot 110	125	39681	4.1	16.9418	2.4	0.6934	3.4	0.0852	2.5	0.72	527.1	12.4	534.9	14.2	568.1	51.8	527.1	12.4
Spot 111	38	9786	0.8	16.3000	10.8	0.0959	11.5	0.0113	4.0	0.35	72.7	2.9	93.0	10.2	651.5	232.4	72.7	2.9
Spot 112	151	6846	1.9	20.2523	5.3	0.0780	6.1	0.0115	3.0	0.50	73.4	2.2	76.3	4.5	165.8	123.5	73.4	2.2
Spot 113	917	25654	2.3	20.8421	2.4	0.0756	3.2	0.0114	2.2	0.68	73.3	1.6	74.0	2.3	98.3	55.9	73.3	1.6
Spot 114	144	8659	1.6	20.1304	5.1	0.1404	6.0	0.0205	3.1	0.52	130.8	4.0	133.4	7.5	179.8	118.6	130.8	4.0
Spot 115	47	7189	0.9	21.0740	8.2	0.1730	8.5	0.0264	2.1	0.24	168.2	3.4	162.0	12.7	72.0	195.7	168.2	3.4
Spot 116	1344	763948	17.8	9.5489	0.7	3.9200	2.4	0.2715	2.3	0.96	1548.3	32.3	1617.8	19.8	1709.5	12.8	1709.5	12.8
Spot 117	1032	106234	2.1	20.3358	1.9	0.0792	3.3	0.0117	2.7	0.82	74.8	2.0	77.4	2.4	156.2	44.2	74.8	2.0
Spot 118	142	25244	1.1	20.8382	3.0	0.1528	4.4	0.0231	3.2	0.73	147.2	4.7	144.4	5.9	98.7	71.1	147.2	4.7
Spot 119	219	30998	1.5	20.3602	2.2	0.1526	2.7	0.0225	1.5	0.56	143.7	2.1	144.2	3.6	153.3	52.3	143.7	2.1
Spot 120	105	3708	1.1	22.8013	6.8	0.0689	7.4	0.0114	2.9	0.39	73.1	2.1	67.7	4.8	118.7	167.2	73.1	2.1
Spot 121	782	40984	1.8	21.1740	3.5	0.0743	4.3	0.0114	2.4	0.57	73.1	1.8	72.7	3.0	60.8	83.4	73.1	1.8
Spot 122	495	150450	2.0	20.4989	2.0	0.0802	2.9	0.0119	2.1	0.72	76.4	1.6	78.3	2.2	137.4	47.8	76.4	1.6
Spot 123	98	8776	1.8	20.1136	4.4	0.1207	4.7	0.0176	1.8	0.39	112.5	2.1	115.7	5.2	181.8	101.5	112.5	2.1

LH15BM18

						Isotope ratios					Apparent ages (Ma)							
Analysis	U (ppm)	206Pb 204Pb	U/Th	206Pb* 207Pb*	± (%)	207Pb* 235U*	± (%)	206Pb* 238U	± (%)	error corr.	206Pb* 238U*	± (Ma)	207Pb* 235U	± (Ma)	206Pb* 207Pb*	± (Ma)	Best age (Ma)	± (Ma)
Spot 65	807	34913	0.9	20.4375	1.2	0.0778	2.7	0.0115	2.4	0.90	74.0	1.8	76.1	2.0	144.4	27.5	74.0	1.8
Spot 64	293	4350	1.4	21.1876	1.9	0.0752	2.6	0.0116	1.8	0.70	74.1	1.4	73.6	1.9	59.2	44.7	74.1	1.4
Spot 66	356	3794	1.6	22.9670	1.4	0.0697	2.1	0.0116	1.6	0.76	74.5	1.2	68.5	1.4	136.6	34.6	74.5	1.2
Spot 68	2782	35088	3.1	20.9862	0.8	0.0770	2.0	0.0117	1.9	0.93	75.1	1.4	75.3	1.5	81.9	18.2	75.1	1.4
Spot 84	1049	8113	2.2	21.4205	0.9	0.0769	2.1	0.0119	1.9	0.91	76.5	1.5	75.2	1.5	33.1	21.5	76.5	1.5
Spot 90	1606	34316	0.9	20.9968	1.0	0.0785	2.1	0.0120	1.8	0.88	76.6	1.4	76.7	1.5	80.7	23.7	76.6	1.4
Spot 67	819	66981	2.3	20.9416	1.1	0.0787	2.1	0.0120	1.8	0.84	76.6	1.3	77.0	1.5	87.0	26.5	76.6	1.3
Spot 81	1793	61798	1.3	20.8713	0.7	0.0799	2.0	0.0121	1.9	0.93	77.5	1.4	78.0	1.5	95.0	16.8	77.5	1.4
Spot 82	1388	13169	1.2	19.5434	1.0	0.0859	2.5	0.0122	2.4	0.93	78.0	1.8	83.7	2.0	248.4	22.1	78.0	1.8
Spot 89	228	3908	2.8	22.0742	2.3	0.0761	3.1	0.0122	2.1	0.69	78.0	1.6	74.5	2.2	39.4	54.8	78.0	1.6
Spot 70	597	24712	1.4	20.1015	1.0	0.1589	2.0	0.0232	1.8	0.87	147.7	2.6	149.8	2.8	183.2	23.7	147.7	2.6
Spot 69	402	275957	4.6	20.2520	1.2	0.1591	2.5	0.0234	2.1	0.87	148.9	3.2	149.9	3.4	165.8	28.5	148.9	3.2
Spot 65	391	11381	5.1	20.5139	1.3	0.1691	2.2	0.0252	1.8	0.81	160.2	2.8	158.7	3.2	135.7	29.7	160.2	2.8
Spot 60	163	17735	2.5	19.8370	1.7	0.1809	4.4	0.0260	4.0	0.92	165.6	6.6	168.8	6.8	214.0	39.7	165.6	6.6
Spot 67	538	3045	1.3	22.1684	1.8	0.0693	3.2	0.0111	2.6	0.82	71.4	1.9	68.0	2.1	49.7	44.7	71.4	1.9
Spot 56	90	7365	0.7	14.3759	5.1	0.1086	7.0	0.0113	4.8	0.68	72.6	3.4	104.7	7.0	915.4	105.7	72.6	3.4
Spot 47	58	499	0.4	56.8305	15.5	0.0277	16.0	0.0114	3.8	0.24	73.3	2.8	27.8	4.4	3242.2	1230.8	73.3	2.8
Spot 46	646	11658	2.4	20.9141	1.5	0.0759	2.3	0.0115	1.7	0.76	73.8	1.3	74.3	1.6	90.1	35.0	73.8	1.3
Spot 63	2048	106700	1.6	20.4777	0.9	0.0779	2.4	0.0116	2.2	0.93	74.1	1.6	76.1	1.7	139.8	20.6	74.1	1.6
Spot 62	1231	21156	1.6	20.7352	1.3	0.0773	2.5	0.0116	2.2	0.87	74.5	1.6	75.6	1.8	110.4	29.7	74.5	1.6
Spot 50	50	511	2.4	54.9109	37.8	0.0292	38.0	0.0116	3.8	0.10	74.6	2.8	29.3	11.0	3070.0	616.9	74.6	2.8
Spot 48	1191	24810	1.9	20.9791	1.3	0.0766	2.3	0.0117	2.0	0.84	74.7	1.5	74.9	1.7	82.7	30.4	74.7	1.5
Spot 40	1730	28786	1.6	20.8921	1.1	0.0773	2.3	0.0117	2.0	0.87	75.1	1.5	75.6	1.7	92.6	27.1	75.1	1.5

Spot 55	2618	279154	3.1	20.5164	0.8	0.0794	2.3	0.0118	2.2	0.94	75.7	1.6	77.6	1.7	135.4	18.3	75.7	1.6
Spot 66	115	1006	1.0	25.8631	3.7	0.0632	4.9	0.0118	3.1	0.64	75.9	2.4	62.2	2.9	439.4	98.1	75.9	2.4
Spot 44	256	2352	1.1	22.4538	2.3	0.0733	3.4	0.0119	2.6	0.74	76.5	1.9	71.9	2.4	81.0	56.4	76.5	1.9
Spot 45	229	1573	1.2	25.1618	12.0	0.0655	12.3	0.0120	2.5	0.21	76.6	1.9	64.4	7.7	367.6	312.2	76.6	1.9
Spot 58	210	6966	1.4	20.6049	1.8	0.0803	4.2	0.0120	3.8	0.90	76.9	2.9	78.4	3.2	125.3	43.0	76.9	2.9
Spot 70	1126	32162	1.6	21.2647	0.8	0.0785	2.5	0.0121	2.4	0.95	77.6	1.8	76.7	1.9	50.6	19.0	77.6	1.8
Spot 59	429	9658	3.0	20.2368	1.5	0.0848	3.0	0.0125	2.6	0.88	79.8	2.1	82.7	2.4	167.5	33.9	79.8	2.1
Spot 37	1621	113921	1.8	20.5040	1.0	0.1007	2.9	0.0150	2.7	0.94	95.8	2.5	97.4	2.7	136.8	23.5	95.8	2.5
Spot 43	19	502	0.7	44.0536	44.5	0.0641	44.9	0.0205	5.4	0.12	130.6	7.0	63.1	27.4	2115.1	145.8	130.6	7.0
Spot 54	92	2453	0.8	14.2406	6.6	0.2122	8.1	0.0219	4.7	0.58	139.7	6.5	195.4	14.4	934.8	135.3	139.7	6.5
Spot 61	617	11024	1.5	20.8574	1.3	0.1449	2.6	0.0219	2.2	0.86	139.8	3.1	137.4	3.3	96.5	31.5	139.8	3.1
Spot 42	196	70038	1.3	19.0922	1.4	0.1590	2.9	0.0220	2.6	0.87	140.4	3.6	149.9	4.1	301.9	32.5	140.4	3.6
Spot 65	276	3766	4.0	21.5792	1.8	0.1415	3.3	0.0221	2.8	0.84	141.2	3.9	134.4	4.2	15.4	43.1	141.2	3.9
Spot 53	326	3241	1.1	21.8789	1.6	0.1443	2.9	0.0229	2.4	0.83	145.9	3.5	136.8	3.7	17.8	38.9	145.9	3.5
Spot 39	214	3501	1.2	21.3625	1.6	0.1509	3.3	0.0234	2.9	0.88	149.0	4.3	142.7	4.4	39.6	37.8	149.0	4.3
Spot 49	162	3277	1.2	18.3682	2.7	0.1760	3.6	0.0234	2.4	0.67	149.4	3.6	164.6	5.5	389.3	60.9	149.4	3.6
Spot 52	200	3851	0.6	21.4983	1.4	0.1510	2.8	0.0235	2.5	0.88	150.0	3.7	142.8	3.8	24.4	32.7	150.0	3.7
Spot 69	100	3958	1.1	21.0227	2.5	0.1550	3.8	0.0236	2.9	0.76	150.6	4.3	146.3	5.2	77.8	58.7	150.6	4.3
Spot 64	206	3371	2.1	20.9618	4.9	0.1558	5.5	0.0237	2.6	0.48	150.9	3.9	147.0	7.6	84.7	115.7	150.9	3.9
Spot 60	395	93935	3.9	19.7002	1.2	0.1693	3.0	0.0242	2.7	0.91	154.1	4.1	158.8	4.4	230.0	28.6	154.1	4.1
Spot 51	149	4318	0.6	20.8972	1.7	0.1719	3.3	0.0261	2.8	0.86	165.8	4.6	161.1	4.9	92.0	40.1	165.8	4.6
Spot 38	60	3116	0.6	21.3974	3.4	0.1733	4.6	0.0269	3.1	0.68	171.0	5.3	162.2	6.9	35.7	81.2	171.0	5.3
Spot 57	74	30847	0.7	19.9914	2.2	0.1922	3.9	0.0279	3.2	0.82	177.2	5.6	178.5	6.4	196.0	51.6	177.2	5.6
Spot 41	219	45490	1.1	13.2211	0.7	1.9064	2.8	0.1828	2.7	0.97	1082.2	26.9	1083.3	18.6	1085.5	14.1	1085.5	14.1
Spot 36	30	14726	0.8	12.8219	1.1	2.1303	4.3	0.1981	4.1	0.97	1165.1	43.9	1158.7	29.5	1146.6	21.8	1146.6	21.8

LH15GM7

						Isotope ratios					Apparent ages (Ma)							
Analysis	U (ppm)	206Pb 204Pb	U/Th	206Pb* 207Pb*	± (%)	207Pb* 235U*	± (%)	206Pb* 238U	± (%)	error corr.	206Pb* 238U*	± (Ma)	207Pb* 235U	± (Ma)	206Pb* 207Pb*	± (Ma)	Best age (Ma)	± (Ma)
Spot 135	492	9720	2.0	21.0452	1.3	0.0734	2.3	0.0112	1.9	0.82	71.8	1.3	71.9	1.6	75.3	30.6	71.8	1.3
Spot 148	964	14752	2.3	20.9981	0.9	0.0738	2.5	0.0112	2.3	0.93	72.1	1.6	72.3	1.7	80.6	21.6	72.1	1.6
Spot 132	575	138480	2.2	20.7755	1.1	0.0748	2.8	0.0113	2.6	0.91	72.3	1.9	73.3	2.0	105.8	27.2	72.3	1.9
Spot 144	805	7728	2.5	21.0725	1.1	0.0738	1.9	0.0113	1.6	0.82	72.3	1.1	72.3	1.4	72.2	26.6	72.3	1.1
Spot 140	264	1793	1.2	24.5232	1.8	0.0636	2.8	0.0113	2.2	0.78	72.5	1.6	62.6	1.7	301.5	45.0	72.5	1.6
Spot 118	455	3383	2.2	22.1014	5.1	0.0707	5.4	0.0113	1.6	0.30	72.7	1.2	69.4	3.6	42.4	125.1	72.7	1.2
Spot 112	444	6769	2.6	21.1877	2.1	0.0740	3.1	0.0114	2.3	0.75	72.9	1.7	72.5	2.2	59.2	49.1	72.9	1.7
Spot 128	474	10354	2.5	20.4105	1.1	0.0769	2.3	0.0114	2.0	0.87	72.9	1.5	75.2	1.7	147.6	26.4	72.9	1.5
Spot 146	662	16969	1.3	20.6612	1.2	0.0760	2.7	0.0114	2.4	0.89	73.0	1.7	74.3	1.9	118.9	28.6	73.0	1.7
Spot 109	326	5373	1.9	21.2121	2.4	0.0740	3.0	0.0114	1.7	0.59	73.0	1.3	72.5	2.1	56.5	57.2	73.0	1.3
Spot 106	113	3886	1.4	21.4514	3.2	0.0733	4.3	0.0114	2.9	0.68	73.1	2.1	71.9	3.0	29.7	76.4	73.1	2.1
Spot 126c	399	39205	1.6	20.7218	1.7	0.0759	3.1	0.0114	2.6	0.84	73.1	1.9	74.3	2.2	112.0	39.4	73.1	1.9
Spot 141	732	51499	2.4	20.6163	1.2	0.0763	2.2	0.0114	1.8	0.83	73.2	1.3	74.7	1.6	124.0	28.3	73.2	1.3
Spot 138	954	15128	1.4	20.5861	1.0	0.0766	2.3	0.0114	2.1	0.91	73.3	1.5	74.9	1.7	127.5	22.9	73.3	1.5
Spot 133	287	2843	1.0	22.3616	2.9	0.0705	3.5	0.0114	1.9	0.55	73.3	1.4	69.2	2.3	70.9	70.5	73.3	1.4
Spot 124	577	6488	2.6	21.1529	1.4	0.0747	2.5	0.0115	2.1	0.84	73.5	1.5	73.2	1.8	63.1	32.2	73.5	1.5
Spot 150c	236	6314	1.6	20.7320	2.1	0.0764	3.1	0.0115	2.3	0.75	73.6	1.7	74.8	2.2	110.8	48.5	73.6	1.7
Spot 134	809	26939	1.7	19.9597	1.0	0.0794	1.9	0.0115	1.6	0.84	73.7	1.2	77.6	1.4	199.7	23.9	73.7	1.2
Spot 142	154	4491	1.8	20.9732	2.9	0.0756	3.7	0.0115	2.3	0.61	73.7	1.7	74.0	2.6	83.4	69.8	73.7	1.7
Spot 121	672	21764	2.1	21.0955	1.1	0.0752	2.6	0.0115	2.4	0.90	73.8	1.7	73.7	1.9	69.6	27.1	73.8	1.7
Spot 130	225	54152	2.1	20.0051	1.9	0.0797	3.4	0.0116	2.8	0.83	74.1	2.1	77.9	2.6	194.4	45.3	74.1	2.1
Spot 137c	240	49448	1.4	20.9626	1.8	0.0761	3.3	0.0116	2.7	0.83	74.2	2.0	74.5	2.3	84.6	43.6	74.2	2.0
Spot 115	542	8391	2.9	21.3312	1.5	0.0749	2.5	0.0116	2.1	0.82	74.2	1.5	73.3	1.8	43.1	34.7	74.2	1.5
Spot 127	489	64529	1.7	20.8386	1.5	0.0768	2.2	0.0116	1.6	0.73	74.4	1.2	75.1	1.6	98.7	35.7	74.4	1.2

Spot 113	401	7080	3.5	21.1380	1.8	0.0758	2.5	0.0116	1.8	0.70	74.5	1.3	74.2	1.8	64.8	43.1	74.5	1.3
Spot 110	439	49972	2.6	19.8795	1.4	0.0808	2.4	0.0117	1.9	0.81	74.7	1.4	78.9	1.8	209.0	32.8	74.7	1.4
Spot 116	1649	39237	2.2	20.6788	1.0	0.0780	2.5	0.0117	2.3	0.92	75.0	1.7	76.2	1.9	116.9	23.7	75.0	1.7
Spot 107	247	7788	1.0	19.7987	2.2	0.0815	2.7	0.0117	1.6	0.58	75.0	1.2	79.5	2.1	218.5	51.2	75.0	1.2
Spot 145	926	79494	2.4	20.5446	1.2	0.0785	2.6	0.0117	2.3	0.89	75.0	1.7	76.7	1.9	132.2	28.4	75.0	1.7
Spot 149	414	22816	3.0	20.9853	1.6	0.0769	2.7	0.0117	2.2	0.81	75.0	1.6	75.2	2.0	82.0	38.2	75.0	1.6
Spot 117	502	3403	3.0	22.2864	1.8	0.0724	3.5	0.0117	3.0	0.85	75.0	2.2	71.0	2.4	62.7	45.0	75.0	2.2
Spot 101	415	18767	2.4	20.7833	1.4	0.0777	2.4	0.0117	1.9	0.81	75.1	1.4	76.0	1.7	104.9	32.7	75.1	1.4
Spot 123	398	52282	2.0	21.1509	1.3	0.0764	2.6	0.0117	2.2	0.86	75.1	1.7	74.8	1.9	63.3	31.7	75.1	1.7
Spot 114	356	69328	2.5	20.4134	1.1	0.0793	2.5	0.0117	2.2	0.89	75.3	1.6	77.5	1.8	147.2	26.7	75.3	1.6
Spot 103	473	22282	2.1	20.8713	1.1	0.0776	2.3	0.0118	2.0	0.87	75.3	1.5	75.9	1.7	95.0	26.9	75.3	1.5
Spot 104c	225	11301	1.2	20.4502	1.7	0.0792	2.8	0.0118	2.2	0.79	75.3	1.7	77.4	2.1	143.0	40.3	75.3	1.7
Spot 119c	653	10690	0.6	17.0495	2.3	0.0951	3.2	0.0118	2.2	0.69	75.3	1.6	92.2	2.8	554.2	49.5	75.3	1.6
Spot 102	1146	44039	1.1	20.7252	0.8	0.0783	2.1	0.0118	2.0	0.92	75.4	1.5	76.6	1.6	111.6	19.1	75.4	1.5
Spot 143	397	2458	1.3	22.8780	1.6	0.0711	2.5	0.0118	1.9	0.77	75.6	1.4	69.7	1.7	127.0	39.0	75.6	1.4
Spot 136	149	5649	1.3	19.9590	2.4	0.0815	3.5	0.0118	2.5	0.73	75.6	1.9	79.5	2.7	199.8	56.2	75.6	1.9
Spot 122	343	18890	1.8	20.6543	1.4	0.0792	2.5	0.0119	2.1	0.84	76.1	1.6	77.4	1.8	119.6	32.0	76.1	1.6
Spot 105	413	5792	1.3	21.8911	1.5	0.0751	3.1	0.0119	2.7	0.88	76.4	2.1	73.5	2.2	19.2	36.4	76.4	2.1
Spot 129	497	3318	2.2	13.9395	7.1	0.1180	7.6	0.0119	2.9	0.38	76.4	2.2	113.2	8.2	978.5	144.1	76.4	2.2
Spot 139	662	9244	4.7	19.8652	1.9	0.0828	3.0	0.0119	2.3	0.77	76.5	1.7	80.8	2.3	210.7	43.9	76.5	1.7
Spot 108c	175	2295	1.1	22.8451	2.5	0.0723	3.9	0.0120	3.0	0.77	76.8	2.3	70.9	2.6	123.4	61.1	76.8	2.3
Spot 111	195	2682	1.8	22.6844	6.6	0.0730	8.2	0.0120	4.9	0.59	76.9	3.7	71.5	5.7	106.0	163.4	76.9	3.7
Spot 131	200	10255	1.4	20.6673	1.9	0.0802	3.3	0.0120	2.7	0.81	77.0	2.0	78.3	2.5	118.1	45.4	77.0	2.0
Spot 120	299	4901	2.6	21.7350	2.1	0.0762	3.2	0.0120	2.4	0.77	77.0	1.9	74.6	2.3	1.9	49.5	77.0	1.9
Spot 147	66	764	1.2	36.2449	13.4	0.0464	14.0	0.0122	4.0	0.29	78.2	3.1	46.1	6.3	1424.0	439.9	78.2	3.1
Spot 125	88	777	2.0	30.7878	2.7	0.0655	4.0	0.0146	2.9	0.73	93.7	2.7	64.5	2.5	921.3	79.2	93.7	2.7

Floyd

						Isotope ratios					Apparent ages (Ma)							
Analysis	U (ppm)	206Pb 204Pb	U/Th	206Pb* 207Pb*	± (%)	207Pb* 235U*	± (%)	206Pb* 238U	± (%)	error corr.	206Pb* 238U*	± (Ma)	207Pb* 235U	± (Ma)	206Pb* 207Pb*	± (Ma)	Best age (Ma)	± (Ma)
Spot 52	112	1556	0.8	25.4626	6.4	0.0630	7.1	0.0116	3.1	0.43	74.5	2.3	62.0	4.3	398.5	166.3	74.5	2.3
Spot 86	133	1291	0.9	26.1969	3.7	0.0613	4.4	0.0116	2.4	0.55	74.6	1.8	60.4	2.6	473.2	96.9	74.6	1.8
Spot 61	121	2583	1.0	22.7652	3.0	0.0707	4.0	0.0117	2.7	0.67	74.8	2.0	69.3	2.7	114.8	74.0	74.8	2.0
Spot 63	151	2482	0.9	23.1528	2.8	0.0696	3.4	0.0117	2.0	0.59	74.9	1.5	68.4	2.3	156.5	68.4	74.9	1.5
Spot 49	94	947	0.9	29.3183	6.0	0.0552	6.9	0.0117	3.3	0.48	75.2	2.5	54.6	3.6	781.0	170.4	75.2	2.5
Spot 98	82	758	1.0	32.8902	4.6	0.0493	5.5	0.0118	3.1	0.56	75.3	2.3	48.8	2.6	1118.0	139.4	75.3	2.3
Spot 70	80	781	1.0	32.3370	9.5	0.0503	9.9	0.0118	2.8	0.28	75.5	2.1	49.8	4.8	1066.6	285.2	75.5	2.1
Spot 60	137	37705	1.2	19.9347	2.1	0.0817	2.8	0.0118	1.9	0.67	75.7	1.4	79.8	2.2	202.6	48.3	75.7	1.4
Spot 84	434	8806	2.0	21.3193	1.1	0.0766	2.5	0.0118	2.2	0.89	75.9	1.7	75.0	1.8	44.4	26.9	75.9	1.7
Spot 67	104	2918	1.3	22.0014	2.4	0.0743	3.5	0.0119	2.5	0.72	76.0	1.9	72.8	2.5	31.4	59.4	76.0	1.9
Spot 95	142	859	0.7	32.0378	2.7	0.0510	3.6	0.0119	2.3	0.66	76.0	1.8	50.6	1.8	1038.7	79.9	76.0	1.8
Spot 81	78	1203	1.1	24.8128	5.1	0.0660	6.3	0.0119	3.6	0.58	76.1	2.7	64.9	3.9	331.6	132.1	76.1	2.7
Spot 90	287	7803	1.5	20.9618	1.7	0.0781	3.2	0.0119	2.7	0.85	76.1	2.0	76.4	2.3	84.7	39.3	76.1	2.0
Spot 57	304	3698	1.5	21.9033	1.4	0.0748	2.9	0.0119	2.5	0.88	76.1	1.9	73.2	2.0	20.5	32.9	76.1	1.9
Spot 79	164	8245	1.0	20.9293	2.5	0.0784	3.7	0.0119	2.7	0.74	76.3	2.1	76.6	2.7	88.4	59.0	76.3	2.1
Spot 80	97	2415	1.1	24.7846	6.8	0.0663	7.2	0.0119	2.5	0.34	76.4	1.9	65.2	4.6	328.6	174.5	76.4	1.9
Spot 92	97	5504	1.2	21.0493	2.4	0.0784	3.7	0.0120	2.9	0.77	76.7	2.2	76.6	2.8	74.8	56.6	76.7	2.2
Spot 89	113	3119	1.5	23.2207	2.3	0.0712	3.5	0.0120	2.7	0.76	76.8	2.1	69.8	2.4	163.8	57.0	76.8	2.1
Spot 91	170	11347	0.8	21.2592	2.3	0.0778	3.4	0.0120	2.4	0.72	76.9	1.9	76.1	2.5	51.2	55.5	76.9	1.9
Spot 88	85	6185	1.1	21.1197	2.8	0.0783	4.6	0.0120	3.6	0.79	76.9	2.8	76.6	3.4	66.8	67.0	76.9	2.8
Spot 99	110	3433	1.9	22.6294	2.3	0.0731	3.6	0.0120	2.7	0.76	76.9	2.1	71.7	2.5	100.1	57.4	76.9	2.1
Spot 58	217	31437	0.9	20.3316	2.2	0.0815	3.1	0.0120	2.2	0.72	77.0	1.7	79.5	2.4	156.7	50.4	77.0	1.7
Spot 75	330	365724	0.5	20.6922	1.5	0.0801	2.9	0.0120	2.5	0.85	77.0	1.9	78.2	2.2	115.4	35.6	77.0	1.9
Spot 83	86	3312	1.0	22.0422	2.7	0.0754	3.5	0.0120	2.3	0.65	77.2	1.7	73.8	2.5	35.9	64.8	77.2	1.7

Spot 56	263	68838	1.3	16.5946	3.3	0.1005	4.0	0.0121	2.2	0.54	77.5	1.7	97.2	3.7	612.9	72.4	77.5	1.7
Spot 59	238	466909	2.0	19.8782	2.1	0.0840	3.3	0.0121	2.5	0.76	77.6	1.9	81.9	2.6	209.2	49.2	77.6	1.9
Spot 77	53	2735	0.9	23.6235	3.1	0.0707	4.4	0.0121	3.1	0.70	77.7	2.4	69.4	2.9	206.8	78.8	77.7	2.4
Spot 96	135	2335	1.2	23.6036	4.1	0.0708	4.7	0.0121	2.4	0.51	77.7	1.9	69.5	3.2	204.7	102.0	77.7	1.9
Spot 72	129	6351	1.4	21.0670	2.2	0.0794	3.0	0.0121	2.0	0.67	77.7	1.6	77.6	2.3	72.8	53.4	77.7	1.6
Spot 71	98	22372	1.1	20.6978	2.9	0.0809	4.4	0.0121	3.3	0.75	77.8	2.6	79.0	3.4	114.7	69.0	77.8	2.6
Spot 66	83	3251	1.0	22.6849	2.7	0.0738	3.8	0.0121	2.6	0.70	77.8	2.0	72.3	2.6	106.1	66.5	77.8	2.0
Spot 93	73	1769	1.4	25.0061	3.5	0.0670	4.5	0.0122	2.7	0.61	77.9	2.1	65.9	2.8	351.6	91.1	77.9	2.1
Spot 65	103	2896	1.1	22.7148	6.2	0.0739	6.7	0.0122	2.5	0.37	78.0	1.9	72.4	4.6	109.3	152.2	78.0	1.9
Spot 85	172	2836	0.9	22.7197	1.9	0.0739	3.1	0.0122	2.4	0.79	78.0	1.9	72.4	2.2	109.8	46.8	78.0	1.9
Spot 69	207	4591	1.7	22.1428	3.7	0.0758	4.6	0.0122	2.7	0.60	78.0	2.1	74.2	3.3	46.9	89.6	78.0	2.1
Spot 54	91	1862	1.1	24.5003	2.9	0.0686	4.3	0.0122	3.1	0.73	78.1	2.4	67.4	2.8	299.1	74.8	78.1	2.4
Spot 73	382	5861	1.8	21.4991	2.0	0.0783	3.0	0.0122	2.2	0.74	78.2	1.7	76.6	2.2	24.3	48.9	78.2	1.7
Spot 74	128	4019	0.8	20.0767	2.9	0.0839	4.0	0.0122	2.7	0.68	78.3	2.1	81.8	3.1	186.1	68.2	78.3	2.1
Spot 64	131	950	1.0	28.6806	2.7	0.0591	4.3	0.0123	3.4	0.78	78.7	2.6	58.3	2.4	719.2	74.4	78.7	2.6
Spot 82	129	111931	1.1	16.4773	4.2	0.1038	4.9	0.0124	2.7	0.54	79.5	2.1	100.3	4.7	628.2	89.8	79.5	2.1
Spot 97	88	7197	1.1	18.5318	2.8	0.0927	4.0	0.0125	2.9	0.73	79.8	2.3	90.0	3.5	369.4	62.6	79.8	2.3
Spot 62	158	4403	1.0	20.7024	3.4	0.0833	4.3	0.0125	2.5	0.59	80.1	2.0	81.3	3.3	114.2	80.8	80.1	2.0
Spot 55	147	7108	1.2	19.3685	2.0	0.0902	2.9	0.0127	2.1	0.72	81.2	1.7	87.7	2.5	269.0	46.7	81.2	1.7
Spot 87	59	4502	1.1	21.9566	3.7	0.0806	5.1	0.0128	3.5	0.68	82.2	2.9	78.7	3.9	26.4	90.5	82.2	2.9
Spot 78	76	1012	0.9	9.0085	9.6	0.2043	10.2	0.0133	3.4	0.33	85.5	2.9	188.7	17.6	1815.9	175.3	85.5	2.9
Spot 76	417	30739	2.8	20.4926	1.5	0.1129	4.1	0.0168	3.8	0.92	107.3	4.0	108.6	4.2	138.1	36.4	107.3	4.0
Spot 94	24	513	1.2	46.5422	9.0	0.0516	11.0	0.0174	6.4	0.58	111.2	7.1	51.1	5.5	2332.7	365.9	111.2	7.1
Spot 51	289	319	4.0	4.1188	22.4	0.5908	22.7	0.0176	3.7	0.17	112.8	4.2	471.4	85.8	3138.4	360.8	112.8	4.2
Spot 50	170	3565	0.9	20.7640	4.7	0.1294	6.1	0.0195	3.9	0.64	124.5	4.8	123.6	7.1	107.2	110.2	124.5	4.8
Spot 68	154	21101	1.2	19.6677	1.6	0.1583	2.9	0.0226	2.4	0.84	143.9	3.5	149.2	4.0	233.8	36.2	143.9	3.5
Spot 100c	45	5627	0.6	20.0049	2.7	0.1702	4.8	0.0247	3.9	0.82	157.2	6.1	159.6	7.0	194.4	62.9	157.2	6.1
Spot 53	104	47014	0.7	19.9275	2.2	0.1730	3.8	0.0250	3.1	0.82	159.2	4.8	162.0	5.6	203.4	50.2	159.2	4.8

Calvin

						Isotope ratios					Apparent ages (Ma)							
Analysis	U (ppm)	206Pb 204Pb	U/Th	206Pb* 207Pb*	± (%)	207Pb* 235U*	± (%)	206Pb* 238U	± (%)	error corr.	206Pb* 238U*	± (Ma)	207Pb* 235U	± (Ma)	206Pb* 207Pb*	± (Ma)	Best age (Ma)	± (Ma)
Spot 3	128	1267	1.4	26.2864	2.8	0.0598	4.2	0.0114	3.2	0.75	73.1	2.3	59.0	2.4	482.2	74.2	73.1	2.3
Spot 57	133	991	1.3	28.1790	5.9	0.0559	6.4	0.0114	2.5	0.39	73.2	1.8	55.2	3.5	670.3	163.6	73.2	1.8
Spot 34	212	18523	1.2	21.1431	1.9	0.0748	2.8	0.0115	2.1	0.74	73.6	1.5	73.3	2.0	64.3	45.4	73.6	1.5
Spot 42	125	882	1.4	29.4586	4.0	0.0538	4.5	0.0115	2.1	0.46	73.6	1.5	53.2	2.3	794.5	113.0	73.6	1.5
Spot 33	138	4534	1.3	22.2766	2.0	0.0712	2.9	0.0115	2.0	0.71	73.7	1.5	69.8	1.9	61.6	49.4	73.7	1.5
Spot 48	147	3969	1.7	22.9696	4.5	0.0694	5.0	0.0116	2.1	0.42	74.1	1.5	68.1	3.3	136.9	111.5	74.1	1.5
Spot 44	304	7782	1.0	21.1467	2.1	0.0754	2.9	0.0116	2.0	0.69	74.1	1.5	73.8	2.0	63.8	49.3	74.1	1.5
Spot 64	215	2841	1.0	23.3732	2.2	0.0683	2.8	0.0116	1.9	0.65	74.2	1.4	67.0	1.8	180.1	54.0	74.2	1.4
Spot 46	123	2151	1.2	23.9370	3.8	0.0668	5.1	0.0116	3.5	0.68	74.3	2.6	65.6	3.3	240.0	95.6	74.3	2.6
Spot 29	157	27498	1.9	21.3572	2.5	0.0749	3.4	0.0116	2.4	0.69	74.4	1.8	73.3	2.4	40.2	59.5	74.4	1.8
Spot 22	190	11821	1.3	21.0033	2.0	0.0762	2.8	0.0116	1.9	0.69	74.4	1.4	74.6	2.0	80.0	47.9	74.4	1.4
Spot 36	215	2926	1.1	22.8552	1.5	0.0701	2.4	0.0116	1.9	0.79	74.4	1.4	68.8	1.6	124.5	36.2	74.4	1.4
Spot 7	153	1664	2.1	25.6638	4.1	0.0625	4.5	0.0116	1.7	0.37	74.5	1.2	61.5	2.7	419.1	108.4	74.5	1.2
Spot 40	171	1959	1.0	24.6312	3.0	0.0652	3.8	0.0116	2.4	0.64	74.6	1.8	64.1	2.4	312.7	76.1	74.6	1.8
Spot 63	141	15466	1.2	21.0148	2.0	0.0764	3.5	0.0116	2.9	0.82	74.7	2.1	74.8	2.5	78.7	48.2	74.7	2.1
Spot 65	130	3520	1.3	20.9222	2.4	0.0768	3.2	0.0117	2.1	0.65	74.7	1.6	75.1	2.3	89.2	57.8	74.7	1.6
Spot 50	135	5413	1.5	21.4675	2.2	0.0749	3.1	0.0117	2.3	0.72	74.7	1.7	73.3	2.2	27.9	52.0	74.7	1.7
Spot 17	122	1991	1.7	25.6215	2.6	0.0627	3.8	0.0117	2.8	0.74	74.7	2.1	61.8	2.3	414.8	67.4	74.7	2.1
Spot 31	162	1864	1.3	24.8446	3.1	0.0648	3.8	0.0117	2.3	0.60	74.8	1.7	63.7	2.4	334.9	78.6	74.8	1.7
Spot 21	180	1958	1.0	25.0376	5.5	0.0643	6.0	0.0117	2.4	0.40	74.9	1.8	63.3	3.7	354.8	142.0	74.9	1.8
Spot 38	136	89909	1.6	20.5767	1.9	0.0784	3.2	0.0117	2.5	0.80	75.0	1.9	76.7	2.3	128.5	45.1	75.0	1.9
Spot 45	142	4334	1.3	22.3514	2.3	0.0723	3.2	0.0117	2.3	0.71	75.1	1.7	70.9	2.2	69.8	55.4	75.1	1.7
Spot 55	185	50475	2.5	20.5361	2.1	0.0787	2.8	0.0117	1.8	0.65	75.1	1.3	76.9	2.0	133.1	49.3	75.1	1.3

Spot 43	117	2224	1.4	24.4566	4.8	0.0662	5.2	0.0117	2.2	0.43	75.2	1.7	65.0	3.3	294.5	121.4	75.2	1.7
Spot 9	312	6860	2.5	22.2521	2.8	0.0728	3.6	0.0117	2.3	0.63	75.3	1.7	71.3	2.5	58.9	68.9	75.3	1.7
Spot 52	161	19788	0.9	16.7015	3.8	0.0970	4.3	0.0117	2.1	0.48	75.3	1.5	94.0	3.9	599.0	82.2	75.3	1.5
Spot 62	156	136562	0.9	18.2755	2.2	0.0887	3.4	0.0118	2.6	0.76	75.3	1.9	86.3	2.8	400.7	49.7	75.3	1.9
Spot 19	134	6188	1.1	21.4944	2.2	0.0754	3.2	0.0118	2.2	0.70	75.4	1.7	73.8	2.3	24.8	53.8	75.4	1.7
Spot 37	179	1862	1.1	24.8878	4.3	0.0652	4.8	0.0118	2.2	0.45	75.4	1.6	64.1	3.0	339.3	111.8	75.4	1.6
Spot 6	193	3369	1.1	23.0131	2.7	0.0705	3.7	0.0118	2.5	0.68	75.4	1.9	69.2	2.5	141.5	67.2	75.4	1.9
Spot 51	124	3531	1.4	20.7689	3.0	0.0783	3.7	0.0118	2.3	0.61	75.6	1.7	76.5	2.8	106.6	70.5	75.6	1.7
Spot 35	175	4952	1.1	21.4994	1.8	0.0757	2.7	0.0118	2.0	0.74	75.6	1.5	74.1	1.9	24.3	43.8	75.6	1.5
Spot 16	147	2262	1.4	23.3301	4.6	0.0697	5.1	0.0118	2.2	0.43	75.6	1.6	68.5	3.3	175.5	114.1	75.6	1.6
Spot 61	107	4318	1.6	22.5097	3.0	0.0724	4.1	0.0118	2.8	0.69	75.8	2.1	71.0	2.8	87.0	73.4	75.8	2.1
Spot 18	151	4284	1.5	20.8435	2.7	0.0782	3.5	0.0118	2.2	0.63	75.8	1.6	76.5	2.6	98.1	64.2	75.8	1.6
Spot 39	137	6660	1.4	21.9168	3.0	0.0744	3.6	0.0118	2.0	0.56	75.8	1.5	72.9	2.6	22.0	72.9	75.8	1.5
Spot 53	156	10576	1.3	19.9881	2.3	0.0817	3.5	0.0118	2.7	0.77	75.9	2.0	79.7	2.7	196.4	52.3	75.9	2.0
Spot 11	136	1631	2.4	25.6014	12.1	0.0638	12.4	0.0118	2.7	0.22	75.9	2.0	62.8	7.6	412.7	318.6	75.9	2.0
Spot 28	195	2206	1.1	24.4227	2.5	0.0669	3.7	0.0118	2.6	0.72	75.9	2.0	65.8	2.3	291.0	64.5	75.9	2.0
Spot 5	114	23726	1.5	20.5093	2.8	0.0797	3.9	0.0119	2.7	0.70	76.0	2.0	77.8	2.9	136.2	65.4	76.0	2.0
Spot 25	145	10054	1.4	21.1905	2.0	0.0772	2.8	0.0119	2.1	0.72	76.0	1.6	75.5	2.1	58.9	46.7	76.0	1.6
Spot 26	144	9341	1.0	17.2393	4.0	0.0949	4.5	0.0119	2.2	0.48	76.1	1.6	92.1	4.0	530.0	87.0	76.1	1.6
Spot 24	204	15095	1.2	21.4306	1.7	0.0765	2.5	0.0119	1.8	0.72	76.2	1.4	74.8	1.8	31.9	41.2	76.2	1.4
Spot 14	172	3579	0.9	20.6002	2.8	0.0797	3.6	0.0119	2.2	0.61	76.3	1.7	77.9	2.7	125.8	66.3	76.3	1.7
Spot 2	174	2549	1.0	24.2010	3.5	0.0679	4.3	0.0119	2.5	0.59	76.4	1.9	66.7	2.8	267.8	87.8	76.4	1.9
Spot 27	175	1410	0.9	17.7331	5.3	0.0928	5.8	0.0119	2.3	0.40	76.5	1.8	90.1	5.0	467.8	117.1	76.5	1.8
Spot 32	148	8190	1.0	21.6174	2.3	0.0761	3.4	0.0119	2.5	0.74	76.5	1.9	74.5	2.4	11.1	54.8	76.5	1.9
Spot 15	127	3948	1.6	22.7858	2.1	0.0722	3.1	0.0119	2.2	0.71	76.5	1.7	70.8	2.1	117.0	52.8	76.5	1.7
Spot 54	145	6950	1.2	21.4737	2.5	0.0767	4.6	0.0119	3.9	0.84	76.5	3.0	75.0	3.3	27.1	59.6	76.5	3.0
Spot 30	147	3250	1.9	21.8126	2.0	0.0758	2.8	0.0120	2.0	0.70	76.9	1.5	74.2	2.0	10.5	49.2	76.9	1.5
Spot 1	170	11597	1.3	22.0175	2.0	0.0755	3.0	0.0121	2.3	0.76	77.3	1.8	73.9	2.2	33.1	48.4	77.3	1.8
Spot 20	131	14866	1.3	20.7056	3.0	0.0806	3.6	0.0121	2.0	0.55	77.6	1.5	78.7	2.7	113.8	70.9	77.6	1.5

Spot 8	139	30487	1.4	20.4521	2.2	0.0817	3.7	0.0121	2.9	0.79	77.7	2.2	79.8	2.8	142.8	52.7	77.7	2.2
Spot 13	170	7355	1.3	22.5843	2.3	0.0743	3.8	0.0122	3.1	0.80	78.0	2.4	72.8	2.7	95.2	55.3	78.0	2.4
Spot 23	126	2223	2.0	24.1709	8.4	0.0695	8.9	0.0122	2.8	0.31	78.0	2.2	68.2	5.9	264.6	214.2	78.0	2.2
Spot 12	175	24890	1.2	12.2233	7.3	0.1380	7.7	0.0122	2.4	0.31	78.4	1.8	131.3	9.5	1241.0	144.0	78.4	1.8
Spot 41	145	8477	1.1	16.9446	2.9	0.0997	3.6	0.0122	2.1	0.60	78.5	1.7	96.5	3.3	567.7	62.6	78.5	1.7
Spot 10	126	2439	1.1	23.3352	2.2	0.0747	4.0	0.0126	3.4	0.83	81.0	2.7	73.2	2.9	176.1	56.0	81.0	2.7
Spot 47	165	915	1.4	9.6657	17.1	0.1812	18.8	0.0127	7.8	0.42	81.4	6.3	169.1	29.3	1687.0	317.8	81.4	6.3
Spot 4	147	11246	1.6	20.4341	1.5	0.1025	3.9	0.0152	3.5	0.92	97.2	3.4	99.1	3.6	144.8	35.4	97.2	3.4

Yoshi

						Isotope ratios					Apparent ages (Ma)							
Analysis	**U (ppm)**	**206Pb 204Pb**	**U/Th**	**206Pb* 207Pb***	**± (%)**	**207Pb* 235U***	**± (%)**	**206Pb* 238U**	**± (%)**	**error corr.**	**206Pb* 238U***	**± (Ma)**	**207Pb* 235U**	**± (Ma)**	**206Pb* 207Pb***	**± (Ma)**	**Best age (Ma)**	**± (Ma)**
Spot 18	245	2379	0.6	24.0099	7.9	0.0660	8.3	0.0115	2.5	0.30	73.6	1.9	64.9	5.2	247.7	200.7	73.6	1.9
Spot 20	229	8724	0.9	20.8926	1.9	0.0778	3.3	0.0118	2.7	0.82	75.6	2.0	76.1	2.4	92.5	43.9	75.6	2.0
Spot 26	140	2410	0.7	23.4612	2.9	0.0695	4.6	0.0118	3.6	0.78	75.8	2.7	68.2	3.1	189.5	72.3	75.8	2.7
Spot 49	176	1821	0.6	24.2742	4.8	0.0674	5.6	0.0119	2.8	0.51	76.1	2.1	66.3	3.6	275.4	122.5	76.1	2.1
Spot 48	123	2719	1.0	22.2079	5.6	0.0742	6.3	0.0120	2.8	0.44	76.6	2.1	72.7	4.4	54.1	137.4	76.6	2.1
Spot 9	291	2496	0.8	23.4071	7.2	0.0705	7.7	0.0120	2.9	0.37	76.7	2.2	69.2	5.2	183.8	179.5	76.7	2.2
Spot 46	327	4142	0.8	22.5185	1.5	0.0733	2.9	0.0120	2.5	0.85	76.7	1.9	71.8	2.0	88.0	36.9	76.7	1.9
Spot 36	162	6366	1.0	21.7783	2.4	0.0759	3.8	0.0120	2.9	0.77	76.8	2.2	74.3	2.7	6.7	57.7	76.8	2.2
Spot 11	185	2406	0.8	23.7247	5.7	0.0697	6.4	0.0120	2.7	0.43	76.9	2.1	68.4	4.2	217.5	144.5	76.9	2.1
Spot 43c	385	11969	0.9	21.5553	1.9	0.0767	3.4	0.0120	2.8	0.83	76.9	2.2	75.1	2.5	18.0	46.0	76.9	2.2
Spot 2	197	23196	0.9	20.1792	2.2	0.0820	3.7	0.0120	3.0	0.80	76.9	2.3	80.0	2.9	174.2	52.0	76.9	2.3
Spot 27	205	1604	1.0	25.4516	1.7	0.0652	2.9	0.0120	2.4	0.82	77.1	1.8	64.1	1.8	397.4	43.9	77.1	1.8
Spot 52c	42	3508	0.8	24.3938	3.9	0.0681	5.1	0.0120	3.3	0.64	77.2	2.5	66.9	3.3	288.0	98.8	77.2	2.5

Spot 54c	136	10227	0.9	20.7440	2.3	0.0801	4.0	0.0121	3.3	0.83	77.3	2.6	78.3	3.0	109.4	53.7	77.3	2.6
Spot 40	140	899	0.8	30.3736	2.7	0.0549	4.0	0.0121	2.9	0.72	77.5	2.2	54.3	2.1	882.0	78.7	77.5	2.2
Spot 33	122	1810	0.8	24.8690	10.8	0.0671	11.2	0.0121	3.0	0.27	77.5	2.3	65.9	7.1	337.4	278.8	77.5	2.3
Spot 32	175	1877	1.0	25.0149	2.5	0.0667	4.0	0.0121	3.1	0.78	77.6	2.4	65.6	2.5	352.5	64.0	77.6	2.4
Spot 28	147	10180	1.0	21.3501	2.7	0.0783	4.0	0.0121	3.0	0.74	77.6	2.3	76.5	3.0	41.0	64.2	77.6	2.3
Spot 55c	409	2883	0.6	24.0635	2.0	0.0694	5.1	0.0121	4.7	0.92	77.6	3.7	68.2	3.4	253.3	50.2	77.6	3.7
Spot 47	176	2835	0.9	21.4866	5.0	0.0778	5.7	0.0121	2.6	0.46	77.6	2.0	76.0	4.2	25.7	121.1	77.6	2.0
Spot 31	137	3123	0.7	21.7860	3.7	0.0769	4.8	0.0122	3.1	0.64	77.9	2.4	75.2	3.5	7.6	90.0	77.9	2.4
Spot 39	218	5621	0.8	21.6659	2.1	0.0774	3.3	0.0122	2.6	0.78	77.9	2.0	75.7	2.4	5.7	49.8	77.9	2.0
Spot 1	118	1638	1.0	25.9114	2.7	0.0647	3.7	0.0122	2.5	0.69	78.0	2.0	63.7	2.3	444.3	70.8	78.0	2.0
Spot 8	239	14792	0.8	21.7170	1.8	0.0772	3.0	0.0122	2.4	0.79	78.0	1.8	75.6	2.2	0.1	44.1	78.0	1.8
Spot 59c	92	659	0.6	42.8393	5.8	0.0392	6.3	0.0122	2.4	0.39	78.1	1.9	39.1	2.4	2008.7	219.0	78.1	1.9
Spot 58c	142	6080	0.8	21.5242	2.3	0.0782	3.2	0.0122	2.3	0.71	78.3	1.8	76.5	2.4	21.5	54.3	78.3	1.8
Spot 21	190	8417	1.0	21.3029	2.6	0.0791	3.8	0.0122	2.7	0.73	78.3	2.1	77.3	2.8	46.3	61.2	78.3	2.1
Spot 6	206	3822	1.1	22.3876	3.4	0.0753	4.5	0.0122	3.1	0.68	78.3	2.4	73.7	3.2	73.7	82.0	78.3	2.4
Spot 19	114	2163	0.9	24.9645	6.7	0.0677	7.3	0.0123	2.9	0.39	78.5	2.2	66.5	4.7	347.3	174.2	78.5	2.2
Spot 45	152	2662	1.0	23.4262	2.3	0.0721	3.4	0.0123	2.6	0.75	78.5	2.0	70.7	2.3	185.8	56.6	78.5	2.0
Spot 7	100	810	1.3	31.9862	4.9	0.0528	5.8	0.0123	3.0	0.52	78.5	2.3	52.3	2.9	1033.9	147.3	78.5	2.3
Spot 63c	152	1274	0.7	20.7027	5.9	0.0816	6.6	0.0123	2.9	0.45	78.5	2.3	79.7	5.1	114.1	139.2	78.5	2.3
Spot 4	213	16389	0.8	20.9256	2.2	0.0808	3.6	0.0123	2.9	0.79	78.6	2.2	78.9	2.8	88.8	52.9	78.6	2.2
Spot 29	62	2170	1.1	22.7958	3.5	0.0742	5.9	0.0123	4.8	0.81	78.6	3.8	72.7	4.2	118.1	85.4	78.6	3.8
Spot 14	235	10601	1.3	22.4439	1.7	0.0754	2.9	0.0123	2.4	0.81	78.6	1.9	73.8	2.1	79.9	41.8	78.6	1.9
Spot 22	92	4082	1.0	22.7494	2.8	0.0746	4.2	0.0123	3.1	0.74	78.9	2.4	73.1	2.9	113.1	68.8	78.9	2.4
Spot 16	129	2379	0.9	21.2907	3.0	0.0798	4.4	0.0123	3.2	0.74	79.0	2.5	78.0	3.3	47.6	70.6	79.0	2.5
Spot 37	169	3977	0.8	21.7692	2.1	0.0782	3.3	0.0123	2.6	0.79	79.1	2.1	76.4	2.5	5.7	49.8	79.1	2.1
Spot 62c	302	6094	0.5	21.6643	1.7	0.0785	2.9	0.0123	2.3	0.81	79.1	1.8	76.8	2.1	5.9	40.3	79.1	1.8
Spot 5	76	7642	0.8	20.6445	3.4	0.0825	4.4	0.0124	2.8	0.64	79.1	2.2	80.5	3.4	120.7	79.0	79.1	2.2
Spot 17	166	2770	0.9	23.1355	3.5	0.0737	4.3	0.0124	2.5	0.58	79.2	2.0	72.2	3.0	154.7	87.2	79.2	2.0
Spot 53c	138	1891	0.7	24.1576	2.2	0.0706	3.5	0.0124	2.8	0.79	79.2	2.2	69.3	2.3	263.2	54.6	79.2	2.2

Spot 12	120	11837	1.0	20.9293	2.3	0.0815	3.7	0.0124	3.0	0.80	79.3	2.3	79.6	2.9	88.4	53.7	79.3	2.3
Spot 61	117	1506	0.8	25.3430	9.4	0.0677	9.9	0.0124	3.1	0.31	79.8	2.5	66.5	6.3	386.2	243.7	79.8	2.5
Spot 24	191	11203	0.8	21.8111	1.5	0.0788	3.1	0.0125	2.7	0.87	79.8	2.2	77.0	2.3	10.3	37.0	79.8	2.2
Spot 15	175	4089	1.0	21.5310	1.7	0.0799	3.5	0.0125	3.0	0.87	79.9	2.4	78.0	2.6	20.8	41.9	79.9	2.4
Spot 10	175	3671	0.9	21.3940	1.8	0.0804	3.6	0.0125	3.1	0.86	79.9	2.4	78.5	2.7	36.0	43.0	79.9	2.4
Spot 3	103	2742	0.9	23.3018	4.9	0.0739	5.5	0.0125	2.4	0.45	80.0	1.9	72.4	3.8	172.5	122.1	80.0	1.9
Spot 42	210	4169	0.9	22.6207	2.4	0.0763	3.7	0.0125	2.8	0.76	80.2	2.3	74.6	2.7	99.1	59.7	80.2	2.3
Spot 23	137	22758	0.8	20.0174	2.3	0.0868	3.8	0.0126	3.0	0.79	80.7	2.4	84.5	3.1	193.0	53.2	80.7	2.4
Spot 41	159	4034	1.1	20.5228	2.2	0.0847	3.8	0.0126	3.1	0.81	80.8	2.5	82.5	3.0	134.7	51.2	80.8	2.5
Spot 25	183	21521	0.8	19.5120	1.8	0.0892	3.6	0.0126	3.1	0.86	80.9	2.5	86.7	3.0	252.1	42.3	80.9	2.5
Spot 34	121	64132	1.1	20.2470	2.4	0.0860	3.5	0.0126	2.5	0.72	80.9	2.0	83.8	2.8	166.4	56.4	80.9	2.0
Spot 51	343	6255	1.1	22.0465	1.7	0.0791	2.9	0.0126	2.3	0.82	81.0	1.9	77.3	2.1	36.3	40.1	81.0	1.9
Spot 35	491	8649	0.7	21.1306	1.3	0.0832	2.4	0.0128	2.0	0.83	81.7	1.6	81.2	1.8	65.6	30.9	81.7	1.6
Spot 50	217	1803	0.8	23.3644	1.7	0.0762	3.4	0.0129	2.9	0.86	82.7	2.4	74.5	2.5	179.2	43.3	82.7	2.4
Spot 44	99	1688	1.0	24.7437	6.3	0.0727	7.0	0.0131	3.2	0.45	83.6	2.6	71.3	4.8	324.4	160.8	83.6	2.6
Spot 38	172	14919	1.0	20.5909	2.4	0.0883	3.3	0.0132	2.3	0.68	84.5	1.9	86.0	2.7	126.9	57.3	84.5	1.9
Spot 13	282	10651	1.3	20.2074	1.7	0.1107	2.9	0.0162	2.3	0.80	103.7	2.4	106.6	2.9	170.9	39.9	103.7	2.4
Spot 57c	170	6169	1.5	21.6123	2.2	0.1150	5.4	0.0180	4.9	0.91	115.1	5.6	110.5	5.6	11.7	53.0	115.1	5.6
Spot 56c	37	1081	0.4	24.8884	3.4	0.1357	6.4	0.0245	5.5	0.85	156.0	8.4	129.2	7.8	339.4	87.0	156.0	8.4

Murdock

						Isotope ratios					Apparent ages (Ma)							
Analysis	U (ppm)	206Pb 204Pb	U/Th	206Pb* 207Pb*	± (%)	207Pb* 235U*	± (%)	206Pb* 238U	± (%)	error corr.	206Pb* 238U*	± (Ma)	207Pb* 235U	± (Ma)	206Pb* 207Pb*	± (Ma)	Best age (Ma)	± (Ma)
Spot 129	657	40665	0.8	19.6016	1.0	0.1411	2.2	0.0201	1.9	0.88	128.0	2.4	134.0	2.7	241.6	23.3	128.0	2.4
Spot 126	4406	11057	0.0	18.1215	0.9	0.1814	2.3	0.0238	2.1	0.92	151.9	3.1	169.3	3.5	419.6	20.2	151.9	3.1
Spot 107	385	15823	2.7	20.4092	1.3	0.1637	2.5	0.0242	2.1	0.85	154.4	3.2	154.0	3.5	147.7	30.8	154.4	3.2
Spot 99	530	28703	1.6	20.4588	1.1	0.1635	2.5	0.0243	2.2	0.90	154.5	3.4	153.8	3.6	142.0	26.2	154.5	3.4
Spot 137	305	26964	0.8	20.3839	1.3	0.1647	2.3	0.0243	1.9	0.83	155.1	3.0	154.8	3.3	150.6	29.9	155.1	3.0
Spot 138	2126	188289	1.1	20.1539	0.6	0.1670	1.6	0.0244	1.4	0.92	155.5	2.2	156.8	2.3	177.1	14.3	155.5	2.2
Spot 78c	113	1867	0.8	22.6678	6.9	0.1491	7.2	0.0245	2.3	0.31	156.1	3.5	141.1	9.5	104.2	168.8	156.1	3.5
Spot 120	284	33913	1.0	20.2629	1.2	0.1669	2.4	0.0245	2.0	0.86	156.2	3.1	156.7	3.4	164.5	27.7	156.2	3.1
Spot 116	913	35108	1.2	20.0391	0.9	0.1690	2.0	0.0246	1.8	0.89	156.4	2.8	158.6	3.0	190.5	21.2	156.4	2.8
Spot 112	1970	39389	0.4	20.3026	0.9	0.1670	2.3	0.0246	2.1	0.92	156.6	3.3	156.8	3.3	160.0	20.6	156.6	3.3
Spot 110	1102	112176	1.1	19.9726	0.8	0.1698	2.2	0.0246	2.1	0.94	156.6	3.3	159.2	3.3	198.2	18.1	156.6	3.3
Spot 114	487	26412	0.6	20.2507	1.3	0.1678	3.0	0.0246	2.7	0.90	156.9	4.1	157.5	4.3	165.9	29.8	156.9	4.1
Spot 136	2781	98811	0.5	20.1689	0.8	0.1685	2.0	0.0246	1.8	0.91	157.0	2.8	158.1	2.9	175.4	19.5	157.0	2.8
Spot 131	1901	70417	0.5	20.2883	0.8	0.1687	2.4	0.0248	2.3	0.94	158.1	3.6	158.3	3.6	161.6	18.8	158.1	3.6
Spot 125	249	25178	1.1	18.8325	2.7	0.1818	3.8	0.0248	2.7	0.70	158.1	4.2	169.6	6.0	333.1	61.5	158.1	4.2
Spot 72	3345	72493	0.6	19.8176	0.7	0.1729	2.0	0.0249	1.9	0.94	158.3	3.0	162.0	3.1	216.3	16.5	158.3	3.0
Spot 122	300	16018	1.3	20.3917	1.0	0.1681	2.5	0.0249	2.3	0.92	158.3	3.5	157.8	3.6	149.7	23.0	158.3	3.5
Spot 123	857	77554	1.0	19.9248	0.8	0.1722	2.4	0.0249	2.2	0.94	158.4	3.5	161.3	3.5	203.7	19.3	158.4	3.5
Spot 130	1062	24534	1.0	20.1792	0.8	0.1701	2.1	0.0249	1.9	0.91	158.5	3.0	159.5	3.1	174.2	19.8	158.5	3.0
Spot 101c	185	2766	0.6	22.9789	1.5	0.1494	3.0	0.0249	2.7	0.88	158.6	4.2	141.4	4.0	137.9	36.3	158.6	4.2
Spot 119	388	7434	0.9	20.9240	1.1	0.1642	2.6	0.0249	2.4	0.91	158.6	3.8	154.4	3.8	89.0	25.6	158.6	3.8
Spot 133	1211	174983	1.6	20.1342	0.9	0.1707	2.5	0.0249	2.3	0.93	158.7	3.6	160.0	3.6	179.4	21.5	158.7	3.6
Spot 135	311	4247	0.8	21.2900	1.9	0.1616	3.4	0.0249	2.8	0.82	158.8	4.4	152.1	4.8	47.7	46.4	158.8	4.4
Spot 109	1484	50125	0.6	20.3316	0.8	0.1693	1.9	0.0250	1.7	0.90	158.9	2.7	158.8	2.8	156.7	19.9	158.9	2.7

Spot 105	426	16849	0.7	20.3901	1.1	0.1690	2.5	0.0250	2.3	0.90	159.1	3.6	158.5	3.7	149.9	25.0	159.1	3.6
Spot 124	448	13869	0.6	20.2445	1.0	0.1702	2.6	0.0250	2.3	0.91	159.1	3.7	159.6	3.8	166.6	24.5	159.1	3.7
Spot 128	576	150184	1.1	19.8448	1.1	0.1738	2.3	0.0250	2.0	0.88	159.3	3.2	162.7	3.5	213.0	25.5	159.3	3.2
Spot 91	319	12759	1.0	20.3618	1.5	0.1694	2.6	0.0250	2.1	0.83	159.3	3.4	158.9	3.8	153.2	34.0	159.3	3.4
Spot 139	468	6215	0.7	20.8858	1.2	0.1652	2.7	0.0250	2.4	0.90	159.3	3.8	155.3	3.9	93.3	28.2	159.3	3.8
Spot 113	2147	240963	0.6	20.3714	0.8	0.1696	1.8	0.0251	1.6	0.89	159.5	2.6	159.0	2.7	152.0	19.5	159.5	2.6
Spot 108	3990	42485	0.5	20.0321	0.6	0.1725	2.0	0.0251	1.9	0.96	159.6	3.0	161.6	2.9	191.3	13.0	159.6	3.0
Spot 98	2520	8758	1.5	18.1447	1.2	0.1907	2.5	0.0251	2.1	0.86	159.8	3.4	177.2	4.0	416.8	27.9	159.8	3.4
Spot 121	746	11836	0.7	20.6145	1.0	0.1682	1.9	0.0251	1.6	0.84	160.1	2.6	157.8	2.8	124.2	24.6	160.1	2.6
Spot 77	362	7563	0.8	20.6601	2.2	0.1685	3.0	0.0252	2.1	0.70	160.7	3.4	158.1	4.5	119.0	51.0	160.7	3.4
Spot 96c	191	7483	0.6	20.9019	2.5	0.1667	3.3	0.0253	2.1	0.66	160.9	3.4	156.5	4.7	91.5	58.5	160.9	3.4
Spot 140c	984	150465	0.8	19.9535	0.8	0.1751	2.3	0.0253	2.1	0.94	161.3	3.4	163.8	3.4	200.4	18.3	161.3	3.4
Spot 93	151	19472	0.8	20.7172	1.2	0.1694	2.6	0.0255	2.3	0.89	162.0	3.7	158.9	3.9	112.5	28.3	162.0	3.7
Spot 94	660	33572	1.0	20.2858	1.0	0.1734	2.3	0.0255	2.1	0.89	162.4	3.3	162.4	3.5	161.9	24.3	162.4	3.3
Spot 106	185	13699	1.0	19.8601	1.7	0.1773	3.0	0.0255	2.6	0.84	162.5	4.1	165.7	4.6	211.3	38.3	162.5	4.1
Spot 75	482	16155	0.6	20.6929	1.2	0.1704	2.7	0.0256	2.4	0.89	162.8	3.8	159.8	3.9	115.3	28.3	162.8	3.8
Spot 115	595	1328556	1.1	19.6764	1.0	0.1795	2.4	0.0256	2.2	0.91	163.0	3.5	167.6	3.6	232.8	22.2	163.0	3.5
Spot 74	1655	47006	1.0	19.8239	0.9	0.1784	2.1	0.0256	1.9	0.91	163.2	3.1	166.7	3.3	215.5	19.9	163.2	3.1
Spot 104	682	16711	0.7	20.2633	0.8	0.1746	2.2	0.0257	2.1	0.93	163.3	3.4	163.4	3.4	164.5	18.6	163.3	3.4
Spot 92	452	17962	0.7	20.4423	1.1	0.1731	2.7	0.0257	2.5	0.91	163.4	4.0	162.1	4.0	143.9	25.6	163.4	4.0
Spot 127	695	170468	2.3	18.9256	1.1	0.1870	2.4	0.0257	2.1	0.88	163.4	3.3	174.1	3.8	321.9	25.4	163.4	3.3
Spot 134	2238	74610	0.5	20.1207	0.7	0.1773	1.8	0.0259	1.7	0.93	164.7	2.8	165.8	2.8	181.0	15.8	164.7	2.8
Spot 132	431	14567	0.8	20.7356	1.1	0.1723	2.6	0.0259	2.4	0.90	164.9	3.9	161.4	3.9	110.4	26.5	164.9	3.9
Spot 102	551	80551	1.2	20.1157	0.8	0.1787	2.8	0.0261	2.7	0.96	165.9	4.4	167.0	4.3	181.5	18.7	165.9	4.4
Spot 103	310	16635	1.1	20.5743	1.3	0.1768	2.5	0.0264	2.2	0.85	167.8	3.6	165.3	3.9	128.8	31.6	167.8	3.6
Spot 76	576	13537	1.4	20.5279	1.1	0.1773	2.6	0.0264	2.4	0.91	168.0	4.0	165.7	4.0	134.1	25.6	168.0	4.0
Spot 111	350	78687	1.3	19.9638	1.4	0.1825	2.3	0.0264	1.8	0.80	168.1	3.0	170.2	3.6	199.2	31.6	168.1	3.0
Spot 97	882	101488	1.3	20.3379	0.9	0.1804	2.5	0.0266	2.3	0.94	169.3	3.9	168.4	3.9	155.9	20.7	169.3	3.9
Spot 95	728	89476	1.4	20.2694	0.9	0.1829	3.4	0.0269	3.3	0.97	171.0	5.5	170.6	5.3	163.8	20.1	171.0	5.5

Spot 100	495	11911	1.1	20.4789	1.0	0.1813	2.3	0.0269	2.1	0.90	171.3	3.6	169.2	3.7	139.7	24.0	171.3	3.6
Spot 73	301	4955	1.2	21.4492	1.6	0.1748	2.9	0.0272	2.5	0.84	173.0	4.2	163.6	4.4	29.9	37.8	173.0	4.2
Spot 79	344	58676	0.9	20.0214	1.4	0.1876	3.0	0.0272	2.6	0.88	173.3	4.4	174.6	4.7	192.5	33.1	173.3	4.4
Spot 118	626	13181	1.1	18.1359	1.0	0.2126	2.0	0.0280	1.8	0.86	177.8	3.1	195.8	3.6	417.8	22.9	177.8	3.1
Spot 71	321	567	0.6	7.2994	2.7	0.5405	3.5	0.0286	2.3	0.64	181.9	4.0	438.7	12.5	2189.6	46.5	181.9	4.0
Spot 117	315	13523	1.6	19.8566	1.1	0.2068	3.0	0.0298	2.8	0.93	189.1	5.2	190.8	5.2	211.7	26.1	189.1	5.2

APPENDIX B

$^{40}Ar/^{39}Ar$ Isotopic Analyses Result Tables

BRISTOL MOUNTAINS

LH15BM9, Biotite, 9.17 mg, J = 0.00493 ± 0.14%

4 amu discrimination = 1.0583 ± 0.46%, 40/39K = 0.0041 ± 58.54%, 36/37Ca = 0.000255 ± 3.50%, 39/37Ca = 0.000697 ± 3.69%

step	T (C)	t (min.)	^{36}Ar	^{37}Ar	^{38}Ar	^{39}Ar	^{40}Ar	%^{40}Ar*	% ^{39}Ar rlsd	Ca/K	^{40}Ar*/^{39}ArK	Age (Ma)	1s.d.
1	660	12	4.499	1.512	3.906	213.463	2697.29	53.5	8.0	0.04130665	6.836349	59.80	0.56
2	700	12	3.421	0.612	4.159	257.665	3071.16	69.0	9.6	0.013851065	8.317712	72.50	0.55
3	730	12	0.580	0.424	3.617	264.879	2344.49	93.3	9.9	0.009334798	8.346624	72.75	0.44
4	760	12	0.400	0.328	3.321	243.484	2117.42	95.1	9.1	0.007855789	8.350955	72.79	0.44
5	790	12	0.302	0.292	2.675	197.854	1713.02	95.6	7.4	0.008606459	8.346975	72.75	0.44
6	820	12	0.378	0.313	1.810	126.066	1126.55	91.4	4.7	0.014478835	8.214503	71.62	0.44
7	850	12	0.375	0.330	1.151	80.453	752.960	87.2	3.0	0.023919947	8.177422	71.30	0.46
8	890	12	0.396	0.379	1.047	72.085	689.510	85.2	2.7	0.030660816	8.152626	71.09	0.47
9	930	12	0.424	0.480	1.155	78.048	739.303	85.1	2.9	0.035864893	8.074750	70.43	0.46
10	980	12	0.480	0.781	2.016	142.512	1289.71	90.3	5.3	0.031958704	8.220002	71.67	0.45
11	1020	12	0.415	0.896	2.987	220.174	1908.63	94.4	8.2	0.023731788	8.252411	71.94	0.43
12	1060	12	0.428	1.037	4.595	334.550	2862.33	96.1	12.5	0.01807613	8.308582	72.42	0.43
13	1130	12	0.408	2.131	5.212	384.720	3255.05	96.8	14.3	0.032301917	8.274644	72.13	0.44
14	1400	12	0.274	6.210	0.927	65.245	609.231	90.3	2.4	0.555140331	8.309284	72.43	0.46
								Cumulative %^{39}Ar rlsd =	**100.0**		**Total gas age =**	**71.23**	**0.24**

note: isotope beams in mV, rlsd = released, error in age includes J error, all errors 1 sigma

(36Ar through 40Ar are measured beam intensities, corrected for decay for the age calculations)

No plateau

No isochron

LH15BM13, **Muscovite**, 6.63 mg, J = 0.00479 ± 0.25%

4 amu discrimination = 1.0467 ± 1.41%, 40/39K = 0.0041 ± 58.54%, 36/37Ca = 0.000255 ± 3.50%, 39/37Ca = 0.000697 ± 3.69%

step	T (C)	t (min.)	^{36}Ar	^{37}Ar	^{38}Ar	^{39}Ar	^{40}Ar	%^{40}Ar*	% ^{39}Ar rlsd	Ca/K	^{40}Ar*/^{39}ArK	Age (Ma)	1s.d.
1	800	12	2.966	0.328	2.230	114.920	1765.92	52.9	6.3	0.200801106	8.168094	69.24	1.96
2	850	12	0.866	0.024	3.079	224.575	2163.42	89.0	12.3	0.007518172	8.625277	73.04	1.37
3	880	12	0.461	0.016	3.408	255.331	2313.30	94.7	14.0	0.004408374	8.630217	73.08	1.32
4	910	12	0.246	0.014	2.701	201.759	1774.51	96.5	11.1	0.004881544	8.530704	72.25	1.29
5	940	12	0.218	0.013	2.045	150.167	1307.07	96.1	8.2	0.006090194	8.374899	70.96	1.31
6	970	12	0.224	0.005	1.563	118.076	1069.86	95.1	6.5	0.002978998	8.609612	72.91	1.31
7	1010	12	0.287	0.014	1.960	146.326	1323.61	94.7	8.0	0.006730834	8.574551	72.62	1.31
8	1060	12	0.370	0.006	3.150	238.507	2145.36	95.6	13.1	0.00176975	8.637689	73.14	1.32
9	1090	12	0.194	0.016	2.886	222.754	1957.18	97.8	12.2	0.005053085	8.621300	73.00	1.32
10	1120	12	0.086	0.007	1.507	113.782	994.625	98.7	6.2	0.004327992	8.612745	72.93	1.28
11	1160	12	0.071	0.011	0.360	26.872	247.631	97.3	1.5	0.028797709	8.604672	72.87	1.30
12	1400	12	0.112	0.010	0.148	9.605	113.552	86.8	0.5	0.073244281	8.646245	73.21	1.53
								Cumulative %^{39}Ar rlsd =	**100.0**		**Total gas age =**	**72.50**	**0.78**
											Plateau age =	**72.57**	**0.80**
											(steps 1-13)		
											No isochron		

note: isotope beams in mV, rlsd = released, error in age includes J error, all errors 1 sigma

(36Ar through 40Ar are measured beam intensities, corrected for decay for the age calculations)

LH15BM16, Biotite, 9.74 mg, J = 0.00484 ± 0.16%

4 amu discrimination = 1.0583 ± 0.46%, 40/39K = 0.0041 ± 58.54%, 36/37Ca = 0.000255 ± 3.50%, 39/37Ca = 0.000697 ± 3.69%

step	T(C)	t(min.)	^{36}Ar	^{37}Ar	^{38}Ar	^{39}Ar	^{40}Ar	%^{40}Ar*	% ^{39}Ar rlsd	Ca/K	^{40}Ar*/^{39}ArK	Age (Ma)	1s.d.
1	660	12	4.033	5.374	3.935	226.933	2691.97	58.3	8.6	0.129899715	6.988452	60.01	0.53
2	700	12	1.271	0.916	3.236	225.404	2278.00	84.6	8.6	0.022290914	8.639235	73.90	0.48
3	730	12	0.222	0.633	3.066	226.354	1980.18	97.2	8.6	0.01533941	8.581018	73.41	0.44
4	760	12	0.185	0.621	3.142	233.312	2025.45	97.9	8.9	0.014599821	8.573384	73.35	0.44
5	790	12	0.233	0.696	2.663	195.258	1711.48	96.7	7.4	0.01955213	8.546190	73.12	0.44
6	820	12	0.248	0.796	1.941	143.279	1284.36	95.3	5.5	0.030473731	8.597956	73.56	0.45
7	850	12	0.219	0.743	1.437	105.077	957.923	94.6	4.0	0.03878621	8.655223	74.04	0.45
8	890	12	0.248	1.010	1.352	98.557	911.406	93.4	3.8	0.056212434	8.667156	74.14	0.46
9	930	12	0.281	1.594	1.643	118.688	1104.33	93.7	4.5	0.07366858	8.765744	74.96	0.46
10	980	12	0.337	2.724	2.931	215.443	1953.78	95.7	8.2	0.069354547	8.746882	74.80	0.45
11	1030	12	0.314	3.271	3.808	284.611	2499.88	96.9	10.8	0.063041749	8.583880	73.44	0.44
12	1080	12	0.281	3.895	4.202	314.087	2727.52	97.5	12.0	0.068023277	8.546071	73.12	0.44
13	1150	12	0.227	6.239	2.551	187.263	1638.78	96.9	7.1	0.18275874	8.529136	72.98	0.44
14	1400	12	0.374	16.783	0.734	51.074	536.386	84.0	1.9	1.803425065	8.651524	74.00	0.50
								Cumulative %^{39}Ar rlsd =	**100.0**		**Total gas age =**	**72.46**	**0.24**
											Pseudo plateau age =	**73.63**	**0.35**
											(steps 2-8)		
											No isochron		

note: isotope beams in mV, rlsd = released, error in age includes J error, all errors 1 sigma

(36Ar through 40Ar are measured beam intensities, corrected for decay for the age calculations)

LH15BM17, Biotite, 6.91 mg, J = 0.00487 ± 0.14%

4 amu discrimination = 1.0583 ± 0.46%, 40/39K = 0.0041 ± 58.54%, 36/37Ca = 0.000255 ± 3.50%, 39/37Ca = 0.000697 ± 3.69%

step	T(C)	t(min.)	^{36}Ar	^{37}Ar	^{38}Ar	^{39}Ar	^{40}Ar	%^{40}Ar*	% ^{39}Ar rlsd	Ca/K	^{40}Ar*/^{39}ArK	Age (Ma)	1s.d.
1	660	12	1.896	2.534	1.769	92.375	1125.99	53.3	4.8	0.153356048	6.538774	56.55	0.53
2	700	12	1.586	0.718	1.421	80.703	1129.63	61.1	4.2	0.049735888	8.614120	74.14	0.62
3	730	12	0.389	0.468	1.372	97.222	923.235	88.9	5.0	0.026909982	8.482877	73.03	0.46
4	760	12	0.265	0.527	1.907	138.635	1225.35	94.7	7.2	0.021250497	8.421373	72.51	0.44
5	790	12	0.216	0.570	2.095	155.224	1351.50	96.2	8.0	0.020528029	8.434052	72.62	0.43
6	820	12	0.182	0.514	1.735	127.287	1110.80	96.2	6.6	0.022574108	8.444954	72.71	0.44
7	850	12	0.149	0.446	1.160	86.462	763.463	95.7	4.5	0.02883646	8.470788	72.93	0.44
8	890	12	0.171	0.481	0.972	68.326	620.313	93.8	3.5	0.039354357	8.505753	73.22	0.45
9	930	12	0.199	0.545	0.885	63.764	591.438	92.1	3.3	0.047781063	8.531595	73.44	0.45
10	980	12	0.250	1.268	1.832	134.351	1236.38	95.1	7.0	0.052761102	8.800988	75.71	0.45
11	1030	12	0.304	1.531	4.733	348.742	3037.36	97.5	18.1	0.024541592	8.578308	73.84	0.44
12	1080	12	0.305	1.830	5.316	393.189	3376.57	97.7	20.4	0.026018468	8.481929	73.02	0.43
13	1150	12	0.145	3.675	1.635	120.936	1049.93	97.3	6.3	0.169884074	8.464863	72.88	0.43
14	1400	12	0.233	4.409	0.330	21.076	242.495	79.6	1.1	1.169861404	8.622778	74.21	0.52
								Cumulative %^{39}Ar rlsd =	**100.0**		**Total gas age =**	**72.55**	**0.24**

note: isotope beams in mV, rlsd = released, error in age includes J error, all errors 1 sigma **No plateau**

(36Ar through 40Ar are measured beam intensities, corrected for decay for the age calculations) **No isochron**

Hess-UNLV, LH15BM18, Biotite, 9.39 mg, J = 0.00579 ± 0.25%
4 amu discrimination = 1.0579 ± 0.09%, 40/39K = 0.0071 ± 9.38%, 36/37Ca = 0.000231 ± 0.29%, 39/37Ca = 0.000627 ± 0.08%

step	T (C)	t (min.)	36Ar	37Ar	38Ar	39Ar	40Ar	%40Ar*	% 39Ar rlsd	Ca/K	40Ar*/39ArK	Age (Ma)	1s.d.
1	660	12	4.267	1.155	2.957	159.674	2309.85	48.7	5.4	0.066112743	7.102896	72.71	0.31
2	700	12	1.972	0.487	3.034	199.518	2072.40	73.8	6.7	0.022308948	7.731722	79.01	0.24
3	730	12	0.640	0.377	3.693	281.660	2238.73	92.5	9.5	0.012233401	7.411544	75.80	0.22
4	760	12	0.402	0.310	3.704	286.281	2178.20	95.3	9.6	0.009896917	7.312727	74.81	0.21
5	800	12	0.327	0.325	3.451	265.353	2018.51	96.0	8.9	0.011194128	7.360232	75.29	0.21
6	860	12	0.664	0.517	2.503	184.758	1603.65	88.4	6.2	0.02557525	7.234211	74.03	0.22
7	920	12	0.620	0.496	2.091	155.655	1306.03	87.6	5.2	0.02912404	7.368317	75.37	0.23
8	980	12	0.652	0.633	3.467	261.192	2068.30	91.7	8.8	0.022150117	7.311030	74.80	0.21
9	1030	12	0.613	0.614	5.918	456.743	3472.64	95.4	15.3	0.012286481	7.317616	74.86	0.23
10	1070	12	0.620	0.848	6.304	484.798	3688.34	95.6	16.3	0.015986982	7.340669	75.09	0.21
11	1130	12	0.263	1.516	2.591	201.737	1527.57	96.0	6.8	0.068683331	7.298957	74.68	0.21
12	1400	12	0.243	3.591	0.577	42.155	378.628	87.0	1.4	0.778732086	7.524101	76.93	0.31
								Cumulative %39Ar rlsd =	**100.0**		**Total gas age =**	**75.17**	**0.07**
											No plateau		
											No isochron		

note: isotope beams in mV, rlsd = released, error in age includes J error, all errors 1 sigma
(36Ar through 40Ar are measured beam intensities, corrected for decay for the age calculations)

Hess-UNLV, LH15BM16, K-spar, 9.47 mg,
J = 0.00611 ± 0.47%
4 amu discrimination = 1.0197 ± 0.13%, 40/39K = 0.0071 ± 9.38%, 36/37Ca = 0.000231 ± 0.29%, 39/37Ca = 0.000627 ± 0.08%

step	T (C)	t (min.)	36Ar	37Ar	38Ar	39Ar	40Ar	%40Ar*	% 39Ar rlsd	Ca/K	40Ar*/39Ar K	Age (Ma)	1s.d.
1	422	11	1.781	0.092	0.408	2.193	603.106	14.7	0.1	0.479592775	40.721779	400.85	22.20
2	422	21	0.380	0.073	0.100	0.887	114.500	6.7	0.0	0.940973276	7.137519	77.01	19.93
3	473	10	0.280	0.081	0.103	2.611	108.868	28.6	0.1	0.354639243	10.881420	116.13	2.07
4	473	20	0.122	0.066	0.053	2.660	55.226	56.5	0.1	0.283636774	7.501464	80.85	3.31
5	525	9	0.258	0.116	0.133	5.825	115.747	39.0	0.1	0.227643718	7.229948	77.99	0.57
6	525	20	0.085	0.131	0.097	6.058	62.957	76.0	0.1	0.247194015	5.374902	58.30	1.33
7	576	12	0.186	0.242	0.220	13.839	152.058	71.7	0.3	0.199894563	7.262348	78.33	0.65
8	576	22	0.064	0.190	0.155	12.139	99.032	99.9	0.3	0.178919852	6.071113	65.71	0.46
9	627	12	0.180	0.323	0.318	22.823	201.159	80.0	0.5	0.161776563	6.636187	71.71	0.47
10	627	22	0.066	0.267	0.273	21.601	162.279	99.9	0.5	0.141293047	6.348609	68.66	0.69
11	679	12	0.170	0.425	0.420	32.454	263.039	85.0	0.8	0.149694237	6.619385	71.53	0.37
12	679	22	0.082	0.478	0.425	35.052	253.645	99.9	0.8	0.155883521	6.564931	70.95	0.38
13	730	12	0.263	0.899	0.718	52.844	419.213	84.1	1.3	0.194470482	6.519739	70.47	0.46
14	730	22	0.084	0.674	0.538	43.297	304.783	100.0	1.0	0.17794665	6.500213	70.27	0.42
15	781	13	0.127	1.160	0.787	62.643	448.480	94.9	1.5	0.211678701	6.625898	71.60	0.37
16	781	23	0.067	1.128	0.788	62.331	429.272	100.0	1.5	0.206869353	6.498893	70.25	0.35
17	822	19	0.106	1.503	1.025	82.016	577.035	98.1	1.9	0.209484482	6.673195	72.10	0.36
18	843	19	0.078	1.323	0.981	80.021	557.663	99.5	1.9	0.188992645	6.697746	72.36	0.36
19	884	19	0.129	1.594	1.365	110.421	768.646	97.7	2.6	0.165014777	6.635432	71.70	0.36
20	910	19	0.086	1.149	1.249	100.965	701.998	99.3	2.4	0.130086204	6.717861	72.57	0.37
21	935	19	0.126	0.890	1.200	97.831	678.800	97.5	2.3	0.103990217	6.575405	71.06	0.36
22	961	19	0.115	0.621	1.124	90.944	647.917	97.8	2.2	0.078053692	6.767357	73.10	0.37
23	976	19	0.086	0.403	0.871	73.884	524.029	99.9	1.8	0.062348884	6.801181	73.45	0.40

24	1002	19	0.149	0.430	0.984	77.080	551.447	96.7	1.8	0.06376773	6.653652	71.89	0.37
25	1018	19	0.133	0.348	0.808	66.799	488.483	97.2	1.6	0.059550168	6.802315	73.47	0.38
26	1038	19	0.162	0.341	0.856	65.918	489.757	95.5	1.6	0.059132197	6.784741	73.28	0.39
27	1089	13	0.269	0.574	1.094	85.309	657.311	90.5	2.0	0.07691177	6.837753	73.84	0.37
28	1089	23	0.249	0.563	1.129	88.103	673.044	93.2	2.1	0.073045423	6.849756	73.97	0.40
29	1089	57	0.470	0.805	1.730	135.524	1071.36	93.8	3.2	0.067897591	6.942313	74.95	0.40
30	1089	117	0.914	1.132	2.296	172.709	1407.70	91.1	4.1	0.07492159	6.654785	71.90	0.43
31	1192	11	0.860	1.312	2.109	158.238	1358.29	82.4	3.8	0.094776557	7.034069	75.92	0.41
32	1243	11	2.637	2.450	6.608	514.393	4239.28	82.2	12.2	0.054443262	6.775576	73.18	0.37
33	1346	11	7.921	3.513	22.821	1744.24	14115.99	83.7	41.4	0.023021907	6.794851	73.39	0.38
34	1398	11	0.681	0.668	1.141	85.344	774.91	75.8	2.0	0.089470676	6.795418	73.39	0.41
								Cumulative %39Ar rlsd =	**100.0**		**Total gas age =**	**73.24**	**0.35**

note: isotope beams in mV, rlsd = released, error in age includes J error, all errors 1 sigma
(36Ar through 40Ar are measured beam intensities, corrected for decay for the age calculations)

Hess-UNLV, LH15BM18, K-spar, 16.71 mg, J = 0.00611 ± 0.45%
4 amu discrimination = 1.0197 ± 0.13%, 40/39K = 0.0071 ± 9.38%, 36/37Ca = 0.000231 ± 0.29%, 39/37Ca = 0.000627 ± 0.08%

step	T (C)	t (min.)	36Ar	37Ar	38Ar	39Ar	40Ar	%40Ar*	% 39Ar rlsd	Ca/K	40Ar*/39 ArK	Age (Ma)	1s.d.
1	422	11	4.234	0.205	0.930	8.724	1252.67	2.1	0.1	0.273971402	3.026857	33.06	4.93
2	422	21	1.199	0.094	0.312	4.277	415.866	18.2	0.1	0.256243898	16.840256	176.69	5.58
3	473	10	0.536	0.116	0.262	9.624	253.663	40.6	0.1	0.140525004	10.323765	110.35	1.10
4	473	20	0.327	0.123	0.207	10.829	165.860	48.7	0.2	0.1324241	6.592769	71.25	1.08
5	525	9	0.385	0.188	0.359	21.937	269.356	60.8	0.3	0.099914159	7.268981	78.40	0.58
6	525	20	0.145	0.157	0.240	18.378	155.054	79.5	0.3	0.099597352	5.855888	63.42	0.35
7	576	12	0.206	0.277	0.451	33.623	271.095	82.4	0.5	0.096048209	6.372265	68.91	0.39
8	576	22	0.137	0.279	0.434	33.878	249.143	93.8	0.5	0.096013522	6.223976	67.33	0.36
9	627	12	0.329	0.476	0.798	61.010	490.240	83.0	0.9	0.090960176	6.532192	70.60	0.38
10	627	22	0.110	0.457	0.703	57.682	400.191	98.4	0.8	0.092367974	6.421283	69.43	0.35
11	679	12	0.345	0.789	1.138	86.248	661.519	86.4	1.2	0.106653519	6.542758	70.72	0.35
12	679	22	0.094	0.759	1.014	81.117	555.304	99.7	1.1	0.109088107	6.560402	70.90	0.35
13	730	12	0.332	1.109	1.281	99.956	754.013	88.6	1.4	0.129351832	6.613344	71.46	0.36
14	730	22	0.103	0.994	1.039	85.335	582.691	99.3	1.2	0.135803156	6.528512	70.57	0.35
15	781	13	0.164	1.299	1.199	95.482	686.426	95.1	1.3	0.158613817	6.742135	72.83	0.36
16	781	23	0.072	1.121	0.985	80.722	553.242	95.9	1.1	0.161907684	6.299800	68.14	0.35
17	822	19	0.159	1.505	1.171	94.740	669.305	96.0	1.3	0.185207956	6.599376	71.32	0.34
18	843	19	0.148	1.313	0.995	76.639	541.871	95.6	1.1	0.199743722	6.529833	70.58	0.37
19	884	19	0.207	1.757	1.224	98.845	709.688	94.2	1.4	0.207241241	6.595129	71.27	0.34
20	910	19	0.170	1.465	1.129	90.749	652.998	95.4	1.3	0.188214315	6.673951	72.11	0.35
21	935	19	0.197	1.178	1.118	87.781	645.979	94.1	1.2	0.156458039	6.728817	72.69	0.35
22	961	19	0.269	1.003	1.178	93.060	690.716	91.3	1.3	0.125657193	6.603812	71.36	0.36
23	976	19	0.217	0.727	1.053	84.911	634.446	93.9	1.2	0.099819839	6.795323	73.39	0.37

24	1002	19	0.384	0.775	1.287	99.801	779.925	88.7	1.4	0.090534086	6.758194	73.00	0.40
25	1018	19	0.405	0.699	1.336	103.406	806.511	88.3	1.5	0.078808917	6.721261	72.61	0.36
26	1038	19	0.572	0.806	1.527	116.877	960.280	85.0	1.7	0.080398898	6.852119	73.99	0.37
27	1089	13	1.280	1.363	2.558	184.930	1628.00	78.0	2.6	0.085927713	6.838887	73.85	0.38
28	1089	23	1.011	1.424	2.671	200.396	1665.34	83.8	2.8	0.082844817	6.882462	74.31	0.39
29	1089	57	1.602	1.886	3.830	292.238	2406.94	83.3	4.1	0.075239951	6.685659	72.23	0.37
30	1089	117	1.929	2.257	4.865	367.973	3034.41	85.9	5.2	0.071508664	6.763862	73.06	0.39
31	1192	11	3.021	3.253	5.545	409.136	3684.15	76.5	5.8	0.092696201	6.895981	74.46	0.38
32	1243	11	8.802	7.526	17.754	1330.10	14210.84	82.1	18.8	0.06596633	6.739963	72.81	0.36
33	1346	11	15.370	8.282	31.737	2388.468	20761.72	78.5	33.7	0.040425479	6.855333	74.03	0.36
34	1398	11	1.564	1.229	2.320	168.604	1603.16	84.2	2.4	0.084982336	7.983363	85.92	0.44
								Cumulative %39Ar rlsd =	**100.0**		**Total gas age =**	**73.43**	**0.33**

note: isotope beams in mV, rlsd = released, error in age includes J error, all errors 1 sigma
(36Ar through 40Ar are measured beam intensities, corrected for decay for the age calculations)

GRANITE MOUNTAINS

LH15GM6, Biotite, 9.67 mg, J = 0.00489 ± 0.14%

4 amu discrimination = 1.0583 ± 0.46%, 40/39K = 0.0041 ± 58.54%, 36/37Ca = 0.000255 ± 3.50%, 39/37Ca = 0.000697 ± 3.69%

step	T(C)	t(min.)	^{36}Ar	^{37}Ar	^{38}Ar	^{39}Ar	^{40}Ar	%^{40}Ar*	% ^{39}Ar rlsd	Ca/K	^{40}Ar*/^{39}ArK	Age (Ma)	1s.d.
1	660	12	8.179	4.321	10.698	539.278	4690.87	51.3	18.9	0.045669995	4.518972	39.43	0.39
2	700	12	2.865	1.694	5.349	294.412	2834.10	71.9	10.3	0.032795602	6.996815	60.69	0.45
3	730	12	1.461	1.127	3.686	212.578	1938.45	79.2	7.4	0.030217865	7.290803	63.20	0.44
4	760	12	0.940	0.816	2.640	152.445	1372.63	81.4	5.3	0.03050945	7.384153	63.99	0.43
5	790	12	0.776	0.715	2.065	120.532	1103.08	81.1	4.2	0.033811272	7.458744	64.63	0.46
6	820	12	0.849	0.875	2.205	127.045	1185.25	80.6	4.4	0.03925627	7.569212	65.57	0.45
7	850	12	1.057	1.112	2.499	141.270	1350.47	78.7	4.9	0.044865667	7.575560	65.62	0.46
8	890	12	1.052	1.362	2.190	120.919	1172.29	75.6	4.2	0.064201385	7.369825	63.87	0.45
9	930	12	1.363	1.634	2.761	152.707	1476.29	74.7	5.3	0.060989422	7.276364	63.08	0.46
10	980	12	1.868	2.588	4.662	264.058	2433.27	78.9	9.2	0.055863183	7.336122	63.59	0.45
11	1020	12	1.283	2.518	3.902	225.825	2012.43	82.6	7.9	0.063554376	7.423383	64.33	0.44
12	1060	12	0.088	3.615	3.100	179.219	1572.04	99.1	6.3	0.114972181	8.753289	75.61	0.44
13	1130	12	0.740	6.570	4.234	256.326	2188.59	91.1	9.0	0.146098354	7.839042	67.86	0.42
14	1400	12	0.480	9.464	1.208	69.448	655.923	82.1	2.4	0.776909822	7.655511	66.30	0.44
								Cumulative %^{39}Ar rlsd =	**100.0**		**Total gas age =**	**60.20**	**0.23**

note: isotope beams in mV, rlsd = released, error in age includes J error, all errors 1 sigma **No plateau**

(36Ar through 40Ar are measured beam intensities, corrected for decay for the age calculations)

Hess-UNLV, LH15GM7, Biotite, 11.87 mg, J = 0.00592 ± 0.28%
4 amu discrimination = 1.0579 ± 0.09%, 40/39K = 0.0071 ± 9.38%, 36/37Ca = 0.000231 ± 0.29%, 39/37Ca = 0.000627 ± 0.08%

step	T (C)	t (min.)	36Ar	37Ar	38Ar	39Ar	40Ar	%40Ar*	% 39Ar rlsd	Ca/K	40Ar*/39ArK	Age (Ma)	1s.d.
1	660	12	11.668	1.196	8.353	441.151	5709.36	43.0	11.4	0.02436045	5.626821	59.12	0.24
2	700	12	3.420	0.663	5.486	384.481	3636.90	73.9	9.9	0.015494551	7.066377	73.93	0.25
3	730	12	0.941	0.522	5.660	442.319	3424.96	92.6	11.4	0.010604121	7.242052	75.73	0.24
4	760	12	0.595	0.409	5.520	436.687	3293.38	95.2	11.3	0.008415745	7.254454	75.86	0.23
5	800	12	0.459	0.319	4.227	332.828	2503.25	95.3	8.6	0.008612126	7.230238	75.61	0.24
6	840	12	0.441	0.318	2.170	166.488	1264.96	91.1	4.3	0.017162665	6.954817	72.79	0.25
7	880	12	0.426	0.294	1.409	109.636	878.227	87.7	2.8	0.024095476	7.029117	73.55	0.23
8	920	12	0.523	0.351	1.493	112.718	904.192	85.0	2.9	0.027980513	6.826668	71.48	0.26
9	980	12	0.864	0.569	2.777	212.588	1645.84	86.0	5.5	0.024049989	6.687906	70.05	0.22
10	1030	12	0.923	0.707	3.743	284.339	2147.58	88.5	7.3	0.022342108	6.728014	70.46	0.23
11	1080	12	0.817	1.050	5.142	403.494	2980.93	92.7	10.4	0.023382638	6.906567	72.30	0.23
12	1140	12	0.562	2.151	5.437	430.211	3168.99	95.4	11.1	0.044926515	7.088912	74.17	0.22
13	1400	12	0.319	12.514	1.497	115.764	895.667	92.5	3.0	0.9715746	7.097108	74.25	0.26
								Cumulative %39Ar rlsd =	**100.0**		**Total gas age =**	**72.08**	**0.07**

note: isotope beams in mV, rlsd = released, error in age includes J error, all errors 1 sigma
(36Ar through 40Ar are measured beam intensities, corrected for decay for the age calculations)

No plateau

No isochron

Hess-UNLV, LH15GM6, Amphibole, 21.54 mg, J = 0.00583 ± 0.25%
4 amu discrimination = 1.0579 ± 0.09%, 40/39K = 0.0071 ± 9.38%, 36/37Ca = 0.000231 ± 0.29%, 39/37Ca = 0.000627 ± 0.08%

step	T (C)	t (min.)	36Ar	37Ar	38Ar	39Ar	40Ar	%40Ar*	% 39Ar rlsd	Ca/K	40Ar*/39ArK	Age (Ma)	1s.d.
1	600	12	1.982	2.811	0.625	12.309	657.014	16.4	1.4	2.131332367	8.740304	89.66	1.75
2	680	12	0.960	1.498	0.424	14.103	388.005	32.3	1.6	0.991010979	8.780777	90.07	1.22
3	770	12	1.327	1.228	0.498	14.035	514.734	29.0	1.6	0.816288029	10.571217	107.89	1.06
4	850	12	0.542	1.901	0.322	12.719	247.929	41.7	1.4	1.39461739	7.885407	81.09	0.89
5	940	12	0.532	20.467	0.774	31.208	365.908	63.2	3.5	6.127367477	7.239662	74.58	0.47
6	980	12	0.310	20.852	0.583	25.488	262.567	72.9	2.9	7.646755067	7.227078	74.46	0.68
7	1020	12	0.272	37.951	1.110	41.727	372.127	85.4	4.7	8.503005005	7.452238	76.73	0.25
8	1050	12	0.489	131.297	3.464	113.595	953.839	90.7	12.8	10.81271345	7.625638	78.47	0.25
9	1070	12	0.475	231.382	6.121	190.292	1479.73	96.1	21.5	11.37665825	7.526461	77.47	0.22
10	1090	12	0.214	120.284	3.380	101.426	790.640	98.2	11.4	11.09509442	7.646394	78.68	0.25
11	1130	12	0.167	64.099	1.627	52.418	418.061	96.3	5.9	11.44153086	7.535493	77.57	0.28
12	1210	12	0.526	227.259	5.571	173.230	1409.47	94.9	19.5	12.27750072	7.768693	79.91	0.22
13	1400	12	0.380	137.838	3.379	103.776	859.916	94.2	11.7	12.43088696	7.763525	79.86	0.30
								Cumulative %39Ar rlsd =	**100.0**		**Total gas age =**	**79.18**	**0.11**

note: isotope beams in mV, rlsd = released, error in age includes J error, all errors 1 sigma
(36Ar through 40Ar are measured beam intensities, corrected for decay for the age calculations)

No plateau

No isochron

Hess-UNLV, LH15GM7, K-spar, 11.55 mg, J = 0.00610 ± 0.55%
4 amu discrimination = 1.0197 ± 0.13%, 40/39K = 0.0071 ± 9.38%, 36/37Ca = 0.000231 ± 0.29%, 39/37Ca = 0.000627 ± 0.08%

step	T (C)	t (min.)	36Ar	37Ar	38Ar	39Ar	40Ar	%40Ar *	% 39Ar rlsd	Ca/K	40Ar*/39Ar K	Age (Ma)	1s.d.
1	422	11	3.864	0.104	0.873	4.148	1223.750	8.6	0.1	0.27921681	25.560174	261.40	4.04
2	422	21	1.664	0.067	0.357	1.908	497.614	3.6	0.0	0.391071929	9.226116	98.78	10.62
3	473	10	0.675	0.066	0.214	4.493	262.119	26.6	0.1	0.16358399	15.048390	158.44	1.45
4	473	20	0.553	0.070	0.186	4.741	198.800	21.5	0.1	0.164422582	8.183152	87.88	3.70
5	525	9	0.361	0.085	0.210	10.970	185.533	46.2	0.2	0.086285223	7.499697	80.70	1.47
6	525	20	0.259	0.084	0.217	12.752	163.906	61.7	0.2	0.073353963	6.996135	75.39	0.54
7	576	12	0.224	0.113	0.361	25.690	235.178	77.3	0.4	0.048981722	6.731807	72.60	0.60
8	576	22	0.155	0.114	0.320	24.904	207.343	89.5	0.4	0.050974819	6.570684	70.90	0.60
9	627	12	0.169	0.156	0.488	38.700	307.256	88.2	0.6	0.044888269	6.751863	72.81	0.45
10	627	22	0.106	0.133	0.486	38.616	285.853	98.1	0.6	0.038353306	6.647539	71.71	0.44
11	679	12	0.164	0.240	0.747	58.377	426.978	91.3	1.0	0.045781372	6.532128	70.49	0.40
12	679	22	0.127	0.225	0.809	64.372	454.393	94.0	1.1	0.038922797	6.315224	68.19	0.41
13	730	12	0.166	0.383	1.170	93.325	666.176	94.3	1.6	0.04570041	6.653023	71.77	0.42
14	730	22	0.095	0.382	1.206	98.452	681.780	99.7	1.6	0.043207372	6.690566	72.17	0.41
15	781	13	0.139	0.560	1.549	127.453	880.048	96.9	2.1	0.048928023	6.630520	71.53	0.42
16	781	23	0.103	0.631	1.818	150.770	1035.59	99.5	2.5	0.046605144	6.700875	72.28	0.41
17	822	19	0.111	0.798	2.170	175.973	1196.24	98.9	2.9	0.050498299	6.636382	71.59	0.41
18	843	19	0.095	0.691	1.859	151.939	1028.43	99.2	2.5	0.050644081	6.607926	71.29	0.41
19	884	19	0.092	0.843	2.359	193.742	1327.65	99.4	3.2	0.04845331	6.737294	72.66	0.42
20	910	19	0.112	0.745	2.219	183.384	1260.12	98.9	3.1	0.045239115	6.716293	72.44	0.42

21	935	19	0.094	0.569	2.088	172.168	1182.67	99.3	2.9	0.036802566	6.732375	72.61	0.42
22	961	19	0.113	0.529	2.121	170.232	1171.45	98.8	2.8	0.034604492	6.710145	72.37	0.41
23	976	19	0.127	0.435	2.003	163.807	1130.55	98.9	2.7	0.029571559	6.722631	72.51	0.41
24	1002	19	0.170	0.397	2.143	171.628	1202.46	97.9	2.9	0.025758426	6.763974	72.94	0.42
25	1018	19	0.173	0.314	1.931	156.739	1102.02	97.7	2.6	0.022308436	6.757540	72.87	0.42
26	1038	19	0.180	0.300	1.865	154.724	1094.90	97.5	2.6	0.021591362	6.786211	73.18	0.42
27	1089	13	0.291	0.385	2.537	203.888	1463.88	95.3	3.4	0.021027395	6.803813	73.36	0.42
28	1089	23	0.319	0.407	2.751	220.695	1597.91	95.9	3.7	0.020536114	6.851992	73.87	0.43
29	1089	57	0.641	0.586	4.003	319.429	2344.13	95.0	5.3	0.020428647	6.792740	73.25	0.42
30	1089	117	0.886	0.695	4.564	362.830	2744.35	95.9	6.1	0.021330354	6.891851	74.29	0.44
31	1192	11	0.904	0.648	3.553	275.451	2140.65	88.2	4.6	0.026196765	6.849720	73.85	0.43
32	1243	11	1.912	0.869	8.072	631.269	4870.60	88.8	10.5	0.015329255	6.865435	74.01	0.43
33	1346	11	3.865	0.832	17.396	1380.27	10479.39	89.3	23.0	0.006712355	6.807220	73.40	0.42
34	1398	11	0.603	0.188	1.929	148.319	1197.91	86.3	2.5	0.014114862	6.930015	74.70	0.45
								Cumulative %39Ar rlsd =	**100.0**		**Total gas age =**	**73.31**	**0.40**

note: isotope beams in mV, rlsd = released, error in age includes J error, all errors 1 sigma
(36Ar through 40Ar are measured beam intensities, corrected for decay for the age calculations)

Hess-UNLV, LH15GM6, K-spar, 6.96 mg,
J = 0.00569 ± 0.32%
4 amu discrimination = 1.0197 ± 0.13%, 40/39K = 0.0071 ± 9.38%, 36/37Ca = 0.000231 ± 0.29%, 39/37Ca = 0.000627 ± 0.08%

step	T (C)	t (min.)	36Ar	37Ar	38Ar	39Ar	40Ar	%40Ar*	% 39Ar rlsd	Ca/K	40Ar*/39ArK	Age (Ma)	1s.d.
1	422	11	1.062	0.090	0.268	2.522	329.203	5.7	0.1	0.386250496	7.217484	72.61	4.88
2	422	21	0.282	0.063	0.088	1.159	91.888	16.8	0.0	0.588372902	9.489734	94.88	4.65
3	473	10	0.182	0.080	0.094	2.837	75.176	37.2	0.1	0.305205728	8.131704	81.60	0.83
4	473	20	0.127	0.062	0.072	2.978	52.570	57.6	0.1	0.225330286	4.982424	50.43	7.51
5	525	9	0.124	0.073	0.094	6.485	85.532	68.4	0.2	0.121829707	7.733206	77.69	1.41
6	525	20	0.074	0.088	0.096	6.489	61.852	99.8	0.2	0.146773676	5.376754	54.37	0.46
7	576	12	0.090	0.107	0.182	13.196	112.117	87.8	0.4	0.087756189	6.380078	64.33	0.30
8	576	22	0.067	0.095	0.157	12.268	99.326	99.9	0.4	0.083808035	5.696197	57.55	0.61
9	627	12	0.091	0.153	0.269	20.903	160.885	93.7	0.7	0.079216944	6.481766	65.34	0.51
10	627	22	0.084	0.150	0.278	20.886	156.122	99.9	0.7	0.077726853	6.062656	61.19	0.55
11	679	12	0.107	0.235	0.432	33.189	252.592	93.0	1.1	0.076631736	6.666808	67.17	0.36
12	679	22	0.076	0.220	0.419	33.352	241.913	99.9	1.1	0.071389633	6.417131	64.70	0.37
13	730	12	0.105	0.037	0.599	48.099	351.690	95.2	1.5	0.008325159	6.679548	67.30	0.27
14	730	22	0.070	0.325	0.548	44.353	320.161	99.8	1.4	0.079304101	6.590282	66.41	0.35
15	781	13	0.083	0.401	0.745	59.150	421.555	98.3	1.9	0.073370961	6.752065	68.01	0.27
16	781	23	0.081	0.345	0.764	61.378	438.066	99.8	2.0	0.060833032	6.668122	67.18	0.24
17	822	19	0.096	0.412	1.094	88.080	624.068	99.1	2.8	0.050623457	6.752166	68.01	0.26
18	843	19	0.085	0.275	0.831	66.237	470.942	99.6	2.1	0.044932776	6.707459	67.57	0.27
19	884	19	0.088	0.276	1.028	82.116	583.399	99.5	2.6	0.036375712	6.773613	68.23	0.25
20	910	19	0.075	0.178	0.837	68.487	495.399	99.9	2.2	0.028128145	6.865804	69.14	0.32
21	935	19	0.090	0.168	0.808	65.654	473.440	98.7	2.1	0.027693463	6.742759	67.92	0.26

22	961	19	0.098	0.140	0.787	67.232	491.770	98.8	2.1	0.022536194	6.862261	69.10	0.27
23	976	19	0.108	0.139	0.724	58.290	428.056	97.9	1.9	0.025807723	6.768555	68.18	0.27
24	1002	19	0.129	0.163	0.853	66.602	493.211	96.9	2.1	0.026486792	6.813682	68.62	0.28
25	1018	19	0.112	0.140	0.811	63.905	477.367	97.8	2.0	0.023709473	6.929888	69.77	0.28
26	1038	19	0.139	0.148	0.819	65.235	488.441	96.2	2.1	0.024553299	6.838577	68.87	0.32
27	1089	13	0.212	0.262	1.156	91.068	694.601	93.4	2.9	0.031136162	6.959256	70.06	0.29
28	1089	23	0.212	0.267	1.284	99.631	750.145	95.4	3.2	0.029003212	6.906094	69.54	0.27
29	1089	57	0.380	0.375	1.837	142.903	1101.49	96.2	4.6	0.028400055	6.934546	69.82	0.31
30	1089	117	0.574	0.433	2.186	168.100	1342.85	98.6	5.4	0.027877215	7.001492	70.48	0.35
31	1192	11	0.399	0.510	1.765	134.820	1052.84	90.0	4.3	0.040939883	6.956116	70.03	0.27
32	1243	11	0.746	0.599	4.010	318.153	2446.01	91.7	10.2	0.020376008	7.024792	70.71	0.26
33	1346	11	2.325	0.844	12.325	973.491	7521.06	91.3	31.1	0.009382909	7.052755	70.98	0.26
34	1398	11	0.373	0.313	1.793	142.351	1132.99	92.5	4.5	0.023796469	7.199230	72.43	0.27
								Cumulative %39Ar rlsd =	**100.0**		**Total gas age =**	**69.72**	**0.23**

note: isotope beams in mV, rlsd = released, error in age includes J error, all errors 1 sigma
(36Ar through 40Ar are measured beam intensities, corrected for decay for the age calculations)

REFERENCES

Anderson, J.L. and Smith, D.R., 1995, The effects of temperature and f02 on the Al-in hornblende barometer: American Mineralogist, v. 80, p. 549-559.

Applegate, J.D.R., Walker, J.D., Hodges, K.V., 1992, Late Cretaceous extensional unroofing in the Funeral Mountains metamorphic core complex, California: Geology. v. 19, p. 519–522.

Applegate, J.D., Hodges, K.V., 1995, Mesozoic and Cenozoic extension recorded by metamorphic rocks in the Funeral Mountains, California: Geological Society of America Bulletin, v. 107, p. 1063–1076.

Barth, A. P., and Schneiderman, J. S., 1996, A comparison of structures in the Andean Orogen of northern Chile and exhumed midcrustal structures in southern California, USA: An analogy in tectonic style?, International Geology Review, v. 38, p. 1075–1085.

Beyene, M.A., 2000, Kinematics and timing of the Pinto Shear Zone, New York Mountains, Northeastern Mojave Desert, California. MS thesis, University of Nevada, Las Vegas.

Burchfiel, B.C., Davis, G.A., 1976. Compression and crustal shortening in Andean-type orogenesis: Nature, v. 260, p. 693–694.

Burchfiel, B.C., Cowan, D.S., and Davis, G.A., 1992, Tectonic overview of the Cordilleran orogen in the western United States, *in* Burchfiel, B.C., Lipman, P.W., and Zoback, M.L., eds., The Cordilleran Orogen: Conterminous U.S.: Boulder, Colorado, Geological Society of America, The Geology of North America, v. G-3, p. 407-479.

Carl, B.C., Miller, C.F., Foster, D.A., 1991, Western Old Woman Mountains shear zone: evidence for latest Cretaceous core complex development in the southeastern California: Geology, v. 19, p. 893–896.

Coney, P. J., and T. A. Harms, 1984, Cordilleran metamorphic core complexes: Cenozoic extensional relics of Mesozoic compression: Geology, v. 12, p. 550–554.

Copeland, P., Currie, C.A., Lawton, T.F., and Murphy, M.A., 2017, Location, location, location: The Variable lifespan of the Laramide orogeny: Geology, v. 45(3), p. 223-226.

Constenius, K. N., 1996, Late Paleogene extensional collapse of the Cordilleran foreland fold and thrust belt: Geological Society America Bulletin, v. 108, p. 20–39.

DeCelles, P. G., 2004, Late Jurassic to Eocene evolution of the Cordilleran thrust belt and foreland basin system, western U.S.A.: American. Journal of Science, v. 304, p. 105–168.

DeCelles, P.G., and Graham, S.A., 2015, Cyclical processes in the North American Cordilleran orogenic system: Geology, v. 43, p. 499-502.

DeCelles, P.G., Ducea, M.N., Kapp, P., and Zandt, G., 2009, Cyclicity in Cordilleran orogenic systems: Nature Geoscience, v. 2, p. 251–257.

Dickinson, W. R., 2002, The Basin and Range province as a composite extensional domain: International Geology Review, v. 44, p. 1–38.

Dickinson, W.R., and Snyder, W.S., 1979, Geometry of subducted slabs related to San Andreas transform: The Journal of Geology, v. 87, p. 609-627.

Druschke, P., Hanson, A.D., Wells, M.L., Gehrels, G.E. and Stockli, D., 2011. Paleogeographic isolation of the Cretaceous to Eocene Sevier hinterland, east-central Nevada: Insights from U-Pb and (U-Th)/He detrital zircon ages of hinterland strata. Geological Society of America Bulletin, 123(5-6), p.1141-1160.

Dumitru, T.A., Gans, P.B., Foster, D.A., 1991, Refrigeration of the western Cordilleran lithosphere during Laramide shallow-angle subduction: Geology, v. 19, p. 1145–1148.

England, P., and Houseman, G., 1989, Extension during continental convergence, with application to the Tibetan Plateau: Journal of Geophysical Research, Solid Earth, v. 94, p. 17561-17579.

Ernst, W.G., 2010, Subduction-zone metamorphism, calc-alkaline magmatism, and convergent-margin crustal evolution: Gondwana Research, v. 18(1), p. 8-16.

Faulds, J.E., Henry, C.D., and Hinz, N.H., 2005, Kinematics of the northern Walker Lane: An incipient transform fault along the Pacific–North American plate boundary: Geology, v. 33(6), p. 505-508.

Faulds, J.E., and Henry, C.D., 2008, Tectonic influences on the spatial and temporal evolution of the Walker Lane: An incipient transform fault along the evolving Pacifc – North American plate boundary, *in* Spencer, J.E., and Titley, S.R., eds., Ores and orogenesis: Circum-Pacific tectonics, geologic evolution, and ore deposits: Arizona Geological Society Digest v. 22, p. 437-470.

FitzGerald, J.D., and Stunitz, H., 1993, Deformation of granitoids at low metamorphic grade I: reactions and grain size reduction: Tectonophysics, v. 221, p. 299–324.

Foster, D.A., Harrison, T.M., Miller, C.F., and Howard, K.A., 1990, The $^{40}Ar/^{39}Ar$ thermochronology of the eastern Mojave Desert, California, and adjacent western Arizona with implications for the evolution of metamorphic core complexes: Journal of Geophysical Research, v. 95, p. 20,005-20,024.

Foster, D.A., Miller, C.F., Harrison, T.M., and Hoisch, T.D., 1992, $^{40}Ar/^{39}Ar$ thermochronology and thermobarometry of metamorphism, plutonism, and tectonic denudation in the Old Woman Mountains area, California: Geological Society of America Bulletin, v. 104, p. 176–191.

Gamble, J., 1959a, Geology and mineral resources of Township 8 North, Ranges 11 and 12 East, San Bernardino Base and Meridian, San Bernardino County, California: San Francisco, California, Southern Pacific company, unpublished report and l:24,000-scale map, 22 p.

Gamble, J., 1959b, Geology and mineral resources of Township 9 North, Ranges 11 and 12 East, San Bernardino Base and Meridian, San Bernardino County, California: San Francisco, California, Southern Pacific Company, unpublished report and 1:24,000-scale map, 18 p.

Gapais, D., 1989, Shear structures within deformed granites: mechanical and thermal indicators: Geology, v. 17, p. 1144-1147.

George, P.G., Dokka, R.K., 1994, Major Late Cretaceous cooling events in the eastern Peninsular Ranges, California, and their implications for Cordilleran tectonics: Geological Society of America Bulletin, v. 106, p. 903-914.

Glazner, A.F., 1994, Foundering of mafic plutons and density stratification of continental crust: Geology, v. 22(5), p. 435-438.

Grove, M., Lovera, O., and Harrison, M., 2003a, Late Cretaceous cooling of the east-central Peninsular RangesBatholith (33 degrees N); relationship to La Posta Pluton emplacement, Laramide shallow subduction, and forearc sedimentation, in Johnson, S.E., et al., eds., Tectonic Evolution of Northwestern Mexico andSouthwestern USA: Geological Society of America Special Paper 374, p. 355–379.

Guillope, M., and Poirier, J.P., 1979, Dynamic recrystallization during creep of single-crystalline halite: An experimental study: Journal of Geophysical Research, v. 84, p. 5557–5567.

Henderson, L.J., Gordon, R.G., and Engebretsen, D.C., 1984, Mesozoic aseismic ridges on the Farallon plate and southward migration of shallow subduction during the Laramide orogeny: Tectonics, v. 3, p. 121–132.

Hirth, G., and Tullis, J., 1992, Dislocation creep regimes in quartz aggregates: Journal of Structural Geology, v. 14, p. 145–159.

Hodges, K.V., and Walker, J.D., 1992, Extension in the Cretaceous Sevier orogen, North American Cordillera: Geological Society of America bulletin, v. 104, p. 560-569.

Holdsworth, R.E., Butler, C.A., and Roberts, A.M., 1997, The recognition of reactivation during continental deformation: Journal of the Geological Society, v. 154(1), p. 73-78.

Houseman, G.A., McKenzie, D.P., and Molnar, P., 1981, Convective instability of a thickened boundary layer and its relevance for the thermal evolution of continental convergent belts: Journal of Geophysical Research: Solid Earth, v, 86, p. 6115-6132.

Howard, K.A. and Miller, D.M., 1992, Late Cenozoic Faulting at the Boundary between the Mojave and Sonoran Blocks: Bristol Lake Area, California, *in* Richard, S.M., ed., Deformation associated with the Neogene Eastern California Shear Zone, southeastern

California and southwestern Arizona, San Bernardino County Museums Special Publication, p. 37-47.

Howard, K.A., Kilburn, J.E., Simpson, R.W., Fitzgibbon, Todd T., Detra, D.E., Raines, G.L, and Sabine, C., 1987, Mineral resources of the Bristol/Granite Mountains Wilderness Study Area, San Bernardino County, California: U. S. Geological Survey Bulletin, Report: B 1712-C, p.C1-C18.

Humphreys, E. D., 1995, Post-Laramide removal of the Farallon slab, western United States: Geology, v. 23, p. 987–990.

Ibanez-Mejia, M., Pullen, A., Arenstein, J., Gehrels, G.E., Valley, J., Ducea, M.N., Mora, A.R., Pecha, M. and Ruiz, J., 2015, Unraveling crustal growth and reworking processes in complex zircons from orogenic lower-crust: The Proterozoic Putumayo Orogen of Amazonia: Precambrian Research, v. 267, p.285-310.

Jacobson, C.E., 1990, The $^{40}Ar/^{39}Ar$ geochronology of the Pelona Schist and related rocks, Southern California: Journal of Geophysical Research, v. 95, p. 509–528.

Jacobson, C.E., Oyarzabal, F.R., Haxel, G.B., 1996, Subduction and exhumation of the Pelona–Orocopia–Rand schists, southern California: Geology, v. 24, p. 547–550.

Jones, C.H., Sonder, L.J. and Unruh, J.R., 1998, Lithospheric gravitational potential energy and past orogenesis: Implications for conditions of initial Basin and Range and Laramide deformation: Geology, v. 26, p.639-642.

Kula, J.L., 2002, Thermochronology and Geobarometry of the Granite Mountains, southeast California; Exhumation of a Plutonic Complex During Collapse of the Sevier Orogen: MS Thesis, University of Nevada, Las Vegas.

Lease, R.O., McQuarrie, N., Oskin, M., and Leier, A., 2009, Quantifying Dextral Shear on the Bristol-Granite Mountains Fault Zone: Successful Geologic Prediction from Kinematic Compatibility of the Eastern California Shear Zone: Journal of Geology, v. 117, p 37-53.

Liu, L., S. Spasojevic, and Gurnis, M., 2008, Reconstructing Farallon plate subduction beneath North American back to the Late Cretaceous: Science, v. 322, p. 934–938.

Liu, L., M. Gurnis, M. Seton, J. Saleeby, R. D. Müller, and Jackson, J. M., 2010, The role of oceanic plateau subduction in the Laramide orogeny: Nature Geoscience, v. 3, p. 353–357.

Livaccari, R. F., 1991, Role of crustal thickening and extensional collapse in the tectonic evolution of the Sevier-Laramide Orogeny, Western United States, Geology, 19, 1104–1107.

Lovera, O.M., 1992, Computer programs to model $^{40}Ar/^{39}Ar$ diffusion data from multidomain samples: Computers & Geosciences,v. 18, p. 789–813.

Lovera, O.M., Richter, F.M., and Harrison, T.M., 1991, Diffusion domains determined by ^{39}Ar released during step heating: Journal of Geophysical Research, v. 96, p. 2057–2069.

Lovera, O.M., Grove, M., Harrison, T.M., Mahon, K.I., 1997, Systematic analysis of K-feldspar $^{40}Ar/^{39}Ar$ step-heating experiments I: significance of activation energy determinations: Geochimica et Cosmochimica Acta, v. 61, p. 3171–3192.

Ludwig, K.R., 2001, User Manual for Isoplot: Berkeley Geochronology Center.

McCaffrey, K.J.W., Miller, C.F., Karlstrom, K.E., Simpson, C., 1999, Synmagmatic deformation patterns in the Old Woman Mountains, SE California: Journal of Structural Geology, v. 21, p. 335–349.

Miller, C.F., and Bradfish, L.J., 1980, An inner Cordilleran belt of muscovite-bearing plutons: Geology, v. 8, p. 412–416.

Miller, Fred K., and Douglas M. Morton. Potassium-argon geochronology of the eastern Transverse Ranges and southern Mojave Desert, southern California. No. 1152. 1980.

Molnar, P., and Lyon-Caen, H., 1988, Some simple physical aspects of the support, structure and evolution of mountain belts, in Clark, S.P., Jr., ed., Processes in Continental and Lithospheric Deformation: Geological Society of America Special Paper, v. 218, p. 179–207.

McDougall, I. and Harrison, T.M., 1999, Geochronology and Thermochronology by the $^{40}Ar/^{39}Ar$ Method, 2nd edition, Oxford University Press, New York, NY, 269 p.

Merrihue, C. and Turner, G., 1966. Potassium-argon dating by activation with fast neutrons: Journal of Geophysical Research, v. 71(11), p. 2852-2857.

Miller, D.M., and Howard, K.A., 1985, Bedrock geologic map of the Iron Mountains Quadrangle, San Bernardino and Riverside counties, California. US Geological Survey, Report, MF-1736.

Miller, D.M., Wells, M.L., Dewitt, E., Walker, J.D., and Nakata, J.K., 1996, Late Cretaceous extensional fault system across the northeastern Mojave Desert: San Bernardino County Museum Association Quarterly: v. 43 (1), p. 77–83.

Passchier, C.W., and Trouw, R.A., 1996, Microtectonics, Springer, Berlin, Germany. 289pp.

Patino Douce, A.E., Humphreys, E.D., and Johnston, A.D., 1990, Anatexis and metamorphism in tectonically thickened continental crust exemplified by the Sevier hinterland, western North America: Earth and Planetary Science Letters, v. 97, p. 290–315.

Platt, J.P., 1986, Dynamics of orogenic wegdes and the uplift of high-pressure metamorphic rocks: Geological Society of Americ Bulletin, v. 97(9), p. 1037-1053.

Pryer, L.L., 1993, Microstructures in feldspars from a major crustal thrust zone: the Grenville Front, Ontario, Canada: Journal of Structural Geology, v. 15, p. 21–36.

Saleeby, J., 2003, Segmentation of the Laramide Slab–Evidence from the southern Sierra Nevada region: Geological Society of America Bulletin: v. 115, p. 655–668.

Saleeby, J., Farley, K.A., Kistler, R.W., and Fleck, R., 2007, Thermal evolution and exhumation of deep-level batholithic exposures, southernmost Sierra Nevada, California, in Cloos, M., Carlson, W.D., Gilbert, M.C., Liou, J.G., and Sorensen, S.S., eds., Convergent Margin Terranes and Associated Regions: A Tribute to W.G. Ernst: Geological Society of America Special Paper, v. 419, p. 39–66, doi: 10.1130/2007.2419(02).

Singleton, J.S. and Mosher, S., 2012. Mylonitization in the lower plate of the Buckskin-Rawhide detachment fault, west-central Arizona: Implications for the geometric evolution of metamorphic core complexes: Journal of Structural Geology, p. 39, pp.180-198.

Snell, K.E., Koch, P.L., Druschke, P., Foreman, B.Z. and Eiler, J.M., 2014. High elevation of the 'Nevadaplano'during the Late Cretaceous: Earth and Planetary Science Letters, v. 386, p.52-63.

Simpson, C., 1985, Deformation of granitic rocks across the brittle-ductile transition: Journal of Structural Geology 7, 503-511.

Simpson, C. and Wintsch, R.P., 1989, Evidence for deformation-induced K-feldspar replacement by myrmekite: Journal of Metamorphic Geology 7, 261–275.

Smith, A.G., Wells, M.L., and Foster, D.A., 2003, Timing and development of an orogen-parallel lineation and of frontal thrusting in the southern Cordilleran fold–thrust belt, New York Mountains, California. Geological Society of America Abstracts with Programs.

Sonder, L. J., and Jones, C. H., 1999, Western United States extension: How the west was widened, Annual Review Earth Planetary Science Letters, v. 27, p. 417–462.

Stipp, M., Stünitz, H., Heilbronner, R., and Schmid, S.M., 2002, The eastern Tonale fault zone: A "natural laboratory" for crystal plastic deformation of quartz over a temperature range from 250 to 700 °C: Journal of Structural Geology, v. 24, p. 1861–1884.

Wells, M.L., Dallmeyer, R.D., and Allmendinger, R.W., 1990, Late Cretaceous extension in the hinterland of the Sevier thrust belt, northwestern Utah and southern Idaho: Geology, v. 18, p. 929–933.

Wells, M.L., Spell, T. L., and Grove, M., 2002, Late Cretaceous intrusion and extensional exhumation of the Cadiz Valley Batholith, Iron Mountains, Southeastern California: Geological Society of America Abstracts with Programs. v. 34, No. 6, p.178.

Wells, M.L., Beyene, M.A., Spell, T.L., Kula, J.L., Miller, D.M., Zanetti, K.A., 2005, The Pinto zone; a Laramide synconvergent extensional shear zone in the Mojave Desert region of the southwest United States: Journal of Structural Geology, v.27, p. 1697-1720.

Wells, M.L., and Hoisch, T. D., 2008, The role of mantle delamination in widespread Late Cretaceous extension and magmatism in the Cordilleran orogen, western United States: Geological Society of America Bulletin, v. 120, p. 515-530.

Wells, M.L., and Hoisch, T. D., Cruz-Uribe, A.M., and Vervoort, J.D., 2012, Geodynamics of synconvergent extension and tectonic mode switching: Constraints from the Sevier-Laramide orogen: Tectonics, v. 31, 20 p.

Yonkee, W.A. and Weil, A.B., 2015. Tectonic evolution of the Sevier and Laramide belts within the North American Cordillera orogenic system. *Earth-Science Reviews*, *150*, p.531-593.

Young, R.A., and Hartman, J. H., 2014, Paleogene rim gravel of Arizona: Age and significance of the Music Mountain Formation: Geosphere, v. 10, p. 870-891.

Zeitler, P. K., 1993, Inversion of $^{40}Ar/^{39}Ar$ age spectra using the controlled-random-search method, Eos Trans. AGU, 74(43), 650.

VITAE

Personal Strengths: Geologic mapping, structural geology, tectonics and orogenesis, economic geology and hydrothermal systems, 3D modeling.

Education

Master of Science (Geology) *University of Nevada, Las Vegas* GPA: 3.91 *2015-May2017*

- Project: Late Cretaceous extensional collapse of the southern Cordillera. Project has strong emphasis on field mapping, structural analysis, analytical work, and igneous petrology. Advisor: Dr. Michael L. Wells
- Teaching assistant for upper level Field Methods and Advanced Field classes.

Bachelor of Science (Geology) *Idaho State University* GPA: 3.38 *2009-2011*

- Senior Project: *Detrital zircons from the Maurice Mountain Quartzite and Black Lion Conglomerate, Pioneer Mountains, SW Montana: The southern edge of the Belt Basin.*
- Project was presented at the Geological Society of America Conference, Rocky Mountain/Cordilleran Section, 2011 (as a poster).

Associate of Arts (Liberal Arts) *College of Southern Idaho* *2006-2009*

Work Experience

Project Geologist *Silver Standard Resources Inc.* *May 2017-Present*

- Structural mapping by hand at designated scale on North American project. Digitizing maps and data compiling. Core logging. Mapped Palaeoproterozoic shear zone hosted gold deposits in northern Saskatchewan - developed targets for drilling campaign.

Mapping Geologist *Silver Standard US Inc.* *June 2016-August 2016*

- Performed detailed structural mapping on the Perdito Project, Inyo Mountains, California. Mapped claim areas at 1:2,500 scale, mapped detailed surface structural geology, as well as oxidation and alteration outcrop maps. Provided digitized maps and thorough documents reporting findings and targets for future drilling campaigns.

Field Geologist *Louisiana State University* *June 2014-August 2014*

- Provided geological field assistance for Prof. Barbara Dutrow in the Sawtooth Mountain Metamorphic Complex, Idaho.
- Performed detailed geologic mapping, rock descriptions, and precise sample collection for all metamorphic units.

Geologist *Lost River Geologic Services (sole-proprietor)* *May 2011-April 2014*
- Provided detailed geology for Hudson Ranch Power, LLC and EnergySource, LLC.
- Mapping borehole cuttings, interpreting and preparing XRD samples, interpreting 3D reflection seismic, managing geophysical surveys, developing 3D models. Submitted technical

reports (see attached citations), and assisted with the targeting and development of numerous production wells in the Salton Sea Geothermal Field, California.

Zircon Separation Lab Manager *Idaho State University* *October 2010–May 2011*

- Managed a team of students through the complete process of separating zircons from their parent rock to analysis at the LA-ICP-MS lab at UA

Field Assistant *Idaho State University - Geosciences* *Summer 2010*

- Provided field assistance for ISU graduate student. Mapping metasedimentary rocks, intermediate and bimodal volcanic rocks and performing structural analysis on the Wildhorse detachment fault.

Weeds Technician *Bureau of Land Management, CFO* *Summers 2006–2009*

- Responsible for the identification and management of endemic and invasive species on 800,000 acres, rangeland health monitoring, and ecosystem preservation in riparian areas.

Report and abstract citations

Hess, L.T., and Wells, M.L., 2016, Development and disaggregation of a plutonic complexion SE California: Constrains on Late Cretaceous collapse of the Sevier orogen. Geological Society of America Abstracts, National Conf., Paper No. 55-5.

Hess, L.T., and Wells, M.L., 2016, Late Cretaceous to Neogene Tectonic History of the Bristol and Granite Mountains, Southeast California. Geological Society of America Abstracts, Cordilleran Section, Paper No. 26-5.

Link, P.K., Stewart, E.D., Steel, T., Sherwin, J., **Hess, L.T**., and McDonald, C., 2016, Detrital zircons in the Mesoproterozoic upper Belt Supergroup in the Pioneer, Beaverhead and Lemhi Ranges, MT and ID: The Big White arc. GSA Special Paper 522 Belt Basin: Window to Mesoproterozoic Earth.

Hess, L.T., 2013a, Hudson Ranch II Well 19-2: Detailed Visual Observations from Drill Cuttings. Internal report prepared for EnergySource, LLC, 18p.

Hess, L.T., 2013b, Hudson Ranch II Well 19-1 Side-Track: Detailed Visual Observations from Drill Cuttings. Internal report prepared for EnergySource, LLC, 16p.

Hess, L.T., Link, P.K., and McDonald, K.M., 2011, Detrital zircons from the Maurice Mountain Quartzite and Black Lion Conglomerate, Pioneer Mountains, SW Montana: The southern edge of the Belt Basin: Geological Society of America Abstracts with Programs, v. 43, no. 4, p. 69.

Hess, L.T., 2012a, Detailed Visual Investigation of Alteration and Flow Zones in Legacy Geothermal Wells Located Near the Hudson Ranch Project Area. Internal report prepared for EnergySource, LLC, 32p.

Hess, L.T., 2012b, Analysis of Reflection Seismic Features. Internal report prepared for EnergySource, LLC, 9p.

Neuhoff, P., and **Hess, L.T.** 2012. Alteration History of Geothermal Wells in the Vicinity of the Hudson Ranch Project, Imperial County, California. Internal report prepared for EnergySource, LLC, 19p.

Norton, D.L., Sims, D., Neuhoff, P., and **Hess, L.T.** 2011. Geologic Review of Hudson

Ranch Geothermal Wellfield. Internal report prepared for Energy Source, LLC, 59p.

Awards

- Awarded NAGT internship opportunity for best field camp student, 2010
- Geological Society of America graduate student research grant, 2016
- Graduate student academic achievement award at UNLV, 2017

Computer skills

- Office, Windows, Mac OS, Photoshop, Illustrator
- LeapFrog 3D modeling, ArcGIS, Mathematica, Opendtect, Maptek Vulcan, Global Mapper